CHALMERS
UNIVERSITY OF TECHNOLOGY

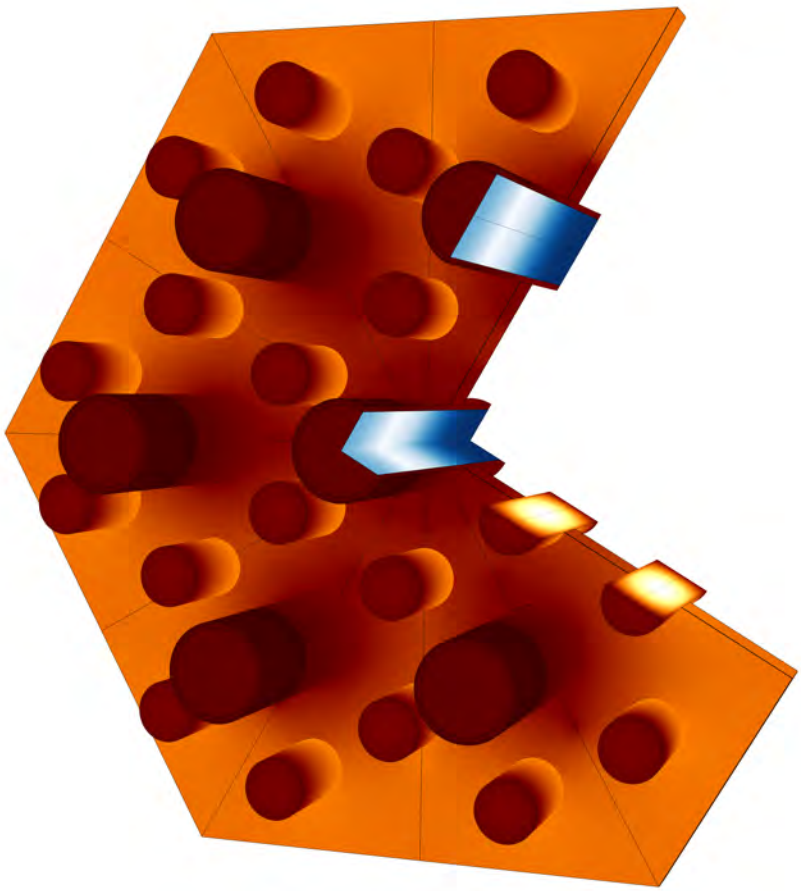

At the Heat-Pipe Limit

Coupled Modelling and Operating-Limit Assessment of a Fuel Assembly in a Heat-Pipe-Cooled Microreactor

Master's thesis in Physics

Karl Andersson, Felix Persson

DEPARTMENT OF PHYSICS
CHALMERS UNIVERSITY OF TECHNOLOGY
Gothenburg, Sweden 2026
www.chalmers.se

Master's thesis 2026

At the Heat-Pipe Limit

Coupled Modelling and Operating-Limit Assessment of a Fuel Assembly in a Heat-Pipe-Cooled Microreactor

KARL ANDERSSON & FELIX PERSSON

CHALMERS
UNIVERSITY OF TECHNOLOGY

Department of Physics
Division of Subatomic, High Energy and Plasma Physics
Chalmers University of Technology
Gothenburg, Sweden 2026

At the Heat-Pipe Limit
Karl Andersson, Felix Persson

Supervisor & Examiner: Christophe Demazière

Master's Thesis 2026
Department of Physics
Chalmers University of Technology
SE-412 96 Gothenburg
Telephone +46 31 772 1000

Cover: Three-dimensional rendering of the temperature profile from the first simulation treated in the results chapter. A sector of the fuel assembly has been removed to reveal the two-dimensional temperature profiles of the heat pipe and fuel pin. The geometric length scales have been adjusted to improve the clarity of the figure.

Typeset in LaTeX
Printed by Chalmers Reproservice
Gothenburg, Sweden 2026

At the Heat-Pipe Limit
KARL ANDERSSON & FELIX PERSSON
Department of Physics
Chalmers University of Technology

Abstract

Heat pipes are efficient transporters of heat and are currently being considered in new microreactor designs. To support efforts in understanding the behaviour and limitations associated with using heat pipes as primary heat removal components in microreactors, a reduced coupled model of a fuel assembly is developed in this thesis. The model is based on publicly available information on the Westinghouse eVinci reactor, a prominent design currently under development. The reduced model functions as an effective one-fuel-pin–one-heat-pipe model of a fuel assembly in an eVinci-like reactor and couples one-dimensional neutronics, two-dimensional heat transfer, and one-dimensional fluid flow. Applying the model to an estimated reactor configuration suggests that an eVinci-like reactor operating at the marketed power output is within the heat-pipe limits considered in this thesis. The results also indicate that the model complexity can be further reduced in normal operating conditions, and partly in limiting conditions. Fixed-temperature approximations for the neutronic data and the thermal conductivities have a small effect on the neutronic effective multiplication factor, and do not alter the temperature and neutron-flux distributions significantly. Furthermore, approximating the heat-pipe vapour as isothermal is acceptable under normal operating conditions, but breaks down near the sonic limit.

Keywords: microreactor, heat pipe reactor, heat pipe, eVinci, reactor physics, nuclear reactor

Acknowledgements

We would like to thank our supervisor Christophe for his engagement, guidance, and valuable discussions throughout this work, as well as for proposing the intriguing research idea behind this thesis. Never would we have guessed that a heat-transporting pipe could be so interesting.

We would also like to thank our families for their endless support and encouragement.

Finally, we would like to thank our friends at Chalmers for making the last five years memorable and enjoyable.

Karl Andersson and Felix Persson, Gothenburg, June 2026

Below is the nomenclature of variables, indices, and subscripts used throughout this thesis.

Variables and parameters

General and finite-volume notation

A	Cross-sectional area / generic extensive quantity in a balance equation
d	Distance
a	Volumetric density corresponding to the extensive quantity A
$\boldsymbol{J}_a$	Flux of the quantity a
$\hat{\boldsymbol{N}}$	Outward unit normal vector
$\boldsymbol{r}$	Position vector
r	Radial coordinate
Δr	Radial cell length
S	Surface or face area
s_a	Volumetric source term for the quantity a
t	Time
V	Volume or control volume
$\boldsymbol{v}$	Velocity field
z	Axial coordinate
Δz	Axial cell length
α	Generic transport coefficient in a gradient-driven flux law
Φ	Generic driving potential
$\mathcal{B}$	Set of boundary faces belonging to a control volume
$\mathcal{F}$	Set of faces belonging to a control volume
$\mathcal{I}$	Set of integration points of a face or control volume

Thermal transport

h	Convective heat-transfer coefficient
k	Thermal conductivity
P	Power
Q	Heat-transfer rate
q''	Surface heat flux
q'''	Volumetric heat source

R	Thermal resistance
T	Temperature
ΔT	Temperature difference
U	Internal energy

Heat-pipe and fluid-dynamic quantities

D_h	Hydraulic diameter
f_D	Darcy friction factor
h_fg	Enthalpy of vaporisation
K	Wick permeability
$\dot{m}$	Mass flow rate
p	Pressure
Δp	Pressure difference or pressure drop
R_g	Specific gas constant
R^*	Annular radius ratio
r_eff	Effective pore radius
u_p	Pore velocity
v	Axial mean vapour velocity
Γ	Volumetric vapour mass source
γ	Ratio of specific heat capacities
γ_σ	Saturation-curve derivative, $(\partial p/\partial T)_\sigma$
ζ	Annular-flow correction factor
μ	Dynamic viscosity
ρ	Density
σ	Surface tension
$\boldsymbol{\sigma}$	Cauchy stress tensor
$\boldsymbol{\tau}$	Viscous stress tensor
φ	Wick porosity
Ma	Mach number
Re	Reynolds number
We	Weber number

Neutronics

D	Neutron diffusion coefficient
E	Neutron energy

$\boldsymbol{J}$	Neutron current density
k_{eff}	Effective neutron multiplication factor
N_G	Number of neutron energy groups
n	Neutron density
v_n	Neutron speed
κ	Energy released per fission
ν	Average number of neutrons produced per fission
Σ	Macroscopic cross section
ϕ	Scalar neutron flux
χ	Fission spectrum
ψ	Angular neutron flux
$\boldsymbol{\Omega}$	Angular direction

Indices and subscripts

a	Absorption
ad	Adiabatic region / adiabatic quantity
b	Boundary face index
C	Control-volume centre of current cell
c	Critical quantity, when used in saturation properties
clad	Cladding-region quantity
cond	Conduction
conv	Convection
eff	Effective quantity
env	Environmental sink-side quantity
evap	Evaporator quantity
F	Control-volume centre of neighbouring cell
f	Face index / fission
FP	Fuel-pin quantity
fuel	Fuel-region quantity
g	Neutron energy-group index
gap	Gap-region quantity
HP	Heat-pipe quantity
in	Inlet or input quantity

l	Liquid phase
mod	Moderator quantity
n	Neutron quantity
op	Operating condition
out	Outlet or output quantity
s	Scattering in neutronics / solid phase in thermal or fluid contexts
t	Total quantity
tr	Transport quantity
v	Vapour phase
vap	Vapour-region quantity
w	Wall quantity
wick	Wick quantity
ww	Wall–wick region quantity

Contents

List of Figures

List of Tables

1

Introduction

In a nuclear reactor, the energy released by fission is first deposited in the fuel. The usefulness and safety of a nuclear reactor are therefore contingent not only on sustaining controlled chain reactions, but also on the ability to remove this heat effectively. For compact reactor concepts such as microreactors, effective and reliable heat removal becomes especially important, since the available space for coolant systems, pumps, and auxiliary components is limited.

A promising solution to the heat removal problem for microreactors is the use of heat pipes. They make use of capillary action and phase transitions in the working fluid to transport large amounts of heat over small temperature differences, without mechanical pumps. The passive nature of heat pipes makes them attractive for microreactors intended for remote applications, including military bases and disaster relief [3, 4].

Although heat pipes have existed for several decades, their application to nuclear reactor systems has received renewed attention in recent years. One important demonstration was the KRUSTY experiment in 2018, which showed the feasibility of a heat-pipe-cooled fission system coupled to Stirling power conversion [5]. Since then, several heat-pipe-cooled microreactor concepts have entered development, including Westinghouse's eVinci reactor and the Antares Mark-0 reactor. In early June 2026, Antares Nuclear announced that its Mark-0 microreactor had achieved criticality [6, 7].

Using heat pipes as a method of cooling the reactor core brings about several unique limitations. If one or several limitations are reached, the heat pipes cannot transport the imposed heat load and safe operation can no longer be maintained [4]. These limits must be assessed in the context of fission heat generation and temperature profiles in the reactor. This motivates the development of a coupled model of a heat-pipe-cooled microreactor.

1.1 Nuclear reactors and microreactors

A nuclear reactor is a system that produces heat through controlled fission chain reactions. Heat can either be used directly, for example in industrial processes or district heating, or converted into electricity through a power-conversion system [8, 9]. Reactors are often classified according to their electrical power output.

Large conventional reactors typically produce more than 700 MW(e), while small modular reactors are commonly defined as reactors with outputs up to approximately 300 MW(e), in addition to being modular. Microreactors form an even smaller class, with electrical outputs typically up to approximately 10 MW(e) [10].

The smaller scale of microreactors makes them attractive for applications where large centralised reactors are impractical. Examples include remote communities, mining sites, military bases, space applications, and backup power for critical infrastructures. In such settings, transmission lines may be unavailable, grid capacity may be limited, or conventional diesel generators may be expensive and carbon-intensive to operate [10, 6, 11].

1.2 Heat pipes

Heat pipes operate by circulating a liquid through a porous structure, called a wick, and the corresponding vapour through a vapour channel. The driving mechanism is capillary action. Heat applied on the evaporator outer wall and removed at the condenser outer wall is thus both transported advectively, with the working fluid, and via thermal conduction. This makes heat pipes significantly more effective than solid pipes and makes large heat transfer possible across small temperature differences. An illustration of a cylindrical heat pipe is shown in Figure 1.1.

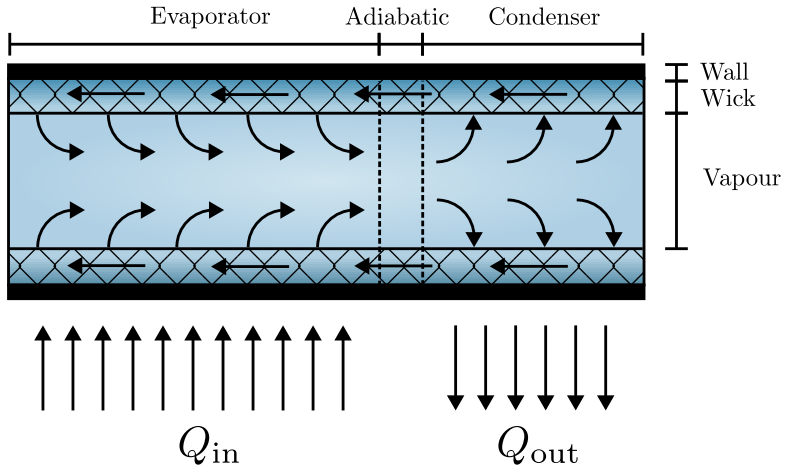

Figure 1.1: Illustration of a cylindrical heat pipe. Heat is applied to the evaporator outer wall and is removed at the condenser outer wall. Consequently, the working fluid evaporates in the evaporator wick and condenses in the condenser wick. No heat is applied or removed on the adiabatic outer wall.

If the capillary action is not sufficient to drive the working fluid under a specific condition, the heat pipe cannot transport the heat load imposed at the evaporator

entrance, and heat removal has failed. This is called a capillary limitation and is one of several limitations relevant for heat-pipe operation. Other heat-transfer limitations include the sonic, boiling, entrainment, viscous, condenser, continuum flow, and frozen startup limitations. Of these, the capillary, boiling, and entrainment limitations are severe and cause local dry-out in the evaporator, thereby inhibiting heat transfer. The last four limitations are mainly relevant during startup [4]. The capillary, sonic, boiling, and entrainment limitations are described in more detail later in Chapter 2, as these are the limits most relevant for the present analysis.

1.3 Heat-pipe-cooled microreactor concept

A heat-pipe-cooled microreactor consists of fuel pins, a moderating material, and heat pipes arranged in a compact reactor core. The specific materials, geometry, and arrangement of these components define different reactor concepts. In this thesis, the reactor design is inspired by the eVinci reactor, currently under development by Westinghouse. The eVinci concept consists of hexagonal fuel assemblies containing sodium heat pipes, fuel pins loaded with TRISO fuel, and a graphite moderator. The wick in the heat pipes is assumed to be annular. One reported layout contains 7 heat pipes and 24 fuel pins per assembly, with a total of 876 heat pipes and 2970 fuel pins, producing approximately 15 MW(th) and 4.5 MW(e) [6]. The hexagonal fuel assembly is shown in Figure 1.2.

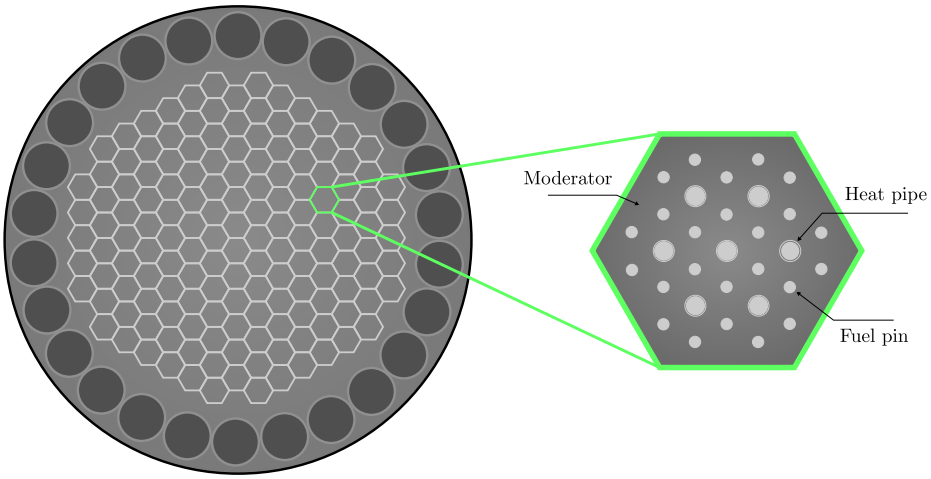

Figure 1.2: The right-hand side shows an eVinci-inspired hexagonal layout of fuel pins and heat pipes. The heat pipes are arranged in a hexagonal structure, with a heat pipe in the middle, and the fuel pins populate the space around the heat pipes in a hexagonal pattern. The left-hand side shows an example of a full reactor design inspired by eVinci, but is not part of the analysis in this report.

In such a reactor, heat is generated in the fuel by fission reactions. Neutrons released in fission are slowed down by the moderator, increasing the probability of further

fission reactions in the fuel. The resulting heat is conducted from the fuel pins into the surrounding moderator, and then transferred to neighbouring heat pipes, which provide the primary heat-removal mechanism.

The part of each heat pipe embedded in the reactor core acts as the evaporator section, where heat addition causes the working fluid to evaporate. The vapour then transports heat axially through the heat pipe towards the condenser section, where heat is rejected to an external coolant or heat sink and the vapour condenses. In wicked heat pipes, the condensed liquid is returned to the evaporator by capillary action, allowing operation even when gravity acts against the direction of liquid return. In this way, heat pipes replace the actively pumped primary coolant loop used in many conventional reactor systems.

The representation of the fuel assembly will vary throughout the thesis, depending on the physical process being considered. A representative hexagonal fuel assembly is used to generate homogenised neutronic data, while a one-twelfth symmetry slice is used to estimate an effective thermal resistance of the moderator. These results are then combined in a reduced one-fuel-pin–one-heat-pipe model, which forms a coupled reactor system used to study the interaction between heat generation, heat removal, and heat-pipe limitations.

1.4 Motivation for coupled modelling

The neutronics, heat transfer, and fluid dynamics present in the reactor are inherently coupled. The spatial and energetic distribution of neutrons is affected by temperature, while the temperature is influenced by the heat generation induced by neutrons. The vapour flow in the heat pipe is also coupled to the temperature profile, since evaporation, condensation, pressure, and density depend on the thermal state of the working fluid. To evaluate the state of the fuel assembly, information about the different subsystems therefore needs to be exchanged.

Additionally, a reactor state that appears acceptable from the perspective of one component may be unacceptable when the full system is considered. For example, a heat pipe may operate below its heat-transfer limits while the corresponding fuel temperature is too high. Taken together, these reasons motivate a coupled model of the fuel assembly.

Several modelling tools and frameworks have already been developed or applied to heat-pipe-cooled microreactors, many of them based on the MOOSE framework [12]. Important examples include Sockeye for heat-pipe modelling, Griffin for neutronics modelling, and DireWolf for coupled heat-pipe reactor simulations [13, 14, 15]. However, the purpose of this thesis is not to reproduce the same high-fidelity simulation capabilities demonstrated by these tools. Instead, a reduced coupled model is developed in order to understand the main interactions of a heat-pipe-cooled reactor, as well as some important limitations associated with heat-pipe operation.

1.5 Aim and research questions

The aim of this thesis is to develop a reduced model capable of simulating the main physical mechanisms in a representative fuel assembly of a heat-pipe-cooled microreactor. This thesis considers the coupled interplay between the neutron-flux distribution in the fuel assembly, the temperature distributions in the fuel pins and heat pipes, and the vapour flow in the heat-pipe vapour channel. Calculations of the capillary and sonic limitations are demonstrated using the coupled model, while the entrainment and boiling limits are estimated using analytical expressions.

The following research questions are addressed:

1. What operating conditions and heat-pipe limitations are predicted for a representative fuel assembly of a steady-state eVinci-like microreactor operating at marketed power output?
2. How does the predicted reactor state change when different levels of model complexity are introduced, including axial discretisation of the heat-pipe vapour and temperature-dependent material and neutronic data?

1.6 Scope and limitations

The scope of this thesis is limited to developing a reduced coupled model of a representative heat-pipe-cooled microreactor fuel assembly. The final coupled model is a two-dimensional, steady-state, effective one-fuel-pin–one-heat-pipe model. Homogenised neutronic data are obtained from OpenMC simulations of an eVinci-like hexagonal fuel assembly, while the moderator is represented by effective thermal resistances estimated from a symmetric one-twelfth slice of the assembly. In the coupled model, the neutronics are represented by a discretised axial neutron flux, with neutronic parameters determined from the homogenised OpenMC data using interpolated average temperatures in the fuel pins, moderator, and heat pipes. The coupled model thus treats the inhomogeneities introduced by the distribution of the neutron flux, temperatures, and heat-pipe fluid.

Heat transfer is resolved radially and axially in the effective fuel pin and heat pipe, while heat transfer through the moderator is represented by effective thermal resistances. The vapour flow in the heat pipe is modelled as cross-sectionally averaged, axially discretised flow, with friction losses represented using the Darcy–Weisbach relation. Because of these reductions, the model does not resolve the full three-dimensional fuel assembly, local pin-to-pin variations, detailed moderator temperature fields, or local heat-pipe effects around individual wick pores and liquid–vapour interfaces. The results should therefore be interpreted as predictions of a reduced modelling framework rather than as industry-level performance estimates for a specific reactor.

The analysis is restricted to steady-state reactor conditions. Transient behaviour during startup, shutdown, load changes, or accident scenarios is therefore not considered. The heat-pipe limitation analysis is limited to the capillary, boiling, sonic, and

entrainment limitations, while other heat-pipe phenomena, such as frozen startup, non-condensable gases, long-term degradation, and detailed dry-out dynamics, are outside the scope of the thesis. Finally, the heat pipes are assumed to have an annular wick and to be perfectly horizontal, such that effects due to gravity are not present.

2

Physical Theory

The purpose of this chapter is to describe the physical theory behind the models used in this thesis. The chapter starts by introducing balance equations as a useful framework for the governing equations. This framework is then applied to the three main physical topics considered in the thesis: neutrons in the reactor, heat transport within the reactor, and fluid dynamics in the interior region of the heat pipes. The chapter concludes with a discussion of heat pipe limitations relevant to steady-state operation.

2.1 Balance equations

For our purposes, balance equations provide a useful mathematical framework for describing how physical quantities are transported, produced, and removed within a system. To introduce this framework, consider an extensive quantity $A(t)$ contained in a fixed control volume V. Let $a(\boldsymbol{r}, t)$ denote the corresponding volumetric density, such that

$$A(t) = \int_V a(\boldsymbol{r}, t)\, d^3\boldsymbol{r}. \tag{2.1}$$

As illustrated in Figure 2.1, the quantity A may change due to transport across the boundary ∂V or due to sources and sinks inside V. Since the control volume is fixed

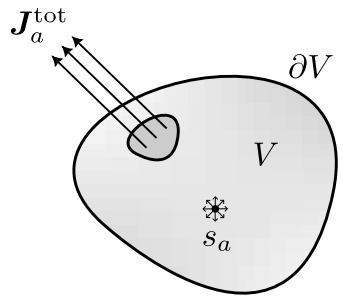

Figure 2.1: An arbitrary volume V, with boundary ∂V. Flux $\boldsymbol{J}_a^{\text{tot}}$ may cross the boundary of the volume, and sources and sinks s_a may appear inside the volume.

in time, the integral balance equation can be written as

$$\int_V \frac{\partial a}{\partial t}(\boldsymbol{r}, t)\, d^3\boldsymbol{r} + \int_{\partial V} \boldsymbol{J}_a^{\text{tot}}(\boldsymbol{r}, t) \cdot \hat{\boldsymbol{N}}\, dS = \int_V s_a(\boldsymbol{r}, t)\, d^3\boldsymbol{r}, \tag{2.2}$$

where $\boldsymbol{J}_a^{\text{tot}}$ is the total flux of A, such that $\boldsymbol{J}_a^{\text{tot}}$ is positive when pointed outwards, $\hat{\boldsymbol{N}}$ is the outward unit normal on ∂V, and s_a is the volumetric source term [16, Ch. 2.3]. In this thesis, we are exclusively concerned with steady-state operation, and can neglect the term containing the time derivative. Using the divergence theorem, the balance equation can then be written as

$$\int_V \boldsymbol{\nabla} \cdot \boldsymbol{J}_a^{\text{tot}}(\boldsymbol{r})\, d^3\boldsymbol{r} = \int_V s_a(\boldsymbol{r})\, d^3\boldsymbol{r}. \tag{2.3}$$

Because V is chosen arbitrarily, the integrand itself must satisfy the equation locally. Therefore, we can write equation (2.3) in its differential form

$$\boldsymbol{\nabla} \cdot \boldsymbol{J}_a^{\text{tot}}(\boldsymbol{r}) = s_a(\boldsymbol{r}). \tag{2.4}$$

The total flux can often be decomposed into advective and non-advective contributions. Advective transport is associated with the transport of a quantity by a velocity field and has the form

$$\boldsymbol{J}_a^{\text{adv}} = a\boldsymbol{v}, \tag{2.5}$$

where $\boldsymbol{v}$ is the velocity field. Non-advective transport is typically described through constitutive relations. Examples include Fick's law for diffusion, Fourier's law for heat conduction, and Darcy's law for flow through porous media. These relations often take a linear gradient-driven form

$$\boldsymbol{J}_a^{\text{lin}} = -\alpha \boldsymbol{\nabla} \phi, \tag{2.6}$$

where ϕ is the driving potential and α is the corresponding transport coefficient [16, Ch. 2.3]. Other flux contributions may be collected in a remaining term $\boldsymbol{J}_a^{\text{other}}$. Thus, a useful schematic decomposition of the total flux is

$$\boldsymbol{J}_a^{\text{tot}} = \boldsymbol{J}_a^{\text{adv}} + \boldsymbol{J}_a^{\text{lin}} + \boldsymbol{J}_a^{\text{other}} = a\boldsymbol{v} - \alpha \boldsymbol{\nabla} \phi + \boldsymbol{J}_a^{\text{other}}. \tag{2.7}$$

Substituting this decomposition into equation (2.4) gives the balance-equation template

$$\boldsymbol{\nabla} \cdot \left[a(\boldsymbol{r})\boldsymbol{v}(\boldsymbol{r}) - \alpha(\boldsymbol{r}) \boldsymbol{\nabla} \phi(\boldsymbol{r}) + \boldsymbol{J}_a^{\text{other}}(\boldsymbol{r}) \right] = s_a(\boldsymbol{r}). \tag{2.8}$$

2.2 Neutron balance

The goal of this section is to derive the steady-state multi-group diffusion equations used to describe neutron production, removal, and transport in the fuel-assembly model. The derivation starts from neutron transport theory and then introduces two common approximations: the multi-group approximation for the energy dependence and the diffusion approximation for the angular dependence. Basic nuclear interactions and the distinction between microscopic and macroscopic cross sections are assumed known and are therefore not derived in detail. Delayed neutron effects are represented under the assumption that precursor concentrations are in equilibrium. Before introducing the neutron transport equation, it is useful to define a few central quantities.

- The neutron density, $n(t, \boldsymbol{r}, E, \boldsymbol{\Omega})$, is defined such that

$$n(t, \boldsymbol{r}, E, \boldsymbol{\Omega})\, d^3\boldsymbol{r}\, dE\, d^2\boldsymbol{\Omega} \tag{2.9}$$

  is the number of neutrons at time t in a volume element $d^3\boldsymbol{r}$ about $\boldsymbol{r}$, with energies in dE about E, and directions within the solid angle element $d^2\boldsymbol{\Omega}$ about $\boldsymbol{\Omega}$.

- The angular neutron flux is defined as

$$\psi(t, \boldsymbol{r}, E, \boldsymbol{\Omega}) \equiv v(E) n(t, \boldsymbol{r}, E, \boldsymbol{\Omega}), \tag{2.10}$$

  where $v(E)$ is the neutron speed. The angular flux describes the neutron flux associated with position $\boldsymbol{r}$, energy E, and direction $\boldsymbol{\Omega}$.

- The scalar neutron flux is obtained by integrating the angular flux over all directions:

$$\phi(t, \boldsymbol{r}, E) \equiv \int_{4\pi} \psi(t, \boldsymbol{r}, E, \boldsymbol{\Omega})\, d^2\boldsymbol{\Omega}. \tag{2.11}$$

  It measures the angular flux integrated over all directions at position $\boldsymbol{r}$ and energy E.

- The neutron current density vector is defined as the first angular moment of the angular flux:

$$\boldsymbol{J}(t, \boldsymbol{r}, E) \equiv \int_{4\pi} \boldsymbol{\Omega}\, \psi(t, \boldsymbol{r}, E, \boldsymbol{\Omega})\, d^2\boldsymbol{\Omega}. \tag{2.12}$$

  Unlike the scalar flux, the current density measures the net directional transport of neutrons.

To clarify the necessity to define both neutron flux and neutron current density, it is useful to note that in neutron transport, the term flux is used differently from the vector flux introduced in Section 2.1. The scalar neutron flux represents the number of neutrons at a position irrespective of the neutron direction, and is therefore useful for calculating reaction rates. For example, the total number of neutron interactions of type X in a volume V over a time interval dt about time t, can be written using the corresponding cross section Σ_X and the scalar neutron flux [17, Ch. 5.1]

$$dt \int_V \int_0^\infty \Sigma_X(t, \boldsymbol{r}, E) \phi(t, \boldsymbol{r}, E)\, d^3\boldsymbol{r}\, dE. \tag{2.13}$$

In contrast, the neutron current density vector is comparable to the vector flux appearing in the general balance equation, since it represents the net directional transport of neutrons.

2.2.1 Neutron transport equation

The neutron transport equation is a balance equation for the energy- and direction-resolved number of neutrons. The corresponding density is $n(t, \boldsymbol{r}, E, \boldsymbol{\Omega})$. The relevant advective velocity is the neutron velocity $v(E)\boldsymbol{\Omega}$, so the advective flux in phase space is $v(E)\boldsymbol{\Omega}\, n(t, \boldsymbol{r}, E, \boldsymbol{\Omega})$. Applying the local balance equation gives [16, Ch. 2.2.b]

$$\frac{\partial n}{\partial t}(t, \boldsymbol{r}, E, \boldsymbol{\Omega}) + \boldsymbol{\nabla} \cdot [v(E)\boldsymbol{\Omega}\, n(t, \boldsymbol{r}, E, \boldsymbol{\Omega})] = Q_n(t, \boldsymbol{r}, E, \boldsymbol{\Omega}), \tag{2.14}$$

where Q_n denotes the volumetric production or disappearance term. Using the definition $\psi = vn$, this can be written as

$$\frac{1}{v(E)}\frac{\partial \psi}{\partial t}(t, \boldsymbol{r}, E, \boldsymbol{\Omega}) + \boldsymbol{\nabla} \cdot [\boldsymbol{\Omega}\psi(t, \boldsymbol{r}, E, \boldsymbol{\Omega})] = Q_n(t, \boldsymbol{r}, E, \boldsymbol{\Omega}). \tag{2.15}$$

Neutrons disappear from a given phase-space element through absorption or through scattering to another energy or direction. This is represented by the total macroscopic cross section Σ_t, giving

$$Q_n^-(t, \boldsymbol{r}, E, \boldsymbol{\Omega}) = -\Sigma_t(t, \boldsymbol{r}, E)\psi(t, \boldsymbol{r}, E, \boldsymbol{\Omega}). \tag{2.16}$$

Neutrons are produced in the phase-space element $(\boldsymbol{r}, E, \boldsymbol{\Omega})$ mainly by scattering from other energies and directions, and by fission. The scattering source is

$$Q_n^{+,\mathrm{scat}}(t, \boldsymbol{r}, E, \boldsymbol{\Omega}) = \int_{4\pi}\int_0^\infty \Sigma_s(t, \boldsymbol{r}, E' \to E, \boldsymbol{\Omega}' \to \boldsymbol{\Omega})\psi(t, \boldsymbol{r}, E', \boldsymbol{\Omega}')\, dE'\, d^2\boldsymbol{\Omega}', \tag{2.17}$$

where $\Sigma_s(t, \boldsymbol{r}, E' \to E, \boldsymbol{\Omega}' \to \boldsymbol{\Omega})$ is the macroscopic differential scattering cross section. The fission source is described using the average number of neutrons emitted per fission reaction, ν, the macroscopic fission cross section, Σ_f, and the fission spectrum, χ. Assuming isotropic fission emission in the laboratory reference frame, the fission source is

$$Q_n^{+,\mathrm{fis}}(t, \boldsymbol{r}, E, \boldsymbol{\Omega}) = \frac{\chi(\boldsymbol{r}, E)}{4\pi}\int_{4\pi}\int_0^\infty \nu(\boldsymbol{r}, E')\Sigma_f(t, \boldsymbol{r}, E')\psi(t, \boldsymbol{r}, E', \boldsymbol{\Omega}')\, dE'\, d^2\boldsymbol{\Omega}'. \tag{2.18}$$

Here, χ denotes the effective fission spectrum of both prompt and delayed neutrons. The factor $1/(4\pi)$ represents the isotropic angular distribution of fission neutrons.

Substituting these source terms into equation (2.15) gives the time-dependent neutron transport equation:

$$\begin{aligned} &\frac{1}{v(E)}\frac{\partial \psi}{\partial t}(t, \boldsymbol{r}, E, \boldsymbol{\Omega}) + \boldsymbol{\nabla} \cdot [\boldsymbol{\Omega}\psi(t, \boldsymbol{r}, E, \boldsymbol{\Omega})] + \Sigma_t(t, \boldsymbol{r}, E)\psi(t, \boldsymbol{r}, E, \boldsymbol{\Omega}) \\ &= \int_{4\pi}\int_0^\infty \Sigma_s(t, \boldsymbol{r}, E' \to E, \boldsymbol{\Omega}' \to \boldsymbol{\Omega})\psi(t, \boldsymbol{r}, E', \boldsymbol{\Omega}')\, dE'\, d^2\boldsymbol{\Omega}' \\ &+ \frac{\chi(\boldsymbol{r}, E)}{4\pi}\int_{4\pi}\int_0^\infty \nu(\boldsymbol{r}, E')\Sigma_f(t, \boldsymbol{r}, E')\psi(t, \boldsymbol{r}, E', \boldsymbol{\Omega}')\, dE'\, d^2\boldsymbol{\Omega}'. \end{aligned} \tag{2.19}$$

For a physical steady-state without an external source, neutron production and loss must balance; this is only possible for a critical system. In reactor calculations, the stationary problem is therefore commonly reformulated as an eigenvalue problem by scaling the fission source by $1/k$. The value of k is then the multiplication factor required for the stationary balance equation to hold, and can be defined as the number of neutrons released by fission per unit time over the sum of the number of neutrons leaking out of the system per unit time and the number of neutrons absorbed per unit time [16, Ch. 2.2]

$$k = \frac{\int_V \int_0^\infty \nu(\boldsymbol{r}, E)\Sigma_f(\boldsymbol{r}, E)\phi(\boldsymbol{r}, E)\, d^3\boldsymbol{r}\, dE}{\int_{\partial V} \int_0^\infty \boldsymbol{J}(\boldsymbol{r}, E) \cdot \hat{\boldsymbol{N}}\, dS\, dE + \int_V \int_0^\infty \Sigma_a(\boldsymbol{r}, E)\phi(\boldsymbol{r}, E)\, d^3\boldsymbol{r}\, dE} \tag{2.20}$$

A critical system has $k = 1$, while $k < 1$ and $k > 1$ correspond to subcritical and supercritical systems, respectively. The steady-state transport eigenvalue problem is therefore written as

$$\begin{aligned} &\boldsymbol{\nabla} \cdot [\boldsymbol{\Omega}\psi(\boldsymbol{r}, E, \boldsymbol{\Omega})] + \Sigma_t(\boldsymbol{r}, E)\psi(\boldsymbol{r}, E, \boldsymbol{\Omega}) \\ &= \int_{4\pi} \int_0^\infty \Sigma_s(\boldsymbol{r}, E' \to E, \boldsymbol{\Omega}' \to \boldsymbol{\Omega})\psi(\boldsymbol{r}, E', \boldsymbol{\Omega}')\, dE'\, d^2\boldsymbol{\Omega}' \\ &+ \frac{\chi(\boldsymbol{r}, E)}{4\pi k} \int_{4\pi} \int_0^\infty \nu(\boldsymbol{r}, E')\Sigma_f(\boldsymbol{r}, E')\psi(\boldsymbol{r}, E', \boldsymbol{\Omega}')\, dE'\, d^2\boldsymbol{\Omega}'. \end{aligned} \tag{2.21}$$

Although this equation is time-independent, it remains difficult to solve directly. It is represented in the six-dimensional phase space $(\boldsymbol{r}, E, \boldsymbol{\Omega})$, contains both differential and integral operators, and includes quantities with complicated energy dependence. The following subsections present the two main simplifications used in this thesis: the multi-group approximation and the diffusion approximation.

2.2.2 Multi-group formalism

The transport equation can be simplified by discretising the neutron energy interval into N_G energy groups. Let the group boundaries be $E_0 > E_1 > \cdots > E_{N_G}$, where $E_0 = E_{\max}$ and $E_{N_G} = E_{\min}$. The full energy interval is then

$$[E_{\min}, E_{\max}] = \bigcup_{g=N_G}^{1} [E_g, E_{g-1}]. \tag{2.22}$$

The convention is that the group index increases with decreasing neutron energy, so group $g = 1$ is the highest-energy group.

The group scalar flux is defined by

$$\phi_g(\boldsymbol{r}) = \int_{E_g}^{E_{g-1}} \phi(\boldsymbol{r}, E)\, dE. \tag{2.23}$$

Group-averaged quantities are defined so that reaction rates are preserved [16, Ch. 3.1.a]. For a generic macroscopic cross section Σ_α, this gives

$$\Sigma_{\alpha,g}(\boldsymbol{r}) = \frac{1}{\phi_g(\boldsymbol{r})} \int_{E_g}^{E_{g-1}} \Sigma_\alpha(\boldsymbol{r}, E)\phi(\boldsymbol{r}, E)\, dE. \tag{2.24}$$

Similarly, the group-averaged inverse speed is

$$\frac{1}{v_g(\boldsymbol{r})} = \frac{1}{\phi_g(\boldsymbol{r})} \int_{E_g}^{E_{g-1}} \frac{1}{v(\boldsymbol{r}, E)} \phi(\boldsymbol{r}, E)\, dE. \tag{2.25}$$

The same principle is used to define group-wise scattering and fission quantities.

2.2.3 From transport to diffusion theory

The primary goal of diffusion theory is to simplify the angular dependence in the transport equation. This is done in two steps. First, the transport equation is integrated over all directions $\boldsymbol{\Omega}$. Second, the P_1 and diffusion approximations are applied.

Integrating the steady-state transport eigenvalue equation over the unit sphere gives

$$\begin{aligned} &\boldsymbol{\nabla} \cdot \boldsymbol{J}(\boldsymbol{r}, E) + \Sigma_t(\boldsymbol{r}, E)\phi(\boldsymbol{r}, E) \\ &= \int_{4\pi}\int_{4\pi}\int_0^\infty \Sigma_s(\boldsymbol{r}, E' \to E, \boldsymbol{\Omega}' \to \boldsymbol{\Omega})\psi(\boldsymbol{r}, E', \boldsymbol{\Omega}')\, dE'\, d^2\boldsymbol{\Omega}'\, d^2\boldsymbol{\Omega} \\ &+ \frac{\chi(\boldsymbol{r}, E)}{k} \int_0^\infty \nu(\boldsymbol{r}, E')\Sigma_f(\boldsymbol{r}, E')\phi(\boldsymbol{r}, E')\, dE'. \end{aligned} \tag{2.26}$$

After this integration, the remaining angular dependence appears in the scattering term. A standard way to proceed is to expand the angular dependence of Equation (2.21) in spherical harmonics. This is known as the P_N method. In the P_1 approximation, the expansion is truncated after the first angular moment. The resulting P_1 equations are [16, Ch. 4.1]

$$\begin{aligned} &\boldsymbol{\nabla} \cdot \boldsymbol{J}(\boldsymbol{r}, E) + \Sigma_t(\boldsymbol{r}, E)\phi(\boldsymbol{r}, E) \\ &= \int_0^\infty \Sigma_{s0}(\boldsymbol{r}, E' \to E)\phi(\boldsymbol{r}, E')\, dE' + \\ &\frac{\chi(\boldsymbol{r}, E)}{k} \int_0^\infty \nu(\boldsymbol{r}, E')\Sigma_f(\boldsymbol{r}, E')\phi(\boldsymbol{r}, E')\, dE', \end{aligned} \tag{2.27}$$

and

$$\frac{1}{3}\boldsymbol{\nabla}\phi(\boldsymbol{r}, E) + \Sigma_t(\boldsymbol{r}, E)\boldsymbol{J}(\boldsymbol{r}, E) = \int_0^\infty \Sigma_{s1}(\boldsymbol{r}, E' \to E)\boldsymbol{J}(\boldsymbol{r}, E')\, dE'. \tag{2.28}$$

Here, Σ_{s0} and Σ_{s1} are the zeroth and first Legendre moments of the scattering cross section. In the most general case, deriving the P_1 equations requires assuming that there are no anisotropic neutron sources and that the time dependence of the neutron current density can be neglected [16, Ch. 4.1]. These assumptions are consistent with the steady-state fuel-assembly model considered in this thesis.

The diffusion approximation further simplifies the first-moment equation by assuming the anisotropic out-scatter from any of the energy groups is equal to the anisotropic in-scatter to that energy group. In other words,

$$\int_0^\infty \Sigma_{s1}(\boldsymbol{r}, E' \to E)\boldsymbol{J}(\boldsymbol{r}, E')\, dE' \approx \int_0^\infty \Sigma_{s1}(\boldsymbol{r}, E \to E')\boldsymbol{J}(\boldsymbol{r}, E)\, dE'. \tag{2.29}$$

Substituting equation (2.29) into equation (2.28) gives

$$\frac{1}{3}\boldsymbol{\nabla}\phi(\boldsymbol{r},E)+\left[\Sigma_t(\boldsymbol{r},E)-\Sigma_{s1}(\boldsymbol{r},E)\right]\boldsymbol{J}(\boldsymbol{r},E)=0, \tag{2.30}$$

where

$$\Sigma_{s1}(\boldsymbol{r},E)=\int_0^\infty \Sigma_{s1}(\boldsymbol{r},E\rightarrow E')\,dE'. \tag{2.31}$$

Solving for the current density gives Fick's law for neutron diffusion:

$$\boldsymbol{J}(\boldsymbol{r},E)=-D(\boldsymbol{r},E)\boldsymbol{\nabla}\phi(\boldsymbol{r},E). \tag{2.32}$$

The diffusion coefficient is

$$D(\boldsymbol{r},E)=\frac{1}{3\left[\Sigma_t(\boldsymbol{r},E)-\Sigma_{s1}(\boldsymbol{r},E)\right]}=\frac{1}{3\Sigma_{\mathrm{tr}}(\boldsymbol{r},E)}, \tag{2.33}$$

where $\Sigma_{\mathrm{tr}}=\Sigma_t-\Sigma_{s1}$ is the transport cross section.

Combining Fick's law with the multi-group formalism gives the steady-state multi-group diffusion equations:

$$\begin{aligned}&-\boldsymbol{\nabla}\cdot\left[D_g(\boldsymbol{r})\boldsymbol{\nabla}\phi_g(\boldsymbol{r})\right]+\Sigma_{t,g}(\boldsymbol{r})\phi_g(\boldsymbol{r})\\&=\sum_{g'=1}^{N_G}\Sigma_{s0,g'\rightarrow g}(\boldsymbol{r})\phi_{g'}(\boldsymbol{r})+\frac{\chi_g(\boldsymbol{r})}{k}\sum_{g'=1}^{N_G}(\nu\Sigma_f)_{g'}(\boldsymbol{r})\phi_{g'}(\boldsymbol{r}).\end{aligned} \tag{2.34}$$

Finally, to account for the Doppler broadening of the energy distributions in the reactor materials with increasing temperature, we modify the multi-group diffusion equations by introducing temperature dependence in the parameters [17, Ch. 2.14]

$$\begin{aligned}&-\boldsymbol{\nabla}\cdot\left[D_g(\boldsymbol{r},T)\boldsymbol{\nabla}\phi_g(\boldsymbol{r})\right]+\Sigma_{t,g}(\boldsymbol{r},T)\phi_g(\boldsymbol{r})\\&=\sum_{g'=1}^{N_G}\Sigma_{s0,g'\rightarrow g}(\boldsymbol{r},T)\phi_{g'}(\boldsymbol{r})+\frac{\chi_g(\boldsymbol{r},T)}{k}\sum_{g'=1}^{N_G}(\nu\Sigma_f)_{g'}(\boldsymbol{r},T)\phi_{g'}(\boldsymbol{r}).\end{aligned} \tag{2.35}$$

2.3 Heat transfer

This section introduces the heat transfer models used in the thesis. The description of conduction, convection, thermal conductivity, and thermal resistance follows standard heat-transfer theory, primarily as presented by Incropera et al. [18]. Of the three classical modes of heat transfer, that is conduction, convection, and radiation, only conduction and convection are included in the thermal model. Radiative heat transport is neglected.

First, the basic heat-transfer mechanisms are defined and related to the balance-equation framework. Then, the treatment of thermal conductivity is discussed, including the use of an effective conductivity for the saturated wick structure. Finally, thermal resistance networks are introduced as a reduced model for heat transfer through regions that are not resolved explicitly.

2.3.1 Heat transport mechanisms

The most direct form of thermal transport considered in the model is heat conduction. Heat conduction is the diffusive transfer of heat within or between materials. At the macroscopic scale, it is modelled using Fourier's law [18, Ch. 1.2.1]

$$\boldsymbol{q}''(\boldsymbol{r}) = -\boldsymbol{k}(\boldsymbol{r}, T) \cdot \boldsymbol{\nabla} T(\boldsymbol{r}), \tag{2.36}$$

where $\boldsymbol{k}$ is the thermal conductivity tensor and $\boldsymbol{q}''$ is the conductive heat flux. Conduction is the main form of heat transfer in the fuel assembly. Using the internal energy U as an extensive quantity, the steady balance equation can be formulated using (2.4)

$$-\nabla \cdot [\boldsymbol{k}(\boldsymbol{r}, T) \cdot \boldsymbol{\nabla} T(\boldsymbol{r})] = q'''(\boldsymbol{r}), \tag{2.37}$$

where q''' is the volumetric heat source. This assumes that the change in internal energy is only due to heat transfer.

Next, convection refers to heat transfer between a moving fluid and a bounding surface. It includes both diffusive transfer near the surface and advective transport by the fluid motion. Such heat transfer is often modelled using Newton's law of cooling [18, Ch. 1.2.2]

$$q''_{\text{conv}} = h(T_s - T_f), \tag{2.38}$$

where h is the heat-transfer coefficient, T_s is the surface temperature, and T_f is a representative fluid temperature. In the heat pipe model, this form can be used to describe heat transfer between the wick and the vapour core.

In this thesis, a distinction is made between convection and advection. The term convection is used for heat transfer between a moving fluid and a bounding surface, while advection refers specifically to the transport of thermal energy by bulk fluid motion. With this convention, heat transfer inside a fluid consists of conduction and advection. A thermal model for the vapour flow is developed in Section 2.4. The heat transfer mechanisms discussed are illustrated by the heat transfer in the evaporator of the heat pipe and are shown in Figure 2.2.

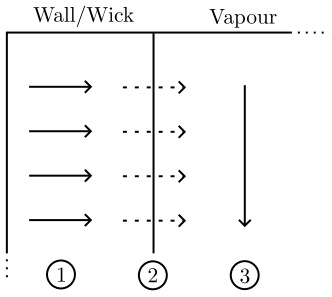

Figure 2.2: Illustration of the heat-transfer mechanisms in the heat pipe evaporator. Region 1 denotes conduction in the solid heat pipe wall and wick structure. Region 2 denotes heat transfer between the wick and vapour core, modelled as convection. Region 3 denotes conduction and advection in the vapour channel.

2.3.2 Thermal conductivity

Thermal conductivity is often assumed to be a constant scalar k, but is more accurately described by a tensorial quantity $\boldsymbol{k}(\boldsymbol{r}, T)$, dependent both on spatial position $\boldsymbol{r}$ and temperature T. In this thesis, we assume that the materials are isotropic and homogeneous, which simplifies the model of thermal conductivity to a scalar dependent on temperature $k(T)$. The conductivity models used are either purely empirical, or are supplemented with theory to describe cases which lack experimental data.

The main case where theory supplements empirical formulas has to do with the porous structure in the heat-pipe wick. A commonly used model for the effective conductivity in a wire-screen is [4, Ch. 3.2.3]

$$k_{\text{eff}}(T) = k_l(T)\frac{(k_l(T) + k_s(T)) - (1-\varphi)(k_l(T) - k_s(T))}{(k_l(T) + k_s(T)) + (1-\varphi)(k_l(T) - k_s(T))}, \tag{2.39}$$

where k_l and k_s are the thermal conductivity of the liquid and the solid material, respectively. The porosity φ is the volumetric ratio of the fluid to the entire porous structure. Since an annular wick is used in this thesis, k_{eff} refers to the conductivity only in the porous structure, and not in the gap between the porous structure and the heat-pipe wall. Instead, the gap uses the thermal conductivity of liquid sodium.

2.3.3 Thermal resistance

In this thesis, the discretised equations governing heat transfer can be viewed as a thermal resistance network. Thermal resistance networks are analogous to electrical circuits, where temperature difference ΔT and heat-transfer rate Q play roles analogous to voltage difference ΔV and electric current I, respectively. The defining relation is [18, Ch. 3.1.2]

$$Q = \frac{\Delta T}{R}, \tag{2.40}$$

where R is the thermal resistance with units $\mathrm{K\,W^{-1}}$.

2.3.3.1 The analogy to electrical circuits

For one-dimensional conduction through a plane wall of thickness L, cross-sectional area A, and thermal conductivity k, the thermal resistance is

$$R_{\text{cond}} = \frac{L}{kA}. \tag{2.41}$$

For convective heat transfer between a surface and a fluid, Newton's law of cooling gives

$$Q = hA(T_s - T_f), \tag{2.42}$$

which can be written in resistance form as

$$R_{\text{conv}} = \frac{1}{hA}. \tag{2.43}$$

Thermal resistances can be combined in the same way as electrical resistances. Resistances in series add directly,

$$R_{\text{tot}} = \sum_i R_i, \tag{2.44}$$

whereas resistances in parallel satisfy

$$\frac{1}{R_{\text{tot}}} = \sum_i \frac{1}{R_i}. \tag{2.45}$$

In this thesis, thermal resistance concepts are generally not used explicitly, although the resulting equations can be interpreted using them. They are, however, used explicitly in the treatment of the graphite moderator and the boundaries of the fuel pin and heat pipe. For the moderator, the resistance acts as an effective relation between a temperature difference and a heat-transfer rate,

$$Q = \frac{T_{\text{FP}} - T_{\text{HP}}}{R_{\text{eff}}}, \tag{2.46}$$

such that R_{eff} captures the entire moderator region. The boundaries are explained in the following.

2.3.3.2 Mixed heat transfer at boundaries

When treating boundary conditions in various heat-transfer systems, there can be two different forms of heat transfer on each side of the boundary [19, Ch. 8.6.3]. In this thesis, the relevant case is conduction in a cylindrical geometry on one side and convection on the other. Consider a hollow cylinder with height L, inner radius r_1, outer radius r_2, and conductivity k, as shown in Figure 2.3. The thermal resistance is then given by [18, Ch. 3.3.1]

$$R_{\text{cond}} = \frac{\ln(r_2/r_1)}{2\pi L k}. \tag{2.47}$$

Convection at the outer wall is given by Equation (2.43). Connecting the resistances in series, according to Equation (2.44), the total resistance is

$$R_{\text{tot}} = \frac{\ln(r_2/r_1)}{2\pi L k} + \frac{1}{2\pi L r_2 h}. \tag{2.48}$$

Equivalently, the conductance is

$$\frac{1}{R_{\text{tot}}} = \frac{1}{\frac{\ln(r_2/r_1)}{2\pi L k} + \frac{1}{2\pi L r_2 h}}. \tag{2.49}$$

2.4 Heat pipe fluid flow

This section presents the fluid-flow models used for the heat pipe. The vapour core is described by mass and momentum balance equations, together with closure relations for saturated sodium vapour. The liquid return flow through the wick is described separately using Darcy's law for porous media. Together, these models provide a reduced description of the internal heat-pipe circulation, where the vapour core is treated as a one-dimensional, saturated, compressible flow.

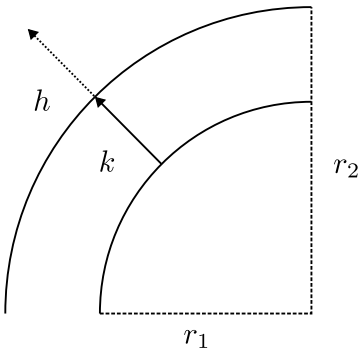

Figure 2.3: Heat transfer at the boundary of a hollow cylinder.

2.4.1 One-dimensional vapour flow

To set up the fluid balance equations, mass and axial momentum are chosen as the extensive quantities. Their corresponding densities are ρ and $\rho\boldsymbol{v}$. For mass balance, the only flux is the advective mass flux $\rho\boldsymbol{v}$. In addition, vapour may be generated or removed at the wick-vapour interface due to evaporation or condensation [4]. Let Γ denote the volumetric vapour mass source, with $\Gamma > 0$ corresponding to evaporation. The steady mass balance is then [19, Ch. 3.4]

$$\boldsymbol{\nabla} \cdot (\rho\boldsymbol{v}) - \Gamma = 0. \tag{2.50}$$

For momentum balance, the advective momentum flux is $\rho\boldsymbol{v} \otimes \boldsymbol{v}$. Furthermore, particles on the surface of the control volume can interact with the particles outside and transfer momentum. This flux is represented by the Cauchy stress tensor, which can be written in the form

$$\boldsymbol{\sigma} = -p\boldsymbol{I} + \boldsymbol{\tau}, \tag{2.51}$$

where p is pressure and $\boldsymbol{\tau}$ is the viscous stress tensor [16]. Momentum transfer associated with phase change at the wick-vapour interface is neglected. This corresponds to assuming that the mass entering or leaving the vapour core does not introduce a significant axial momentum source compared with pressure, inertia, and wall-friction effects. Neglecting body forces for the horizontal heat pipes, the steady momentum balance on conservative form becomes [19, Ch. 3.5]

$$\boldsymbol{\nabla} \cdot (\rho\boldsymbol{v} \otimes \boldsymbol{v} + p\boldsymbol{I} - \boldsymbol{\tau}) = \boldsymbol{0}. \tag{2.52}$$

In this thesis, the vapour core is modelled as one-dimensional plug flow along the z-axis. The variables are interpreted as cross-sectionally averaged quantities, and Γ represents the interfacial evaporation or condensation rate expressed per unit vapour-core volume. Equations (2.50) and (2.52) then reduce to

$$0 = \frac{\partial(\rho v)}{\partial z}(z) - \Gamma(z), \tag{2.53}$$

$$0 = \frac{\partial(\rho v^2)}{\partial z}(z) + \frac{\partial p}{\partial z}(z) - (\boldsymbol{\nabla} \cdot \boldsymbol{\tau})_z(z). \tag{2.54}$$

2.4.2 Saturation closure

To complete equations (2.53) and (2.54), closure relations are needed for ρ, p, and $\boldsymbol{\tau}$. The density and pressure of the vapour are determined from the assumption that the vapour is saturated. To this end, J. K. Fink and L. Leibowitz have reported empirical formulas relating temperature to the density and pressure of sodium vapour and liquid under saturated conditions [20]. Starting with the liquid and vapour densities, ρ_l and ρ_v, they are calculated using

$$\rho_l = \rho_c + 275.32 \cdot \left(1 - \frac{T}{T_c}\right) + 511.58 \cdot \left(1 - \frac{T}{T_c}\right)^{0.5} \qquad [\mathrm{kg\,m^{-3}}], \tag{2.55}$$

$$\rho_v = \left(\frac{h_{fg}}{T\gamma_\sigma} + \frac{1}{\rho_l}\right)^{-1} \qquad [\mathrm{kg\,m^{-3}}]. \tag{2.56}$$

Here, h_{fg} is the enthalpy of vaporisation, specified by

$$h_{fg} = 393.37\left(1 - \frac{T}{T_c}\right) + 4398.6\left(1 - \frac{T}{T_c}\right)^{0.29302} \qquad [\mathrm{kJ\,kg^{-1}}]. \tag{2.57}$$

Furthermore, γ_σ is defined as the derivative of pressure with respect to temperature along the saturation curve, $(\partial p/\partial T)_\sigma$. Empirically, it is given by

$$\gamma_\sigma = \left(\frac{12633.73}{T^2} - \frac{0.4672}{T}\right) \exp\left[11.9463 - \frac{12633.73}{T} - 0.4672 \ln T\right] \qquad [\mathrm{MPa\,K^{-1}}]. \tag{2.58}$$

The formulas above are evaluated with $\rho_c = 219.0\,\mathrm{kg\,m^{-3}}$ and $T_c = 2503.7\,\mathrm{K}$, and are recommended for use in the temperature range $371\,\mathrm{K} \leq T \leq 2503.7\,\mathrm{K}$. Regarding the vapour pressure p_v, it can be found using

$$\ln p_v = 11.9463 - 12633.73/T - 0.4672 \ln T, \tag{2.59}$$

where the recommended temperature range is $864\,\mathrm{K} \leq T \leq 2499\,\mathrm{K}$.

2.4.3 Friction closure

The remaining closure relation concerns the viscous stress $\boldsymbol{\tau}$. Consider the axial viscous force

$$F_z^{\mathrm{visc}} = \int_V (\boldsymbol{\nabla} \cdot \boldsymbol{\tau})_z \, d^3 r. \tag{2.60}$$

This force can be split into boundary contributions [21]

$$F_z^{\mathrm{visc}} = \int_{\partial V_{\mathrm{top}}} (\boldsymbol{\tau} \cdot \hat{\boldsymbol{N}})_z \, dS + \int_{\partial V_{\mathrm{bottom}}} (\boldsymbol{\tau} \cdot \hat{\boldsymbol{N}})_z \, dS + \int_{\partial V_{\mathrm{wall}}} (\boldsymbol{\tau} \cdot \hat{\boldsymbol{N}})_z \, dS, \tag{2.61}$$

where the wall refers to the open-cylinder area and the top and bottom refer to the end caps of the cylindrical heat-pipe vapour core. Next, we assume that the viscous force is wall-shear dominated

$$F_z^{\mathrm{visc}} \approx \int_{\partial V_{\mathrm{wall}}} (\boldsymbol{\tau} \cdot \hat{\boldsymbol{N}})_z \, dS. \tag{2.62}$$

Since the vapour flow is parallel to the wall, the relevant contribution to the viscous force is the shear stress tangential to the flow. For flow in the positive z-direction, this is written as $(\boldsymbol{\tau} \cdot \boldsymbol{n})_z = -\tau_w$, where τ_w is the wall shear-stress magnitude. The viscous force due to wall shear over a small axial distance Δz is [22, p. 202]

$$F_z^{\text{visc}} \approx -\tau_w 2\pi r_{\text{v}} \Delta z. \tag{2.63}$$

Comparing with equation (2.60), the force can also be written as

$$F_z^{\text{visc}} \approx (\boldsymbol{\nabla} \cdot \boldsymbol{\tau})_z \Delta V \tag{2.64}$$

when the volume is small. Using $\Delta V = \pi r_{\text{v}}^2 \Delta z$ and equating the right-hand sides of equations (2.63) and (2.64) gives

$$(\boldsymbol{\nabla} \cdot \boldsymbol{\tau})_z \approx -\frac{2\tau_w}{r_{\text{v}}}. \tag{2.65}$$

At this point, the shear-stress form of the Darcy–Weisbach equation [22, p. 202] is used:

$$\tau_w = \frac{1}{8} f_{\text{D}} \rho |v| v, \tag{2.66}$$

where f_{D} is the Darcy friction factor. Substituting equation (2.66) into equation (2.65) yields

$$(\boldsymbol{\nabla} \cdot \boldsymbol{\tau})_z \approx -f_{\text{D}} \frac{\rho |v| v}{2 D_{\text{v}}}. \tag{2.67}$$

This form is equivalent to the usual Darcy–Weisbach pressure-gradient expression for a circular tube, with hydraulic diameter $D_{\text{H}} = D_{\text{v}}$ [23].

2.5 Heat pipe operating limits

Heat pipes transport heat highly efficiently, as they are able to transport large amounts of thermal energy over relatively small temperature gradients. However, their performance is constrained by several physical limits that restrict the maximum axial heat transfer. These limits depend on factors such as the working fluid, heat pipe geometry, and operating temperature [4, Ch. 4.1]. Since this thesis focuses on developing a model of a fuel assembly in a heat-pipe-cooled reactor, it is important to present the range of efficient operating conditions for the heat pipes included in the model.

In this section, we present the relevant limitations placed on a heat pipe in a reactor environment during steady-state operation. The limitations that can only be reached during startup for liquid-metal heat pipes, such as the viscous limit, will therefore not be considered [24, Ch. 4.2.1]. The heat-transfer limitations are commonly represented in an axial heat-transfer versus operating-temperature diagram, hereafter referred to as a Q–T diagram. An example of such a diagram is shown in Figure 2.4. The possible axial heat transfer at any given temperature is restricted by the limitation corresponding to the lowest heat transfer rate. Consequently, this creates an operating region below the graphed limitations, which can be seen as the green area in the figure.

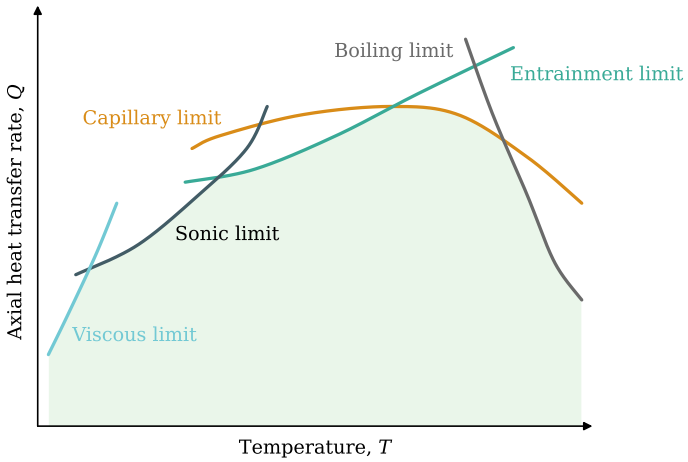

Figure 2.4: Illustration of the combined limitations placed on the working conditions of a heat pipe.

2.5.1 Sonic limit

The sonic limit occurs when the speed of the vapour transported in the interior of the heat pipe reaches velocities close to the speed of sound. This causes a shock wave that hinders further increases in the vapour velocity, which in turn inhibits the axial heat transfer from increasing. The phenomenon can be compared with a converging-diverging nozzle, where the fluid cannot exceed the speed of sound at the throat [25].

Because the sonic limit emerges from compressibility effects, the compressible vapour-flow model used in this thesis should be able to capture the conditions when the sonic limit is met. However, for validation purposes, the results are compared to a sonic-limit model derived in an article by R. Bertossi et al. [25]. Based on the assumptions of an ideal gas, negligible viscous forces, and saturated conditions along the entire heat pipe, the authors derive the expression

$$Q_{\text{sonic}} = S_v h_{fg,a} \frac{P_{v,0}}{1+\gamma} \sqrt{\frac{\gamma}{r_g T_{v,0}}} \frac{1}{\sqrt{1 - \frac{r_g}{h_{fg,a}} T_{v,a} \ln(1+\gamma)}}. \tag{2.68}$$

Here, Q is the axial heat transfer, S_v is the cross-sectional area of the vapour flow, $T_{v,a}$ is the temperature at the end of the evaporator section, $T_{v,0}$ is the temperature at the start of the evaporator section, r_g is the gas constant, $P_{v,0}$ is the pressure at the start of the evaporator section, $h_{fg,a}$ is the enthalpy of vaporisation at the end of the adiabatic section, and γ is the ratio of specific heat capacities.

2.5.2 Entrainment limit

The second relevant limitation is the entrainment limit. In a heat pipe, vapour and liquid travel in opposite directions while remaining in direct contact with each other at a liquid–vapour interface in the wick. At high vapour velocities, the shear stress at the surface becomes evident through the formation of wave crests at the surface of the liquid. For sufficiently high velocities, the wave crests grow larger to

the point where droplets are detached from the surface and become entrained into the vapour flow. This reduces the amount of liquid being transported back into the evaporator section, which can cause parts of the evaporator section to dry out, and consequently, limit the axial heat transfer capacity of the heat pipe [4, Ch. 4.4].

The entrainment limit is characterized by the Weber number We, which describes the ratio of the shear forces at the liquid–vapour interface and the liquid surface tension. The limit can be assumed to be reached when We is on the order of unity, since that indicates that the forces maintaining the liquid are equal in size to the forces that are trying to disrupt the surface [4, Ch. 4.4]. The Weber number can be expressed as

$$\mathrm{We} = \frac{2R_{h,p}\rho_v u^2}{\sigma} \tag{2.69}$$

where $R_{h,p}$ is the hydraulic radius of the wick-surface pore, ρ_v is the vapour density, u is the difference between the mean axial velocity in the liquid and the vapour, and σ is the surface tension. The mean axial velocity difference is usually substituted by the mean axial velocity of the vapour u_v, since it is often orders of magnitude larger than the liquid velocity [4, Ch. 4.4]. Translating the criterion We = 1 into a corresponding expression for the axial heat flow yields the following equation for the entrainment limit

$$Q_{\mathrm{ent}} = S_v h_{fg} \left(\frac{\sigma \rho_v}{2R_{h,p}} \right)^{\frac{1}{2}} \tag{2.70}$$

where S_v is the cross-sectional area of the vapour flow and h_{fg} is the enthalpy of vaporisation

$$Q = h_{fg} S_v \rho_v u. \tag{2.71}$$

The fluid models used in this thesis do not take the underlying physical causes of the entrainment limitation into consideration, and equation (2.70) is therefore used to represent the limit.

2.5.3 Capillary limit

The capillary limit arises from the pressure balance required to sustain steady-state circulation of the working fluid in a heat pipe. The necessary pressure head is provided by capillary forces originating from the interaction between the fluid and the wick structure, and must be large enough to overcome the pressure losses in the liquid–vapour path caused by viscous and inertial effects. For stable operation, therefore, the total pressure loss in the liquid–vapour loop must be less than or equal to the maximum capillary pressure head. If this criterion is not fulfilled, the evaporator section will not receive sufficient inflow of working fluid, leading to dry-out and rapidly increasing temperatures [24, Ch. 4.1.2].

The capillary limit can be expressed as

$$\Delta P_{\mathrm{cap,max}} \geq \Delta P_l + \Delta P_v + \Delta P_{e,\delta} + \Delta P_{c,\delta} + \Delta P_g. \tag{2.72}$$

The liquid pressure drop ΔP_l is calculated analytically, while the vapour pressure loss ΔP_v is calculated from the numerical solution using the saturation closure described in Section 2.4.2. The maximum possible capillary head, $\Delta P_{\text{cap,max}}$, is given by [24, Ch. 4.3.2.6]

$$\Delta P_{\text{cap,max}} = \frac{2\sigma}{r_{\text{eff}}} \tag{2.73}$$

where σ is the surface tension, and r_{eff} is the effective pore radius. Pressure losses at the wick–vapour interface due to evaporation and condensation, $\Delta P_{e,\delta}$ and $\Delta P_{c,\delta}$, are neglected. Likewise, the heat pipes are horizontal; effects due to gravity are thus ignored, that is ΔP_g.

Furthermore, the vapour and liquid pressure losses cannot in general be evaluated independently, since the two pressure profiles are connected through a so-called wet point. The wet point is defined as the axial position where the liquid pressure equals the vapour pressure. It therefore sets the reference point from which the liquid pressure drop through the wick and the vapour pressure drop through the vapour channel must be balanced. Consequently, the location of the wet point contributes to how much vapour pressure recovery is possible. For high cooling rates, the wet point is often located closer to the start of the condenser section, and no pressure recovery is possible, as shown in Figure 2.5a. In contrast, for low cooling rates, the wet point is located close to the end of the condenser section, and maximum pressure recovery is possible, as can be observed in Figure 2.5b [24, Ch. 4.3.5.4].

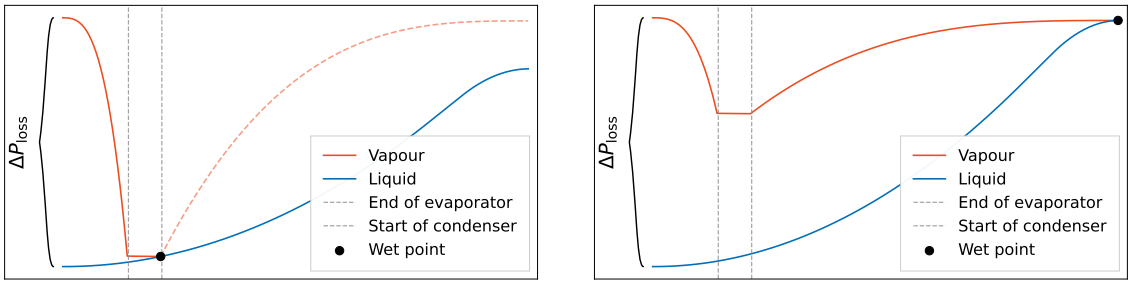

(a) Wet point close to the condenser start.

(b) Wet point close to the condenser end.

Figure 2.5: Illustration of the wet-point location for two different axial pressure drop profiles. The orange line represents the pressure drop and subsequent recovery in the vapour channel. The blue line represents the pressure drop in the liquid in the wick. The pressure drop in the vapour is enlarged to make the characteristic profile visible.

Finally, to later validate the hybrid analytical–numerical procedure used to evaluate the capillary limit, a fully analytical estimate of the vapour pressure loss is also computed for comparison. For this purpose, the model of Cotter is used. The model assumes uniform heat addition in the evaporator and uniform heat removal in the condenser, incompressible vapour flow, constant thermophysical properties, and a wet point located close to the condenser end cap [26]. Under these assumptions, the

vapour pressure loss is approximated as

$$\Delta P_v = \frac{\left(1 - \frac{4}{\pi^2}\right) Q_{\mathrm{HP}}^2}{8\rho_v R_v^4 h_{fg}^2} + \frac{8\mu_v Q_{\mathrm{HP}} L_{\mathrm{ad}}}{\pi \rho_v R_v^4 h_{fg}} \tag{2.74}$$

where Q_{HP} is the axial heat transfer rate transported by the heat pipe, ρ_v is the vapour density, R_v is the radius of the vapour interior, h_{fg} is the enthalpy of vaporisation, μ_v is the dynamic viscosity of the vapour, and L_{ad} is the length of the adiabatic section of the heat pipe.

2.5.3.1 Pressure loss in the wick

It is generally assumed that the liquid flow in the wick structure can be modelled as a 2D incompressible laminar flow with negligible body forces. In a thin wick, however, the radial flow can be neglected. Therefore, assuming that the wick is circular, homogeneous, and isotropic, and the liquid velocity and its gradients are small, the axial pressure drop can be expressed using Darcy's law for flow through a porous medium [4, Ch. 3.2.2]

$$\frac{dp_l}{dz} = \frac{\mu_l \dot{m}_l}{\rho_l S_l K}, \quad S_l = \varphi S_{\mathrm{wick}} \tag{2.75}$$

where μ_l is the liquid dynamic viscosity, ρ_l is the liquid density, K is the wick permeability, $\dot{m}_l$ is the liquid mass flow rate, S_l is the liquid cross-sectional area, and S_{wick} is the cross-sectional area of the wick.

If, instead, the wick can be assumed to be annular and there exists a gap between the wall and wick structure, the pressure drop exhibits the characteristics of annular flow due to a majority of the flow going through the gap [4, Ch. 3.2.2]. The axial pressure drop due to viscous effects can then be described by the Darcy–Weisbach equation, which states

$$\frac{dp_l}{dz} = \frac{f_l \rho_l u_{p,l}^2}{2 D_{h,l}} \tag{2.76}$$

where $D_{h,l}$ is the hydraulic diameter, u_l is the pore velocity (also known as the volumetric flux) and f_l is the friction factor for laminar flow in a concentric annulus, given by

$$f_l = \frac{64}{Re}\zeta, \quad \zeta = \frac{(r_1 - r_2)^2 (r_1^2 - r_2^2)}{r_1^4 - r_2^4 - \frac{(r_1^2 - r_2^2)^2}{\ln(r_1/r_2)}} \tag{2.77}$$

with ζ being a dimensionless correction factor for annular flow, that approaches $\frac{2}{3}$ for thin annuli. Furthermore, for convenience and ease of computation, the expressions of equations (2.75) and (2.76) can be combined to yield an effective value K_{eff} so

that equation (2.76) takes the form of Darcy's law. The form of K_{eff} can be derived to be equal to

$$K_{\text{eff}} = \frac{2R_h^2}{f\text{Re}_l} = \frac{D_h^2}{32\left(\frac{(1-R^*)^2}{1+R^{*2}-\frac{1-R^{*2}}{\ln(1/R^*)}}\right)}, \quad R^* = \frac{r_2}{r_1}. \tag{2.78}$$

The pressure drop in an annular medium then also takes the form of

$$\frac{dp_l}{dz} = \frac{\mu_l \dot{m}_l}{\rho_l S_l K_{\text{eff}}} \tag{2.79}$$

2.5.4 Boiling limit

In a scenario of high radial heat flux, the liquid in the evaporator wick can start to boil. If this boiling develops to the point of nucleate boiling, the vapour formed will cover parts of the wick and prevent the liquid from entering, causing hotspots. Furthermore, if the boiling is intense enough it can cause complete dry-out of the evaporator, which is defined as the boiling limit [4, Ch. 4.3].

Establishing a theoretical expression for the boiling limit is challenging because boiling is a physically complex phenomenon. Additionally, it is hard to base models on experimental results because small differences in geometry and materials can lead to drastically different outcomes. The boiling limit should therefore be interpreted as a rough estimate. In this work, the following expression is used [4, Ch. 4.3]

$$Q_{\text{boil}} = \frac{2\pi L_e k_{\text{wick}} \Delta T_{\text{crit}}}{\ln(R_i/R_v)}, \tag{2.80}$$

where Q_{boil} is the boiling limit axial heat transfer rate, L_e is the evaporator length, k_{wick} is the effective thermal conductivity of the wick, R_i is the inner radius of the heat pipe wall, and R_v is the radius of the vapour interior. The quantity ΔT_{crit} denotes the critical superheat and is given by

$$\Delta T_{\text{crit}} = \frac{2\sigma T_v}{h_{fg}\rho_v}\left(\frac{1}{R_b} - \frac{1}{R_{men}}\right), \tag{2.81}$$

where σ is the surface tension, T_v is the vapour temperature, h_{fg} is the enthalpy of vaporisation, ρ_v is the vapour density, R_{men} is the radius of the liquid-vapour meniscus, and R_b is the critical bubble radius. In the absence of experimental results for a specific heat pipe, the critical bubble radius can be set to 0.1 µm [4].

3

Numerical Theory

This chapter introduces the numerical theory used to discretise and solve the physical models presented in Chapter 2. The finite volume method is first described as the discretisation framework used to transform the continuous governing equations into a system of algebraic equations. Powell's dogleg method is then presented as the algorithm used to solve the resulting nonlinear system.

3.1 Finite volume method

The finite volume method (FVM) is a computational method designed to solve partial differential equations by transforming differential equations into algebraic equations through discretisation. The central idea of the discretisation process is to split the geometry into smaller control volumes, in which the relevant physical quantities are averaged, to get a discrete problem that is possible to solve numerically. Additionally, FVM exhibits several properties that make it well suited for solving transport equations, including its inherent conservation of transported quantities. The finite volume formulation presented here follows the general treatment given by Moukalled et al. [19].

The first step in the discretisation process is to split the geometrical domain of the problem into non-overlapping cells, or control volumes, to yield a mesh or grid over the geometry. Grids can vary in several attributes, including dimensionality (1D, 2D, or 3D), cell geometry (e.g. triangular, quadrilateral, or hexagonal), and topology — either structured, where all cells share the same shape, or unstructured, where cell shapes can form cell to cell. This is illustrated in Figure 3.1. Since the structure and shape of the grid are flexible, it often means that the grid can be tailored to the problem and its corresponding geometry.

The second step of the discretisation process is to adapt the continuous equations to the discrete grid by integrating them over each individual cell. The resulting integrals are then approximated at specific integration points using Gaussian quadrature. The formulation used in this thesis is cell-centred FVM, meaning that the state variables are stored at grid points located at the centroids of the control volumes. The derivation follows the procedure described by Moukalled et al. [19, Ch. 5], starting from a local steady-state transport equation for a volumetric density $a(\boldsymbol{r})$, as defined in Section 2.1. The steady-state equation is

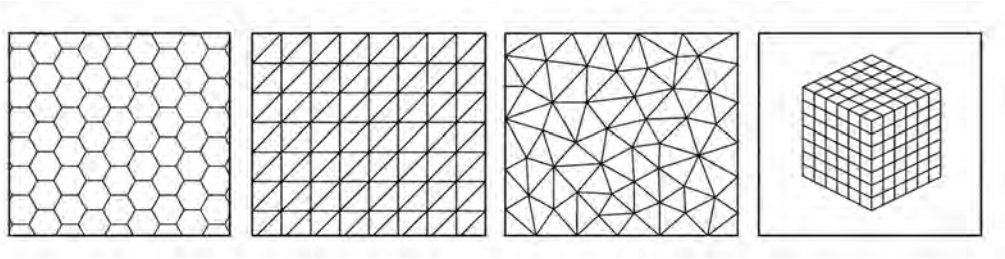

Figure 3.1: Examples of meshes with different cell geometries, dimensionalities, and topologies. From left to right: hexagonal cells in a structured grid, triangular cells in a structured grid, triangular cells in an unstructured grid, and cubic cells in a three-dimensional structured grid.

$$\boldsymbol{\nabla} \cdot \boldsymbol{J}_a^{\mathrm{tot}}(\boldsymbol{r}) - s_a(\boldsymbol{r}) = 0, \tag{3.1}$$

with

$$\boldsymbol{J}_a^{\mathrm{tot}}(\boldsymbol{r}) = a(\boldsymbol{r})\boldsymbol{v}(\boldsymbol{r}) - \alpha(\boldsymbol{r})\boldsymbol{\nabla}\Phi(\boldsymbol{r}) + \boldsymbol{J}_a^{\mathrm{other}}(\boldsymbol{r}), \tag{3.2}$$

where Φ represents the driving potential, s_a represents the volumetric source term, $\boldsymbol{v}$ is the velocity field, α is the transport coefficient, and $\boldsymbol{J}_a^{\mathrm{other}}$ represents other flux contributions.

Integrating Equation (3.1) over the volume of an arbitrary cell C and using the divergence theorem yields

$$\oint_{\partial V_C} \boldsymbol{J}_a^{\mathrm{tot}}(\boldsymbol{r}) \cdot \hat{\boldsymbol{N}}\, dS - \int_{V_C} s_a(\boldsymbol{r})\, d^3\boldsymbol{r} = 0. \tag{3.3}$$

Converting the surface integral into a sum of the total flux over all faces of the cell C, denoted as $\mathcal{F}(C)$, yields

$$\sum_{f_C \in \mathcal{F}(C)} \int_{f_C} \boldsymbol{J}_a^{\mathrm{tot}}(\boldsymbol{r}) \cdot \hat{\boldsymbol{N}}_{f_C}\, dS - \int_{V_C} s_a(\boldsymbol{r})\, d^3\boldsymbol{r} = 0. \tag{3.4}$$

Thereafter, substituting the volume and surface integrals with the corresponding Gaussian quadrature expressions, results in

$$\sum_{f_C \in \mathcal{F}(C)} \sum_{\mathrm{ip} \in \mathcal{I}(f_C)} \omega_{\mathrm{ip}} S_{f_C} \boldsymbol{J}_{a,\mathrm{ip}}^{\mathrm{tot}} \cdot \hat{\boldsymbol{N}}_{f_C} - \sum_{\mathrm{ip} \in \mathcal{I}(C)} \omega_{\mathrm{ip}} V_C a_{f,\mathrm{ip}} = 0, \tag{3.5}$$

where $\mathcal{I}(A)$ refers to all integration points of the Gaussian quadrature integration at position A and ω_{ip} is the corresponding weight to the integration point. The balance equation is now spatially discretised, as can be observed in equation (3.5), but more work is needed before we arrive at a formulation that is solvable.

A standard simplification to equation (3.5) is to approximate the sum over the integration points by a single integration point. That point represents the mean value of the quantity in the volume or on the surface. Thus, if we let C and f_C denote both the integration points on the objects and the objects themselves, the discretised steady-state balance equation then takes the form

$$\sum_{f_C \in \mathcal{F}(C)} S_{f_C} \boldsymbol{J}_{a,f_C}^{\mathrm{tot}} \cdot \hat{\boldsymbol{N}}_{f_C} - V_C s_{a,C} = 0. \tag{3.6}$$

Replacing $\boldsymbol{J}_{a,f_C}^{\text{tot}}$ with the different fluxes in Equation (3.2) results in

$$\sum_{f_C \in \mathcal{F}(C)} S_{f_C} \left[(\boldsymbol{v}a)_{f_C} - (\alpha \boldsymbol{\nabla} \Phi)_{f_C} + \boldsymbol{J}_{a,f_C}^{\text{other}} \right] \cdot \hat{\boldsymbol{N}}_{f_C} - V_C s_{a,C} = 0. \tag{3.7}$$

Two main difficulties remain. No explicit relationship has been defined to evaluate $\nabla\Phi$ based on the cell-centre values of Φ. Secondly, in cell-centred FVM, the values of $\boldsymbol{v}$, a, and α are evaluated in the cell centres, but the flux terms require face values. The remaining two subsections describe the approaches used to address these issues, while the additional flux contribution $\boldsymbol{J}_a^{\text{other}}$ is treated separately according to the specific problem considered.

3.1.1 Gradient approximation

The face value of the gradient required in the diffusive flux term is approximated differently depending on whether the grid is orthogonal or non-orthogonal. Consider a cell A across face a and neighbouring cell C, as shown in Figure 3.2. For a structured, orthogonal grid, the face normal $\hat{\boldsymbol{N}}_f$ and the unit vector $\widehat{\boldsymbol{CF}}$ are parallel. A gradient evaluated on the face f_C is defined as a finite difference between the cell-centre value Φ_C and the neighbouring cell-centre value Φ_F [19, Ch. 8.1]. Applying this to the diffusion term in Equation (3.7) then yields

$$(\alpha \boldsymbol{\nabla} \Phi)_{f_C} \cdot \hat{\boldsymbol{N}}_{f_C} S_{f_C} = \alpha_{f_C} \frac{\Phi_F - \Phi_C}{d_{CF}} \widehat{\boldsymbol{CF}} \cdot \hat{\boldsymbol{N}}_{f_C} S_{f_C} = \alpha_{f_C} \frac{\Phi_F - \Phi_C}{d_{CF}} S_{f_C}. \tag{3.8}$$

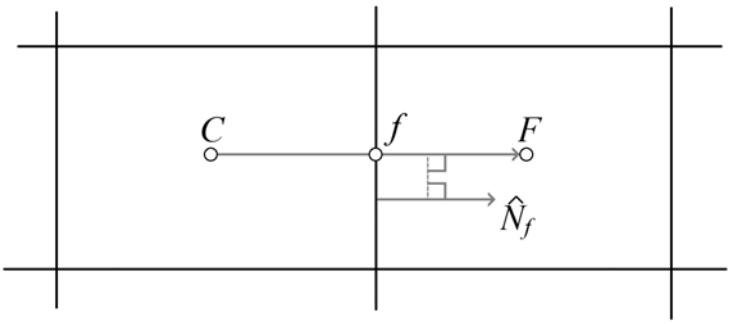

Figure 3.2: The figure depicts a structured orthogonal grid where the vector connecting the neighbouring cell centres C and F is collinear with the face normal $\hat{\boldsymbol{N}}_{f_C}$.

However, for non-orthogonal grids the gradient normal to the surface cannot be written as a function of only Φ_C and Φ_F, since it has a component perpendicular to $\widehat{\boldsymbol{CF}}$, as can be observed in Figure 3.3. Instead, it is separated into two terms [19, Ch. 8.6]

$$\begin{aligned}(\alpha \boldsymbol{\nabla} \Phi)_{f_C} \cdot \hat{\boldsymbol{N}}_{f_C} S_{f_C} &= (\alpha \boldsymbol{\nabla} \Phi)_{f_C} \cdot \widehat{\boldsymbol{CF}} \, S_{f_C} + (\alpha \boldsymbol{\nabla} \Phi)_{f_C} \cdot (\hat{\boldsymbol{N}}_{f_C} - \widehat{\boldsymbol{CF}}) \, S_{f_C} \\ &= \alpha_{f_C} \frac{\Phi_F - \Phi_C}{d_{CF}} S_{f_C} + (\alpha \boldsymbol{\nabla} \Phi)_{f_C} \cdot \boldsymbol{T}_{f_C},\end{aligned} \tag{3.9}$$

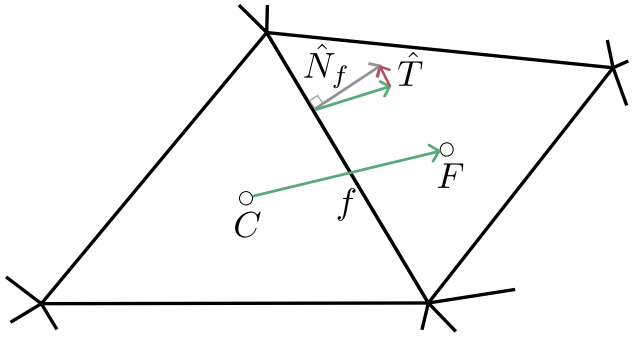

Figure 3.3: Illustration of the non-orthogonal contribution to the face-normal gradient on an unstructured grid. The vector connecting the cell centres C and F is not aligned with the face normal $\hat{\boldsymbol{N}}_{f_C}$, causing the diffusive flux through the face f_C to be decomposed into an orthogonal contribution along $\widehat{\boldsymbol{CF}}$ and a correction contribution along $\hat{\boldsymbol{T}}_{f_C}$.

where $\boldsymbol{T}_{f_C}$ is defined as

$$\boldsymbol{T}_{f_C} = S_{f_C}\hat{\boldsymbol{T}}_{f_C} = S_{f_C}(\hat{\boldsymbol{N}}_{f_C} - \widehat{\boldsymbol{CF}}). \tag{3.10}$$

The second term in equation (3.9), called the cross-diffusion correction, can be expressed as a function of only the face-centred values of Φ for all neighbours of C and F [19, Ch. 8.6.6]. This is based on the Green-Gauss method and results in the following expression

$$\begin{aligned}(\alpha\boldsymbol{\nabla}\Phi)_{f_C}\cdot\boldsymbol{T}_{f_C} = \alpha_{f_C}\Bigg[&g_C\left(\frac{1}{V_C}\sum_{f'_C\in\mathcal{F}(C)}\Phi_{f'_C}S_{f'_C}\hat{\boldsymbol{N}}_{f'_C}\right)\\ &+g_F\left(\frac{1}{V_F}\sum_{f_F\in\mathcal{F}(F)}\Phi_{f_F}S_{f_F}\hat{\boldsymbol{N}}_{f_F}\right)\Bigg]\cdot\boldsymbol{T}_{f_C}.\end{aligned} \tag{3.11}$$

where V_C and V_F are the volumes of the cells C and F, respectively. The quantities g_C and g_F are geometric interpolation factors defined as

$$g_C = \frac{d_{fF}}{d_{Cf}+d_{fF}}, \qquad g_F = \frac{d_{Cf}}{d_{Cf}+d_{fF}}. \tag{3.12}$$

Here, d_{Cf} and d_{fF} represent the distances from the centre of face f to the cell centres C and F, respectively.

3.1.2 Interpolation scheme

There is a myriad of interpolation schemes that can be used to determine the face-centred values based on the cell-centre values, each with its corresponding combination of numerical attributes. The choice of interpolation scheme depends on the type of problem, and accuracy required, among other things. In this thesis, two different schemes were used: the central difference scheme and the first-order upwind scheme.

Diffusive interpolation scheme

There is no directional preference in a diffusive flux, as the flux is based only on differences in the driving potential. The interpolation scheme should reflect this property and should provide an accurate approximation of the diffusive flux at the face, independent of which side the flux is evaluated from. For a general face f in a structured grid, shared by the cells C and F, this condition is equivalent to [19, Ch. 8.4]

$$(\alpha \boldsymbol{\nabla} \Phi)_f \cdot \hat{\boldsymbol{N}}_f = \frac{\Phi_F - \Phi_f}{d_{fF}/\alpha_F} \stackrel{!}{=} \frac{\Phi_f - \Phi_C}{d_{Cf}/\alpha_C}, \tag{3.13}$$

where Φ_C and Φ_F are the cell-centre values of the driving potential, while Φ_f is the face-averaged driving potential. The quantities d_{Cf} and d_{fF} denote the distances from the centre of the face f to the cell centres C and F, respectively. Similarly, α_F and α_C are the corresponding cell-centre values of the transport coefficient.

Equations (3.13) can be rewritten as

$$\Phi_F - \Phi_C = (\alpha \boldsymbol{\nabla} \Phi)_f \cdot \hat{\boldsymbol{N}}_f \left(\frac{d_{Cf}}{\alpha_C} + \frac{d_{fF}}{\alpha_F} \right), \tag{3.14}$$

which can be compared to the expression for the gradient, given by equation (3.8)

$$\Phi_F - \Phi_C = (\alpha \boldsymbol{\nabla} \Phi)_f \cdot \hat{\boldsymbol{N}}_f \left(\frac{d_{CF}}{\alpha_f} \right). \tag{3.15}$$

Equating the two expressions gives the following result.

$$\frac{d_{CF}}{\alpha_f} = \frac{d_{Cf}}{\alpha_C} + \frac{d_{fF}}{\alpha_F}. \tag{3.16}$$

Finally, solving for the face transport coefficient yields

$$\alpha_f = \frac{d_{CF}}{\dfrac{d_{Cf}}{\alpha_C} + \dfrac{d_{fF}}{\alpha_F}}. \tag{3.17}$$

Thus, the face value of the transport coefficient is obtained as a distance-weighted harmonic average of the neighbouring cell-centred values.

Advective interpolation scheme

The central difference scheme used for diffusive quantities is not suitable for directional phenomena such as advection. This is because it assigns equal weight to both cells that share a face, regardless of the direction of transport. Advection, however, is inherently directional, as it represents transport by a velocity field. Consequently, applying a central difference scheme to advection-dominated problems can introduce numerical errors and lead to unphysical results. A compatible alternative for the advective term is the first-order upwind scheme [19, Ch. 11.2.4].

Suppose that a quantity A is interpolated on a grid of cell centres and faces using the first-order upwind scheme, as shown in Figure 3.4. The value A_f is then defined by the direction of transport

$$A_f = \begin{cases} A_C, & v_{CF} \geq 0, \\ A_F, & v_{CF} < 0. \end{cases} \tag{3.18}$$

This means that the face-centred value A_f takes the upstream cell-centre value. This is more consistent with the physics of advection, where information is transported downstream with the flow.

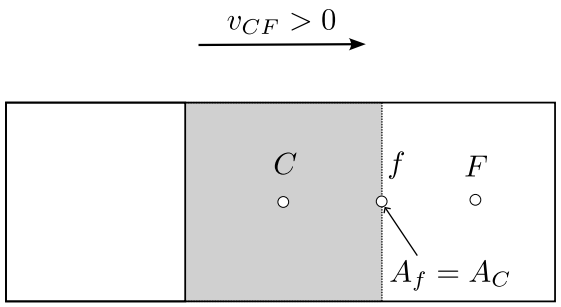

Figure 3.4: Illustration of the first-order upwind scheme for a one-dimensional structured grid. The face value A_f is taken from the upstream cell, determined by the sign of the velocity field at the face v_{CF}.

3.2 Numerical solver

Combining the models for neutron transport, heat transfer, and fluid dynamics and discretising them via the FVM described above yields a system of nonlinear equations. These equations govern the fuel-assembly's behaviour, and the reactor operating state remains unknown until a physically meaningful solution is found.

The nonlinear solver employed in this thesis is the MINPACK implementation of the iterative hybrid method, called Powell's dogleg method [27]. The specifics of the algorithm are well covered by K. Madsen et al. [28, Chapter 3.3]. The general idea of the method is to reformulate the original system of equations, which can be described as

$$\boldsymbol{f}(\boldsymbol{x}^*) = \boldsymbol{0}, \quad \boldsymbol{f} : \mathbb{R}^n \to \mathbb{R}^n, \tag{3.19}$$

into a linear least-squares minimisation problem, where the aim is to minimise $||\boldsymbol{f}(\boldsymbol{x})||$, or equivalently, to find

$$\boldsymbol{x}^* = \text{argmin}_{\boldsymbol{x}}[F(\boldsymbol{x})], \tag{3.20}$$

where

$$F(\boldsymbol{x}) = \frac{1}{2}\sum_{i=1}^{n}(f_i(\boldsymbol{x}))^2 = \frac{1}{2}\boldsymbol{f}(\boldsymbol{x})^T\boldsymbol{f}(\boldsymbol{x}). \tag{3.21}$$

The minimisation is then carried out iteratively by constructing a sequence of approximations $\{\boldsymbol{x}_k\}$, where each new iterate is obtained by adding a step $\boldsymbol{h}_k$ to the current point $\boldsymbol{x}_k$. The step is chosen to reduce the objective function $F(\boldsymbol{x})$ and, hopefully, so that the sequence converges towards a minimiser $\boldsymbol{x}^*$

$$\boldsymbol{x}_{k+1} = \boldsymbol{x}_k + \boldsymbol{h}_k. \tag{3.22}$$

There are different types of methods for generating the step $\boldsymbol{h}_k$, each with different strengths and weaknesses. Powell's dogleg method is a hybrid method because it uses two different methods to generate step candidates: Gauss–Newton and steepest descent. The final step is then selected using a trust-region criterion. The reason for using this combination of methods is that Gauss–Newton converges efficiently near the minimiser, whereas steepest descent is more reliable further away from the solution.

Gauss–Newton generates a new step by applying the least-squares method to a linearised objective function. Specifically, we expand $F(\boldsymbol{x}+\boldsymbol{h})$ around $\boldsymbol{x}$ and truncate after the first derivative

$$\begin{aligned} F(\boldsymbol{x}+\boldsymbol{h}) &= \frac{1}{2}\boldsymbol{f}(\boldsymbol{x}+\boldsymbol{h})^T\boldsymbol{f}(\boldsymbol{x}+\boldsymbol{h}) \\ &\approx \frac{1}{2}(\boldsymbol{f}(\boldsymbol{x})+\boldsymbol{J}(\boldsymbol{x})\boldsymbol{h})^T(\boldsymbol{f}(\boldsymbol{x})+\boldsymbol{J}(\boldsymbol{x})\boldsymbol{h}) \\ &= F(\boldsymbol{x}) + \boldsymbol{h}^T\boldsymbol{J}(\boldsymbol{x})^T\boldsymbol{f}(\boldsymbol{x}) + \frac{1}{2}\boldsymbol{h}^T\boldsymbol{J}(\boldsymbol{x})^T\boldsymbol{J}(\boldsymbol{x})\,\boldsymbol{h}. \end{aligned} \tag{3.23}$$

The Jacobian $\boldsymbol{J}(\boldsymbol{x})$ of $\boldsymbol{f}(\boldsymbol{x})$ is defined by

$$(\boldsymbol{J}(\boldsymbol{x}))_{ij} = \frac{\partial f_i}{\partial x_j}(\boldsymbol{x}), \quad \boldsymbol{J} \in \mathbb{R}^{n\times n}. \tag{3.24}$$

Given that the Jacobian is of full rank, it can be shown that there is a unique value for $\boldsymbol{h}$ that minimises Equation (3.23). This value is found by solving the normal equation

$$\boldsymbol{J}(\boldsymbol{x})^T\boldsymbol{J}(\boldsymbol{x})\,\boldsymbol{h}_{gn} = -\boldsymbol{J}(\boldsymbol{x})^T\boldsymbol{f}(\boldsymbol{x}). \tag{3.25}$$

The solution, denoted by $\boldsymbol{h}_{gn}$, defines the Gauss–Newton step.

The steepest descent method instead first computes the direction in which $F(\boldsymbol{x})$ locally decreases most rapidly, and then calculates a step length. The direction of steepest descent can be shown to be

$$\boldsymbol{h}_{sd} = -F'(\boldsymbol{x}) = -\boldsymbol{J}(\boldsymbol{x})^T\boldsymbol{f}(\boldsymbol{x}), \tag{3.26}$$

while $F(\boldsymbol{x}+\alpha\boldsymbol{h}_{sd})$ can be minimised by choosing α as

$$\alpha = -\frac{\boldsymbol{h}_{sd}{}^T\boldsymbol{J}(\boldsymbol{x})^T\boldsymbol{f}(\boldsymbol{x})}{||\boldsymbol{J}(\boldsymbol{x})\boldsymbol{h}_{sd}||^2}. \tag{3.27}$$

With both steps calculated, the selection process can be described as follows. First, set $\boldsymbol{h}_k = \boldsymbol{h}_{gn}$ if $\boldsymbol{h}_{gn}$ is within the trust region, which is defined as a sphere with radius Δ around $\boldsymbol{x}_k$. Second, if $\|\boldsymbol{h}_{\mathrm{gn}}\| \not\leq \Delta$ and the scaled steepest-descent step $\alpha\boldsymbol{h}_{sd}$ lies outside the trust region, take a step of length Δ in the steepest descent direction. The third alternative is a combination of the two steps and is shown in Figure 3.5. The selection criterion can also be expressed as

$$\boldsymbol{h}_k = \begin{cases} \boldsymbol{h}_{\mathrm{gn}}, & \|\boldsymbol{h}_{\mathrm{gn}}\| \leq \Delta, \\ \Delta \dfrac{\boldsymbol{h}_{\mathrm{sd}}}{\|\boldsymbol{h}_{\mathrm{sd}}\|}, & \|\boldsymbol{h}_{\mathrm{gn}}\| \not\leq \Delta \text{ and } \|\alpha\boldsymbol{h}_{\mathrm{sd}}\| \geq \Delta, \\ \alpha\boldsymbol{h}_{\mathrm{sd}} + \beta\left(\boldsymbol{h}_{\mathrm{gn}} - \alpha\boldsymbol{h}_{\mathrm{sd}}\right), & \|\boldsymbol{h}_{\mathrm{gn}}\| \not\leq \Delta \text{ and } \|\alpha\boldsymbol{h}_{\mathrm{sd}}\| \not\geq \Delta, \end{cases} \tag{3.28}$$

where β is chosen such that

$$\|\boldsymbol{h}_k\| = \Delta. \tag{3.29}$$

Finally, the MINPACK implementation does not require an exact Jacobian. Instead, the Jacobian is initially approximated using a forward difference strategy and is subsequently updated using Broyden's rank-one method [27].

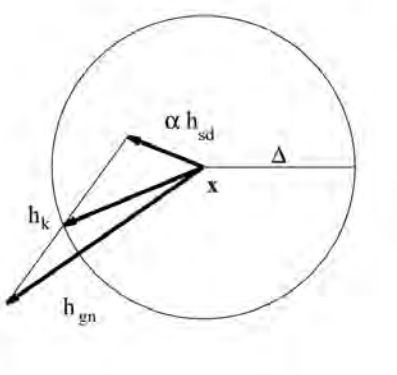

Figure 3.5: Example of the step $\boldsymbol{h}_k$ produced in Powell's dogleg method if $\|\boldsymbol{h}_{\mathrm{gn}}\| \not\leq \Delta$ and $\|\alpha\boldsymbol{h}_{\mathrm{sd}}\| \not\geq \Delta$. The illustration is borrowed from K. Madsen et al. with updated notation and the approval of the authors.

4

Numerical Implementations

This chapter describes the numerical implementation of the individual components that are part of the coupled fuel-assembly model: the heat pipe, the fuel pin, the moderator, and the neutronics model. For each component model, the chosen spatial discretisation is first introduced by presenting the mesh used to represent the relevant geometry. The governing equations are then adapted to the corresponding discrete form, followed by a description of how the boundary conditions are imposed. Finally, each numerical model is compared with either analytical solutions or experimental data.

4.1 Heat pipe model

Two coupled submodels constitute the heat-pipe model: the two-dimensional wall–wick conduction and the one-dimensional vapour flow. Conduction is modelled using an internal-energy balance without any volumetric heat sources, while the vapour flow is modelled using mass and momentum balance. Full saturation of the liquid and the vapour is assumed, in addition to the assumption that friction pressure losses in the vapour can be described by Darcy–Weisbach. The two submodels are coupled via conjugate heat transfer through the wick–vapour interface.

4.1.1 Mesh

The heat pipe is discretised using a structured two-dimensional axial–radial mesh for the wall–wick geometry, combined with a one-dimensional staggered axial mesh for the vapour region. Unlike the mesh used for the fuel pin, later described in Section 4.2, the heat-pipe mesh uses an equal-length discretisation, which means that all cells have equal radial and axial lengths Δr and Δz, as is illustrated in Figure 4.1.

The staggered cell formulation consists of two principles: the mass and momentum balance equations are integrated over control volumes that are offset by half a cell length, and the state variables are stored at different locations. Scalar quantities are stored at the centres of the mass-control volumes, while vectorial quantities are stored at the centres of the momentum-control volumes [19, Ch. 15.2.4]. Figure 4.2 illustrates the staggered grid when temperature T and velocity v are the state variables. The staggered grid is used to avoid decoupling that can occur between alternating cells on a collocated grid, which is referred to as a chequerboard problem [19, Ch. 15.2.3].

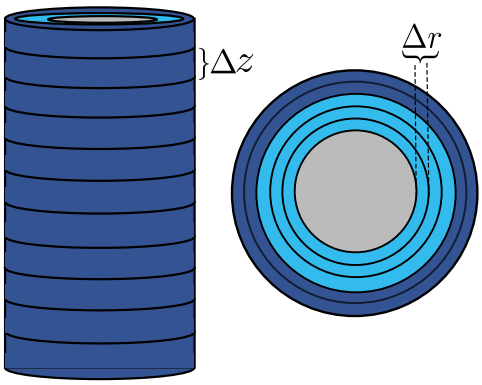

Figure 4.1: Example of a mesh used to represent a heat pipe, from both a near-axial and a radial perspective. The figure shows that the cells are distributed with equal radial and axial lengths Δr and Δz. The cells coloured in darker and lighter blue are the wall-wick cells, while the grey area in the centre is the vapour interior.

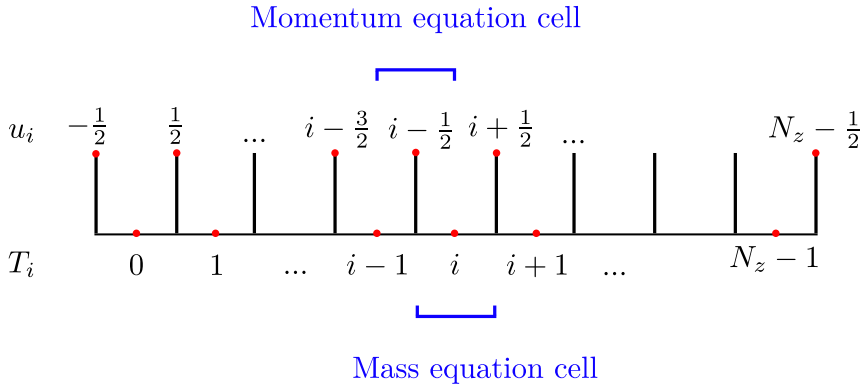

Figure 4.2: Illustration of the staggered grid used for the vapour flow model. The temperatures are stored at the centres of the mass-control volumes, indexed by integer values i, while the velocities are stored at the centres of the momentum-control volumes, indexed by half-integer values $i \pm \frac{1}{2}$.

4.1.2 Discretisation of the wall-wick conduction model

Heat transfer in the heat-pipe wall and wick is modelled as pure conduction without any heat sources. The gap in the annular wick is included in the same conductive description, since convective effects are negligible compared with conduction for liquid metals [29]. Using Equation (2.37), the steady-state conduction equation is thus given by

$$\nabla \cdot [k(T)\nabla T] = 0. \tag{4.1}$$

The state variable chosen to represent the system is the temperature T. Thermal conductivity is modelled using experimental data and depends on the specific material. In the wick, the conductivity is replaced by the effective wick conductivity described in Section 2.3.2.

Integrating Equation (4.1) over a control volume C and applying the FVM framework yields

$$\sum_{f \in \mathcal{F}(C)} S_f k_f \nabla T_f \cdot \hat{\boldsymbol{N}}_f = 0, \tag{4.2}$$

where $\mathcal{F}(C)$ is the set of faces belonging to cell C, S_f is the area of face f, $\hat{\boldsymbol{N}}_f$ is its outward unit normal, and $k_f = k(T_f)$ is the thermal conductivity evaluated at the face. Since the mesh is structured and orthogonal, the gradient ∇T_f can be approximated using Equation (3.8)

$$\nabla T_f \cdot \hat{\boldsymbol{N}}_f = \frac{T_F - T_C}{d_{CF}}. \tag{4.3}$$

Here, C and F are the two neighbouring cell centres and d_{CF} is the distance between them. The corresponding conductivity is evaluated using the harmonic average

$$k_f = \frac{d_{CF}}{\dfrac{d_{Cf}}{k_C} + \dfrac{d_{fF}}{k_F}}, \tag{4.4}$$

where d_{Cf} is the distance from the centre of cell C to the face f, and d_{fF} is the distance from the face f to the centre of cell F.

Substituting Equations (4.3) and (4.4) into Equation (4.2) gives the discrete conduction balance for the heat-pipe wall and wick[1]

$$\sum_{f \in \mathcal{F}(C)} \frac{S_f}{\dfrac{d_{Cf}}{k_C} + \dfrac{d_{fF_f}}{k_{F_f}}} \left(T_{F_f} - T_C \right) = 0. \tag{4.5}$$

4.1.3 Discretisation of the vapour flow model

The vapour flow in the interior of the heat pipe is modelled as a one-dimensional, saturated, compressible flow in the axial direction. The corresponding balance equations are derived in Section 2.4 and are written as follows[2]:

$$0 = \frac{\partial(\rho(T)v)}{\partial z} - \Gamma, \tag{4.6}$$

$$0 = \frac{\partial(\rho(T)v^2)}{\partial z} + \frac{\partial p(T)}{\partial z} + \frac{f_{\mathrm{D}}(T)}{2D_{\mathrm{H}}} \rho(T) v |v|. \tag{4.7}$$

Here, v is the mean axial vapour velocity, Γ is the source of volumetric vapour mass, D_{H} is the hydraulic diameter, and f_{D} is the Darcy friction factor. The state variables are the velocity v and the temperature T, since it has been reported that temperature provides better numerical stability than pressure p for the cell-centred state variable [2].

[1] The neighbour F_f varies with the face f.

[2] The explicit dependence on the axial position z is not written out explicitly.

4.1.3.1 Mass equation

Integrating Equation (4.6) over the mass cell and applying the finite-volume approximation gives

$$\sum_{f\in\mathcal{F}(C_i)} (\rho v)_f \, S_f - V_i \Gamma_i = 0, \tag{4.8}$$

where C_i denotes the mass control volume centred at T_i, V_i is the corresponding cell volume, and S_f is the area of face f. Since the vapour flow is one dimensional and the cross-sectional area is constant, Equation (4.8) reduces to

$$\rho(T_{i+\frac{1}{2}})v_{i+\frac{1}{2}} - \rho(T_{i-\frac{1}{2}})v_{i-\frac{1}{2}} - \Delta z \Gamma_i = 0. \tag{4.9}$$

No interpolation is required for the velocities because they are stored at the mass-cell faces. However, we must use the interpolation scheme to express the temperatures on the faces, since they are stored at the mass-cell centres. Using the first-order upwind scheme for positive flow direction, introduced in Section 3.1.2, the density at each cell face is taken from the upstream cell. Thus,

$$\rho(T_{i+\frac{1}{2}}) = \rho(T_i), \qquad \rho(T_{i-\frac{1}{2}}) = \rho(T_{i-1}). \tag{4.10}$$

Equation (4.9) is then written as

$$\rho(T_i)v_{i+\frac{1}{2}} - \rho(T_{i-1})v_{i-\frac{1}{2}} - \Delta z \Gamma_i = 0. \tag{4.11}$$

4.1.3.2 Momentum equation

Moving on with momentum, integrating Equation (4.7) over the momentum cell and applying the finite-volume approximation results in

$$\sum_{f\in\mathcal{F}(C_{i-\frac{1}{2}})} S_f \left[\rho(T)v^2 + p(T)\right]_f + V_{i-\frac{1}{2}} \frac{f_{\mathrm{D},i-\frac{1}{2}}}{2D_{\mathrm{v}}} \rho(T_{i-\frac{1}{2}}) v_{i-\frac{1}{2}} |v_{i-\frac{1}{2}}| = 0, \tag{4.12}$$

where $C_{i-\frac{1}{2}}$ denotes the momentum control volume centred at $v_{i-\frac{1}{2}}$. For the one-dimensional geometry and the constant surface areas, this is equivalent to

$$\begin{aligned} 0 = {} & \left(\rho(T)v^2\right)_i - \left(\rho(T)v^2\right)_{i-1} + p(T_i) - p(T_{i-1}) \\ & + \Delta z \frac{f_{\mathrm{D},i-\frac{1}{2}}}{2D_{\mathrm{v}}} \rho(T_{i-\frac{1}{2}}) v_{i-\frac{1}{2}} |v_{i-\frac{1}{2}}|. \end{aligned} \tag{4.13}$$

Using the first-order upwind scheme for positive flow direction

$$\left(\rho(T)v^2\right)_i = \rho(T_i)v^2_{i-\frac{1}{2}}, \quad \left(\rho(T)v^2\right)_{i-1} = \rho(T_{i-1})v^2_{i-\frac{3}{2}}, \quad \rho(T_{i-\frac{1}{2}}) = \rho(T_{i-1}), \tag{4.14}$$

Equation (4.13) is taken to be

$$\begin{aligned} 0 = {} & \rho(T_i)v^2_{i-\frac{1}{2}} - \rho(T_{i-1})v^2_{i-\frac{3}{2}} + p(T_i) - p(T_{i-1}) \\ & + \Delta z \frac{f_{\mathrm{D},i-\frac{1}{2}}}{2D_{\mathrm{v}}} \rho(T_{i-1}) v_{i-\frac{1}{2}} |v_{i-\frac{1}{2}}|. \end{aligned} \tag{4.15}$$

The friction factor is evaluated locally from the Reynolds number

$$f_{\mathrm{D},i-\frac{1}{2}} = f_{\mathrm{D}}\Big(\mathrm{Re}_{i-\frac{1}{2}}\Big), \qquad \mathrm{Re}_{i-\frac{1}{2}} = \frac{|v_{i-\frac{1}{2}}|\rho(T_{i-1})D_{\mathrm{v}}}{\mu(T_{i-1})}. \tag{4.16}$$

The density and viscosity at the momentum location are obtained from the neighbouring temperature cells using the same upwind convention as for the advective terms. The Darcy friction factor is approximated using the Hagen–Poiseuille relation in the laminar regime and the Blasius correlation in the turbulent regime [22, 30]. The resulting piecewise model is given by

$$f_{\mathrm{D}} = \begin{cases} \dfrac{64}{\mathrm{Re}}, & \mathrm{Re} < 2000, \\ \dfrac{0.316}{\mathrm{Re}^{1/4}}, & \mathrm{Re} > 3000. \end{cases} \tag{4.17}$$

Together, Equations (4.11) and (4.15) form the discrete vapour-flow system solved in the implementation.

4.1.4 Boundary conditions

So far, the governing equations for the wall–wick and vapour models have been described. It remains to specify the boundary conditions at the external heat-pipe boundaries and the coupling condition at the wick–vapour interface. The external boundary conditions are based mainly on [31, 2], while the wick–vapour coupling is based on [29].

We first introduce a general finite-volume form for boundary contributions in the wall–wick region. Consider a cell C with faces $f \in \mathcal{F}(C)$ and boundary faces $b \in \mathcal{B}(C)$. Heat transfer through internal faces is treated by conduction, while heat transfer through boundary faces is represented by boundary contributions Q_b. The discrete balance can then be written as

$$\sum_{f\in\mathcal{F}(C)\setminus\mathcal{B}(C)} \frac{S_f}{\dfrac{d_{Cf}}{k_C} + \dfrac{d_{fF_f}}{k_{F_f}}} \Big(T_{F_f} - T_C\Big) + \sum_{b\in\mathcal{B}(C)} Q_b = 0. \tag{4.18}$$

Here, the sign convention is that $Q_b > 0$ corresponds to heat entering cell C through boundary face b.

External boundary conditions

The axial end caps are assumed to be insulated. Therefore, for boundary faces at the axial ends of the wick and wall,

$$Q_b = 0. \tag{4.19}$$

For the vapour model, the axial velocity is set to zero at both end caps, corresponding to impermeable axial boundaries.

The boundary condition at the outer radial wall depends on the axial region of the heat pipe:

Evaporator. At the evaporator outer wall, an inward heat flux q''_{evap} is prescribed. With the sign convention introduced above, the boundary contribution is

$$Q_b = q''_{\text{evap}} S_b, \tag{4.20}$$

where S_b is the boundary-face area.

Adiabatic section. The adiabatic section is assumed to be insulated in the radial direction. Hence, there is no heat transfer through the outer radial boundary, and

$$Q_b = 0. \tag{4.21}$$

Condenser. In the condenser region, heat is removed from the outer wall by convection to the environment. The environment is represented by a fixed temperature T_{env} and a convective heat-transfer coefficient h_{env}.

For the condenser boundary condition, the wall temperature T_C is stored at the centre of the cell rather than at the external boundary face. This means that the convective boundary comes after conduction through a half cell. This is the mixed boundary condition explained in Section 2.3.3.2. Using Equation (2.49), the heat transfer through boundary b is therefore

$$Q_b = \frac{1}{\frac{\ln(r_b/r_C)}{2\pi\Delta z k_C} + \frac{1}{2\pi\Delta z r_b h_{\text{env}}}} (T_{\text{env}} - T_C). \tag{4.22}$$

Coupling to the vapour mass source

The wall–wick region is coupled to the vapour through heat transfer at the inner radial boundary. From the point of view of the wall–wick energy balance, this coupling has the same resistance form as the convective condenser boundary condition. Heat transfer in the form of evaporation and condensation in the wick is modelled using Newton's law of cooling, with the extra thermal resistance contribution from conducting heat through half of a cell. The heat transfer from the neighbouring vapour cell B into the cell C, through the boundary face b, is therefore

$$Q_b = \frac{1}{\frac{\ln(r_C/r_b)}{2\pi\Delta z k_C} + \frac{1}{2\pi\Delta z r_b h_{\text{vap}}}} (T_{\text{B}} - T_C). \tag{4.23}$$

Unlike the fixed environment temperature at the condenser, the vapour temperature T_B is not predetermined and is not constant across the wick–vapour boundary. Rather, the vapour temperature depends on the centre-cell temperature of the adjacent vapour cell.

From the point of view of the vapour, the coupling is seen as a volumetric mass generation/loss Γ_B rather than as a boundary condition. This is because the vapour model is one-dimensional, so heat transfer across the wick–vapour boundary is represented through the resulting boiling or condensation of saturated vapour. The heat transfer in Equation (4.23) is converted into a vapour mass source in the adjacent vapour-cell volume V_B according to

$$\Gamma_B = -\frac{Q_b}{h_{fg,B} V_B}. \tag{4.24}$$

The enthalpy of vaporisation $h_{fg,B} = h_{fg}(T_B)$ is given by Equation (2.57). The negative sign stems from the sign convention adopted in Equation (4.18), such that $\Gamma_B > 0$ represents evaporation, while $\Gamma_B < 0$ represents condensation.

4.1.5 Benchmark against experimental data

To validate the numerical heat-pipe model, the model predictions are compared with experimental temperature data from Ivanovskii et al. [1], and a simple estimate of the maximum Mach number, for four different heat-pipe configurations. The comparison is shown in Figure 4.3 and the method for estimating the Mach number is described in Appendix C.1. The main model uses the empirical relations from J. K. Fink et al. [20] to achieve saturation closure, while the comparison model replaces the empirical relations with the ideal gas law and the Clausius-Clapeyron relation; see Appendix C.2 for a derivation of the second model. A comparison between the two models is made mainly because the temperatures in the Ivanovskii experiments are outside the recommended range for the empirical formulas in Section 2.4.2.

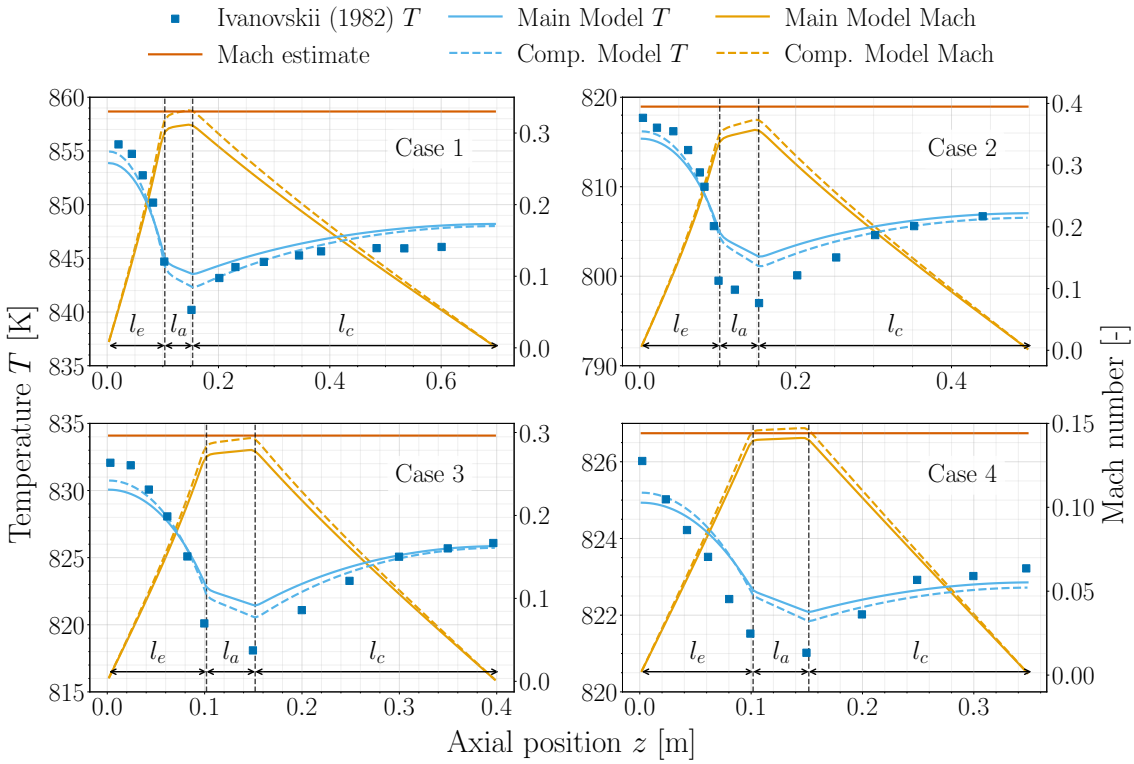

Figure 4.3: Comparison between model predictions and Ivanovskii temperature data [1] for four heat loads. The blue markers show the experimental vapour-temperature data, while the solid and dashed curves show the main model and comparison model. The flat line represents the Mach estimate.

The models capture the main axial temperature trends observed in the experiments, including the temperature decrease from the evaporator towards the adiabatic/condenser transition and the subsequent temperature recovery in the condenser region. However, there is a visible discrepancy between the experimental and predicted tem-

peratures. This means that the predicted pressure losses in the vapour fall short of the experimentally observed pressure losses.

The exact source of discrepancies between the model predictions and the experimental data is difficult to determine. Possible contributions include uncertainties in the thermophysical data, idealised model assumptions, and an unknown radial distribution of the axial velocity. Additionally, the experimental vapour temperatures are recorded at the wick–vapour interface rather than as cross-sectionally averaged temperatures.

Compared with a prior study [2], the temperature and velocity predictions in the vapour in cases 1 and 2 with a prior study, show that there is a noticeable difference in the temperature amplitude and the maximum Mach number. In the study, a similar cross-sectional averaging method was used, but the resulting temperature distribution matched the experimental data more closely. The predicted Mach number was approximately 0.55 in case 2, which neither agrees with the present model predictions nor the estimate provided in this thesis. We therefore fail to replicate the results from the prior study.

The data used to obtain the results in Figure 4.3 are presented in Table 4.1. A uniform heat-flux profile is imposed over the evaporator outer surface. The corresponding evaporator heat flux is therefore

$$q''_{\mathrm{evap}} = \frac{Q_{\mathrm{e}}}{S_{\mathrm{e}}}. \tag{4.25}$$

Table 4.1: Data used for the heat pipe validation cases.

Quantity	**Case 1**	**Case 2**	**Case 3**	**Case 4**	**Unit**
Vapour radius, R_{v}	7	7	7	7	mm
Wick thick., δ_{wick}	0.25	0.25	0.4	0.4	mm
Gap thick., δ_{gap}	0.25	0.25	0.5	0.5	mm
Wall thick., δ_{wall}	1	1	1	1	mm
Evap. length, l_{e}	10	10	10	10	cm
Adiab. length, l_{a}	5	5	5	5	cm
Cond. length, l_{c}	55	35	25	20	cm
Vapour HTC, h_{v}	10^6	10^6	10^6	10^6	$\mathrm{W\,m^{-2}\,K^{-1}}$
Env. HTC, h_{env}	62.6	59.6	84.5	54.14	$\mathrm{W\,m^{-2}\,K^{-1}}$
Env. temp., T_{env}	300	300	300	300	K
Evap. heat, Q_{e}	1000	560	615	315	W
Porosity, φ	0.7	0.7	0.7	0.7	–

4.2 Fuel pin model

The fuel pin model refers specifically to the thermal model of the fuel pin. Heat transfer is modelled by conduction and volumetric heat sources in the fuel from interactions with neutrons. Similar to the heat pipe model, the heat transfer equations are internal balance equations.

4.2.1 Mesh

The fuel-pin geometry is discretised using a two-dimensional axial–radial mesh over the fuel, gap, and cladding regions. In the fuel region, the radial face positions are distributed such that each radial fuel cell has equal volume. The cell centre is then placed so that the annular volume between the inner face and the centre is equal to the annular volume between the centre and the outer face. For a general cell C, this requires

$$\pi \left[r_C^2 - \left(r_C - d_{Cf}^{\text{inner}} \right)^2 \right] = \pi \left[\left(r_C + d_{Cf}^{\text{outer}} \right)^2 - r_C^2 \right], \tag{4.26}$$

where r_C is the radial position of the cell centre, while d_{Cf}^{inner} and d_{Cf}^{outer} denote the distances from the cell centre to the inner and outer radial faces, respectively. This corresponds to the conventional radial discretisation used in fuel-pin modelling [16, Ch. 5.5]. While equal-volume radial spacing is used in the fuel region, the gap and cladding regions are instead discretised using equal-length discretisation. In addition, the mesh uses equal-length discretisation axially, resulting in the mesh shown in Figure 4.4.

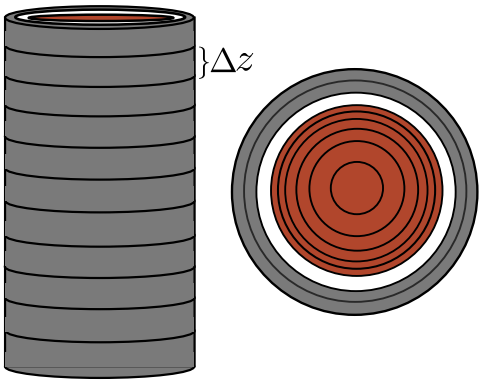

Figure 4.4: Example of a fuel pin mesh, from both a near-axial and a radial perspective, with the equal-volume radial spacing in the red fuel-pin region, and equal-length radial spacing in the gap and cladding areas, coloured white and dark grey respectively. The axial equal-length discretisation with cell length Δz is also visible.

4.2.2 Discretisation of equations

Heat transfer in the fuel pin is modelled as conduction with volumetric heat sources due to fission. The corresponding steady-state conduction equation is given by

$$-\nabla \cdot [k(T)\nabla T] = q''', \tag{4.27}$$

where the volumetric heat source q''' represents heat generated by fission in the fuel region. No fission occurs in the gap and cladding, which means that $q''' = 0$ in those regions.

The fuel-pin calculations are performed on a mesh with the same structure as the heat-pipe mesh, namely a two-dimensional structured cylindrical mesh discretised in the axial and radial directions. Consequently, the finite-volume discretisation follows analogously from the heat-pipe formulation, with the main difference being the presence of a volumetric heat source in the fuel region. The resulting discrete conduction balance is given by

$$\sum_{f \in \mathcal{F}(C)} \frac{S_f k_f}{d_{CF_f}} \left(T_{F_f} - T_C\right) = -q'''_C V_C. \tag{4.28}$$

4.2.3 Boundary conditions

For a fuel-pin cell C with faces $f \in \mathcal{F}(C)$ and boundary faces $b \in \mathcal{B}(C)$, the internal conduction and heat source contributions are given by Equation (4.28), while the boundary heat transfer is added by a separate contribution Q_b

$$\sum_{f \in \mathcal{F}(C) \setminus \mathcal{B}(C)} \frac{S_f k_f}{d_{CF_f}} \left(T_{F_f} - T_C\right) + \sum_{b \in \mathcal{B}(C)} Q_b = -q'''_C V_C. \tag{4.29}$$

The sign convention is that $Q_b > 0$ corresponds to heat entering the fuel pin cell through the boundary.

The axial end caps of the fuel pin are assumed to be insulated, which implies $Q_b = 0$ at the axial boundaries. The inner radial boundary, $r = 0$, is also insulated with $Q_b = 0$, but this is simply a requirement from the symmetry in the fuel pin and not due to any external influence. The outer radial boundary is treated analogously to the condenser boundary of the heat pipe, but with the environment replaced by the surrounding moderator. The moderator is represented by the temperature T_{mod} and the heat-transfer coefficient h_{mod}[3]. For an outer radial boundary face b, the conductive and convective resistances are written as

$$R_{\text{cond,mod}} = \frac{\ln\left(R_{\text{clad}}/r_C\right)}{2\pi k_C l_C}, \qquad R_{\text{mod}} = \frac{1}{h_{\text{mod}} S_b}. \tag{4.30}$$

The moderator boundary condition is therefore

$$Q_{b_C} = \frac{1}{R_{b,\text{mod}}}(T_{\text{mod}} - T_C), \quad R_{b,\text{mod}} = R_{\text{cond,mod}} + R_{\text{mod}}. \tag{4.31}$$

[3]This coefficient can represent imperfect contact or simply conduction between two materials. In this thesis we set it to $1\,\text{MW}\,\text{K}^{-1}\,\text{m}^{-2}$. This means that the boundary is effectively a Dirichlet boundary with temperature T_{mod}.

4.2.4 Validation

The two-dimensional numerical fuel-pin model is validated against a multi-layer analytical one-dimensional model, described by Equations (4.32) and (4.33), based on [18, Ch. 3.3.1, 3.5.2]. The two models are comparable because, with a constant volumetric heat source q''', the numerical 2D model effectively reduces to a one-dimensional radial model with no axial heat transport.

$$\begin{aligned} T_{\text{fuel}}(r) &= T_{\text{gap}}(R_{\text{fuel}}) + \frac{q'''}{4k_{\text{fuel}}}\left(R_{\text{fuel}}^2 - r^2\right), && 0 \le r \le R_{\text{fuel}}, \\ T_{\text{gap}}(r) &= T_{\text{clad}}(R_{\text{gap}}) + \frac{q'}{2\pi k_{\text{gap}}}\ln\left(\frac{R_{\text{gap}}}{r}\right), && R_{\text{fuel}} < r \le R_{\text{gap}}, \\ T_{\text{clad}}(r) &= T_{\text{mod}} + \frac{q'}{2\pi h_{\text{mod}} R_{\text{clad}}} + \frac{q'}{2\pi k_{\text{clad}}}\ln\left(\frac{R_{\text{clad}}}{r}\right), && R_{\text{gap}} < r \le R_{\text{clad}}. \end{aligned} \tag{4.32}$$

In the above, q''' and q' are defined using the total power P

$$q''' = \frac{P}{\pi R_{\text{fuel}}^2 L}, \qquad q' = \frac{P}{L} = q'''\pi R_{\text{fuel}}^2. \tag{4.33}$$

Figure 4.5 shows the comparison between the numerical and analytical solutions, while Table 4.2 lists the verification input parameters. For each cell, the error is computed as the difference between the numerical cell-centre temperature and the corresponding volume-averaged analytical solution. The two models agree well, with a maximum error of 0.16 K over a total temperature drop of approximately 220 K. Since the error is expected to increase with radial cell size, the largest deviations occur in the innermost part of the mesh, where the quadratic radial discretisation of the fuel produces the largest cells [19, Ch. 5.4.2].

Table 4.2: Input constants used for the layered fuel-pin analytical validation case.

Quantity	**Value**	**Unit**
Pin length, L	1.5	m
Fuel outer radius, R_{fuel}	9.0×10^{-3}	m
Gap outer radius, R_{gap}	1.2×10^{-2}	m
Cladding outer radius, R_{clad}	1.5×10^{-2}	m
Gap thickness, δ_{gap}	3.0×10^{-3}	m
Cladding thickness, δ_{clad}	3.0×10^{-3}	m
Fuel thermal conductivity, k_{fuel}	2.97	$\text{W m}^{-1}\,\text{K}^{-1}$
Gap effective thermal conductivity, k_{gap}	9.0	$\text{W m}^{-1}\,\text{K}^{-1}$
Cladding thermal conductivity, k_{clad}	25.87	$\text{W m}^{-1}\,\text{K}^{-1}$
Moderator heat-transfer coefficient, h_{mod}	1.0×10^{4}	$\text{W m}^{-2}\,\text{K}^{-1}$
Moderator temperature, T_{mod}	1.0×10^{3}	K
Total generated power, P	1.0×10^{4}	W

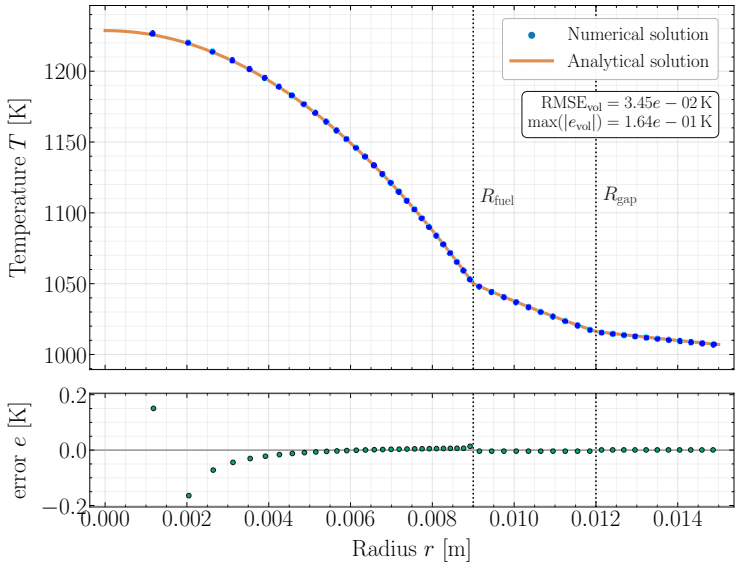

Figure 4.5: Comparison between the numerical solution and the analytical solution of the fuel pin model specified in Table 4.2. The error is computed by comparing the numerical cell-centre values with the corresponding volume-averaged analytical solution over each cell.

4.3 Moderator model

The moderator model refers to the discretised thermal model of the moderator unit cell. Heat transfer is modelled solely by conduction without any heat sources. The numerics are more involved compared to the heat pipe and the fuel pin due to the geometry. Consequently, the detailed model is later transformed into an effective model used for the reactor.

4.3.1 Mesh

The moderator geometry is more complicated than both the heat-pipe and fuel-pin geometries, and therefore requires a more flexible mesh. An unstructured triangular mesh is used for this purpose, since it can accommodate the irregular geometry and can be generated using available meshing tools, such as *Gmsh*, which is used in this thesis [32]. To increase the effective mesh resolution without increasing the total number of triangles, symmetry is used to reduce the moderator region to a section corresponding to one twelfth of the full moderator, as illustrated in Figure 4.6. The mesh is shown in Figure 4.7.

4.3.2 Discretisation of equations

Heat transfer in the moderator is modelled as pure conduction. The corresponding steady-state balance equation is given by Equation (2.37), without any volumetric heat source

$$-\nabla \cdot [k(T)\nabla T] = 0. \tag{4.34}$$

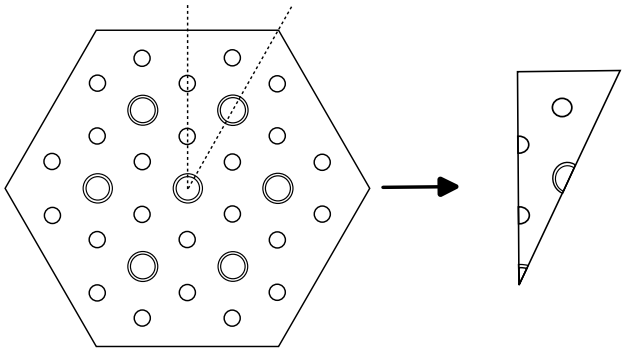

Figure 4.6: The symmetry reduction of the moderator geometry.

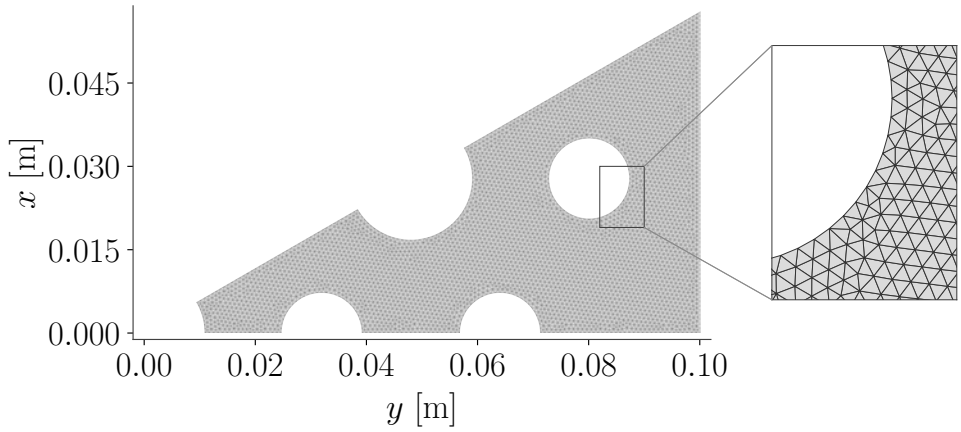

Figure 4.7: Unstructured mesh with triangular cells used for the discretisation of the moderator geometry. The mesh contains 9492 triangular cells in total.

The thermal conductivity is a scalar because the moderator graphite is assumed to be isotropic.

Since the moderator is discretised using an unstructured triangular mesh, the finite-volume formulation must account for non-orthogonal face contributions in the gradient approximation. Using the cross-diffusion correction introduced in Equation (3.9), conduction through a surface $\hat{\boldsymbol{N}}_f \, S_f$ can be expressed as

$$(k(T)\nabla T)_f \cdot \hat{\boldsymbol{N}}_f \, S_f = k_f \frac{T_F - T_C}{d_{CF}} S_f + (k\nabla T)_f \cdot \boldsymbol{T}_f. \tag{4.35}$$

The discrete conduction balance can now be written as

$$\sum_{f \in \mathcal{F}(C)} \frac{S_f k_f}{d_{CF_f}} \left(T_{F_f} - T_C \right) = - \sum_{f \in \mathcal{F}(C)} (k\nabla T)_f \cdot \boldsymbol{T}_f. \tag{4.36}$$

where the cross-diffusion contribution is treated as a source-like correction term. The correction is computed using the expression introduced in Equation (3.11), giving

$$(k\nabla T)_f \cdot \boldsymbol{T}_f = k_f \Bigg[g_C \left(\frac{1}{V_C} \sum_{f' \in \mathcal{F}(C)} T_{f'} S_{f'} \hat{\boldsymbol{N}}_{f'} \right) + g_F \left(\frac{1}{V_F} \sum_{f' \in \mathcal{F}(F)} T_{f'} S_{f'} \hat{\boldsymbol{N}}_{f'} \right) \Bigg] \cdot \boldsymbol{T}_f. \tag{4.37}$$

The moderator heat transport equations were solved iteratively, with the cross-diffusion being based on the previous solution. This was done to improve convergence rates for the solutions [19, Ch. 8.6.5].

4.3.3 Boundary conditions

For a moderator cell C with faces $f \in \mathcal{F}(C)$ and boundary faces $b \in \mathcal{B}(C)$, the internal conductive contributions are written using the same finite-volume form as in Equation (4.36). The boundary heat transfer is then added by a separate contribution Q_b, giving

$$\sum_{f \in \mathcal{F}(C) \setminus \mathcal{B}(C)} \frac{S_f k_f}{d_{CF_f}} \left(T_{F_f} - T_C \right) + \sum_{b \in \mathcal{B}(C)} Q_b = - \sum_{f \in \mathcal{F}(C)} (k\nabla T)_f \cdot \boldsymbol{T}_f. \tag{4.38}$$

The sign convention is that $Q_b > 0$ corresponds to heat entering the moderator cell through the boundary.

The moderator boundary condition is split into three separate regions: heat-pipe boundaries, fuel-pin boundaries, and moderator–moderator boundaries. The three different regions are colour-coded in Figure 4.8. The choice of boundary conditions for the moderator region stems from trial and error, with the final combination of boundary conditions exhibiting solutions that seemed the most physical. Comparison with future experiments or more detailed numerical models would likely show that the choice of boundary conditions has room for improvement.

The boundary contributions are defined as follows:

Moderator–moderator boundaries. The moderator–moderator boundary, marked in black, is based on the assumption that there are negligible temperature variations between the twelve symmetric regions in the fuel assembly and the neighbouring fuel assemblies. Under this assumption, the net heat transfer across the boundary vanishes, giving

$$Q_b = 0. \tag{4.39}$$

Heat-pipe boundaries. The heat-pipe boundary regions, marked in blue and denoted HP, are treated as mixed boundary conditions. However, the moderator boundary is not cylindrical since the boundary elements are triangular. The

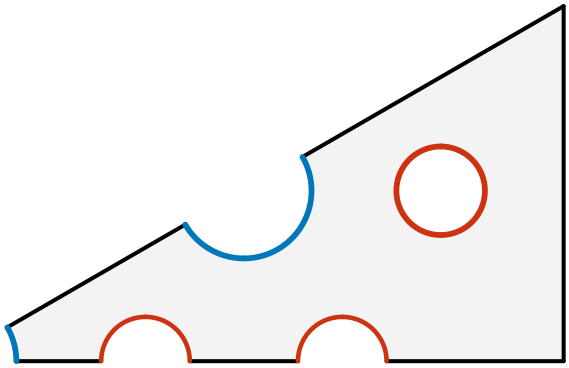

Figure 4.8: Illustration of the moderator boundary sections and their corresponding boundary conditions. Red sections indicate fuel-pin boundaries with imposed Neumann heat-flux conditions, blue sections indicate heat-pipe boundaries with mixed boundary conditions, and black sections indicate moderator–moderator boundaries treated as insulated.

half-cell thermal resistance is therefore expressed as the thermal resistance of a slab according to Equation (2.41), as

$$R_{\text{cond,HP}} = \frac{d_{Cb}}{k_C S_b}. \tag{4.40}$$

The heat-transfer resistance at the heat-pipe interface is

$$R_{\text{HP}} = \frac{1}{h_{\text{HP}} S_b}. \tag{4.41}$$

Combining these two resistances gives the total moderator–heat-pipe boundary resistance, and the boundary contribution is therefore

$$Q_b = \frac{1}{R_{b,\text{HP}}} \left(T_{\text{HP},i} - T_C\right), \qquad R_{b,\text{HP}} = R_{\text{cond,HP}} + R_{\text{HP}}. \tag{4.42}$$

Fuel-pin boundaries. The fuel-pin boundary conditions, marked in red and denoted FP, use Neumann boundary conditions. This gives

$$Q_b = q''_{b,\text{FP}} S_b, \tag{4.43}$$

where S_b is the boundary surface area of the triangular cell.

4.3.4 Validation

To the authors' knowledge, no public experimental or numerical data are available for the temperature profile of the moderator cell with the specified geometry. The validation is therefore directed towards the unstructured-grid implementation using a simplified slab geometry for which an analytical solution exists. Specifically, the

implementation is compared against the analytical temperature profile for a slab with a positive heat flux applied at the boundary $x = 0$ and a fixed temperature imposed at $x = L_x$, as given in Equation (4.44) [18, Ch. 3.1.1]. Since the geometry and boundary conditions introduce variation only in the x-direction, the analytical solution is independent of the remaining spatial dimensions.

$$T(x) = \frac{q''}{k}\left(L_x - x\right), \qquad 0 \leq x \leq L_x. \tag{4.44}$$

The numerical solution can be observed in two dimensions in Figure 4.9, while the comparison between the numerical solution and the analytical solution can be seen in Figure 4.10. The error shown in Figure 4.10 is computed as the difference between the numerical cell-centre temperature and the analytical temperature evaluated at the corresponding cell-centre x-coordinate. The comparison indicates good agreement between the two models with a small maximum error of 0.035 K, over a total temperature drop of 250 K.

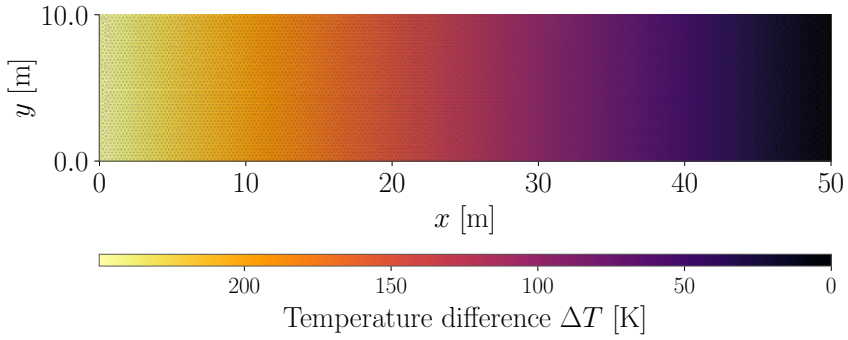

Figure 4.9: A colour-field map of the two-dimensional numerical solution to the one-dimensional heat transport problem.

Table 4.3: Input constants used for the rectangular unstructured FVM validation case.

Quantity	**Value**	**Unit**
Length, L_x	50.0	m
Height, L_y	10.0	m
Thermal conductivity, k	20.0	$\mathrm{W\,m^{-1}\,K^{-1}}$
Heat input, Q_{in}	1.0×10^3	W
Left boundary condition, $q''(x = 0)$	$\frac{Q_{\text{in}}}{L_y}$	$\mathrm{W\,m^{-1}}$
Right boundary condition, $T(x = L_x)$	0	K
Top and bottom boundary conditions, $y = 0,\ L_y$	Insulated	–

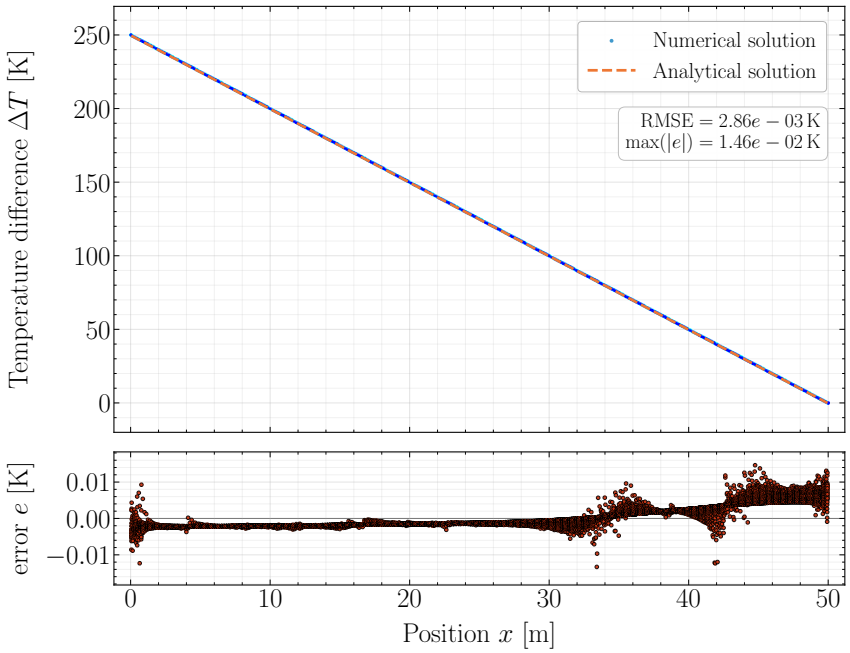

Figure 4.10: Comparison of the numerical and analytical solution of the one-dimensional slab heating simulation. The error shown in the lower graph is computed from the difference between the analytical solution at the cell centre x-axis position and the numerical cell-centre temperature value.

4.4 Neutron transport model

To model the neutronics in the fuel assembly, the multi-group diffusion equation, derived in Section 2.2.3, is used. Homogenised neutronic data are used to numerically solve for the neutron flux and are later generated when the coupled fuel assembly is considered.

The neutronics model is discretised on a structured one-dimensional mesh in the axial direction. The cells are uniformly spaced with width Δz, with constant cross-sectional area S, and have volume $V = S\Delta z$.

4.4.1 Discretisation of equations

The neutron balance is described by the steady-state multi-group diffusion equation, as detailed in Section 2.2. For energy group g, the equation is written as

$$\begin{aligned} &-\nabla \cdot [D_g(\boldsymbol{r}, T)\nabla\phi_g(\boldsymbol{r})] + \Sigma_{t,g}(\boldsymbol{r}, T)\phi_g(\boldsymbol{r}) \\ &= \sum_{g'=1}^{N_G} \Sigma_{s0,g'\to g}(\boldsymbol{r}, T)\phi_{g'}(\boldsymbol{r}) + \frac{\chi_g(\boldsymbol{r}, T)}{k_{\text{eff}}} \sum_{g'=1}^{N_G} (\nu\Sigma_f)_{g'}(\boldsymbol{r}, T)\phi_{g'}(\boldsymbol{r}). \end{aligned} \tag{4.45}$$

The neutronics model is discretised using a one-dimensional axial mesh with cells indexed by i. Applying the finite-volume discretisation to the multi-group diffusion equation for energy group g, by integrating over a cell with index i and no boundary

faces, gives

$$\begin{aligned} &- \sum_{f_i \in \mathcal{F}(i)} (D\nabla\phi)_{g,f_i} \cdot \hat{\boldsymbol{N}}_{f_i} S + V\, \Sigma_{t,g,i}\, \phi_{g,i} \\ &= V \sum_{g'=1}^{N_G} \Sigma_{s0,g'\to g,i}\, \phi_{g',i} + V\, \frac{\chi_{g,i}}{k_{\text{eff}}} \sum_{g'=1}^{N_G} \left(\nu\Sigma_f\right)_{g',i} \phi_{g',i}. \end{aligned} \tag{4.46}$$

In the previous equation, the temperature dependence remains, but is not stated for notational clarity. Since the mesh is structured, the gradient in the diffusive term can be approximated directly, without any correction term. Writing out the sum over the face contributions, and using the uniform axial spacing Δz together with the cell volume $V_i = S_i \Delta z$ introduced in the mesh definition, gives

$$\begin{aligned} &- \left[\frac{D_{g,i-\frac{1}{2}} S}{\Delta z}(\phi_{g,i-1} - \phi_{g,i}) + \frac{D_{g,i+\frac{1}{2}} S}{\Delta z}(\phi_{g,i+1} - \phi_{g,i})\right] + V\, \Sigma_{t,g,i}\, \phi_{g,i} \\ &= V \sum_{g'=1}^{N_G} \Sigma_{s0,g'\to g,i}\, \phi_{g',i} + V\, \frac{\chi_{g,i}}{k_{\text{eff}}} \sum_{g'=1}^{N_G} \left(\nu\Sigma_f\right)_{g',i} \phi_{g',i}. \end{aligned} \tag{4.47}$$

The subscripts $i + \frac{1}{2}$ and $i - \frac{1}{2}$ denote the face-centre values at the upper and lower face of cell i, respectively. The diffusive coefficient at the face is calculated using the harmonic average introduced for the diffusive interpolation scheme in section 3.1.2, with

$$D_{i\pm\frac{1}{2}} = \frac{\Delta z}{\frac{\Delta z}{2D_i} + \frac{\Delta z}{2D_{i\pm1}}} = \frac{2D_i D_{i\pm1}}{D_i + D_{i\pm1}}. \tag{4.48}$$

Furthermore, Equation (4.47) can be divided by the cell volume $V = S\Delta z$, and simplified by grouping the diffusion terms according to the cell-centre scalar fluxes

$$\begin{aligned} &\left[(a^+_{g,i} + a^-_{g,i})\phi_{g,i} + b_{g,i}\phi_{g,i+1} + c_{g,i}\phi_{g,i-1}\right] + \Sigma_{t,g,i}\, \phi_{g,i} \\ &= \sum_{g'=1}^{N_G} \Sigma_{s0,g'\to g,i}\, \phi_{g',i} + \frac{\chi_{g,i}}{k_{\text{eff}}} \sum_{g'=1}^{N_G} \left(\nu\Sigma_f\right)_{g',i} \phi_{g',i}. \end{aligned} \tag{4.49}$$

where $a_{g,i}$, $b_{g,i}$, and $c_{g,i}$ are defined according to

$$\begin{aligned} a^+_{g,i} = \frac{2D_i D_{i+1}}{(\Delta z)^2(D_i + D_{i+1})}, \quad a^-_{g,i} = \frac{2D_i D_{i-1}}{(\Delta z)^2(D_i + D_{i-1})} \\ b_{g,i} = \frac{2D_i D_{i+1}}{(\Delta z)^2(D_i + D_{i+1})} \\ c_{g,i} = \frac{2D_i D_{i-1}}{(\Delta z)^2(D_i + D_{i-1})} \end{aligned} \tag{4.50}$$

4.4.2 Boundary conditions

For the first and last axial cells, one face lies on the boundary of the geometry and the gradient term cannot be approximated using the cell-centre values, as in Equation (4.47). Instead, the gradient on the boundary is evaluated using the Marshak boundary condition. It is an adaptation of the no-reentry boundary condition to diffusion theory and can be written as [16, Ch 4.1.d]

$$\phi_{g,i\pm\frac{1}{2}} + 2(D\nabla\phi)_{g,i\pm\frac{1}{2}} \cdot \hat{\boldsymbol{N}}_{i\pm\frac{1}{2}} = 0, \tag{4.51}$$

for the upper and lower boundary cells. To use this condition in the cell-centred discretisation, the face-centre scalar flux $\phi_{g,i\pm\frac{1}{2}}$ must be eliminated in favour of the cell-centre flux $\phi_{g,i}$. This is done by approximating the gradient on the inner side of the boundary face as

$$(D\nabla\phi)_{g,i\pm\frac{1}{2}} \cdot \hat{\boldsymbol{N}}_{i\pm\frac{1}{2}} = D_{g,i}\frac{\phi_{g,i\pm\frac{1}{2}} - \phi_{g,i}}{\Delta z/2}. \tag{4.52}$$

Substituting this expression back into Equation (4.51), solving for $\phi_{g,i\pm\frac{1}{2}}$, and substituting back into the expression above gives the boundary gradient directly in terms of the cell-centred scalar flux,

$$(D\nabla\phi)_{g,i\pm\frac{1}{2}} \cdot \hat{\boldsymbol{N}}_{i\pm\frac{1}{2}} = \underbrace{\left(\frac{2D_{g,i}}{\Delta z(\Delta z + 4D_{g,i})}\right)}_{\equiv m_{g,i}} \phi_{g,i}. \tag{4.53}$$

The Marshak boundary condition therefore enters the balance equation as an additional coefficient term in the expanded sum, which is proportional to the cell-centred flux. For the two axial boundary cells, the missing neighbour contribution is removed and replaced by the contribution from $m_{g,i}\phi_{g,i}$. The discretised multi-group equation for these cells can therefore be written as

$$\begin{aligned}&\left[(a^+_{g,i} + a^-_{g,i} + m_{g,i})\phi_{g,i} + b_{g,i}\phi_{g,i+1} + c_{g,i}\phi_{g,i-1}\right] + \Sigma_{t,g,i}\,\phi_{g,i} \\ &= \sum_{g'=1}^{N_G} \Sigma_{s0,g'\to g,i}\,\phi_{g',i} + \frac{\chi_{g,i}(T_i)}{k_{\text{eff}}} \sum_{g'=1}^{N_G} \left(\nu\Sigma_f\right)_{g',i}\phi_{g',i}.\end{aligned} \tag{4.54}$$

For the bottom cell there is no lower neighbour, which means that $a^-_{g,i} = c_{g,i} = 0$. Similarly, for the top cell there is no upper neighbour, and $a^+_{g,i} = b_{g,i} = 0$.

Even with the Marshak boundary conditions applied, the amplitude of the scalar neutron flux remains undetermined. This is because the continuous multi-group diffusion equations, and hence their discretised form, is a homogeneous eigenvalue problem. Consequently, all source terms are proportional to the flux itself, and no independent or external source fixes its absolute magnitude. The scalar flux is therefore determined only up to an arbitrary multiplicative constant. This difficulty is resolved by fixing the amplitude through normalising the solution to the prescribed fuel-pin power, as

$$P_{\text{FP}} = \sum_{g}^{N_G}\sum_{i}^{N_Z} \kappa_{g,i}\Sigma_{f,g,i}\phi_{g,i}V_i \tag{4.55}$$

4.4.3 Validation

The numerical multi-group diffusion implementation is compared to an analytical solution of the two-group neutron diffusion equation in a homogenous slab, detailed by Equations (4.56) and (4.57). The analytical equations are presented in the form expressed in [33, Ch. 5.c], while the solution process follows the treatment in Lamarsh[17, Ch. 10.2].

$$\begin{aligned} D_1 \frac{d^2\phi_1}{dx^2}(x) + \left(\frac{\nu\Sigma_{f,1}}{k_{\text{eff}}} - \Sigma_{a,1} - \Sigma_r \right) \phi_1(x) + \frac{\nu\Sigma_{f,2}}{k_{\text{eff}}} \phi_2(x) = 0, \\ D_2 \frac{d^2\phi_2}{dx^2}(x) + \Sigma_r \phi_1(x) - \Sigma_{a,2} \phi_2(x) = 0, \end{aligned} \tag{4.56}$$

where the removal cross-section Σ_r is defined as

$$\Sigma_r(x) = \Sigma_{s0,1\to2} - \Sigma_{s0,2\to1} \frac{\phi_2(x)}{\phi_1(x)}. \tag{4.57}$$

The comparison was carried out with two energy groups for the numerical implementation, over a one-dimensional mesh of 75 cells, with the input parameters defined in Table 4.4. The comparison is presented in Figure 4.11. The figure shows that the two solutions agree well, with a maximum relative error of 0.0201 %, and 0.149 % for energy group 1 and 2, respectively. The two values for the multiplication factor, k_{eff}, differ with a value of 0.39 pcm. The error is computed from the difference between the average analytical value in the cell and the numerical cell-centre value, all divided by the maximum value of the corresponding group scalar flux.

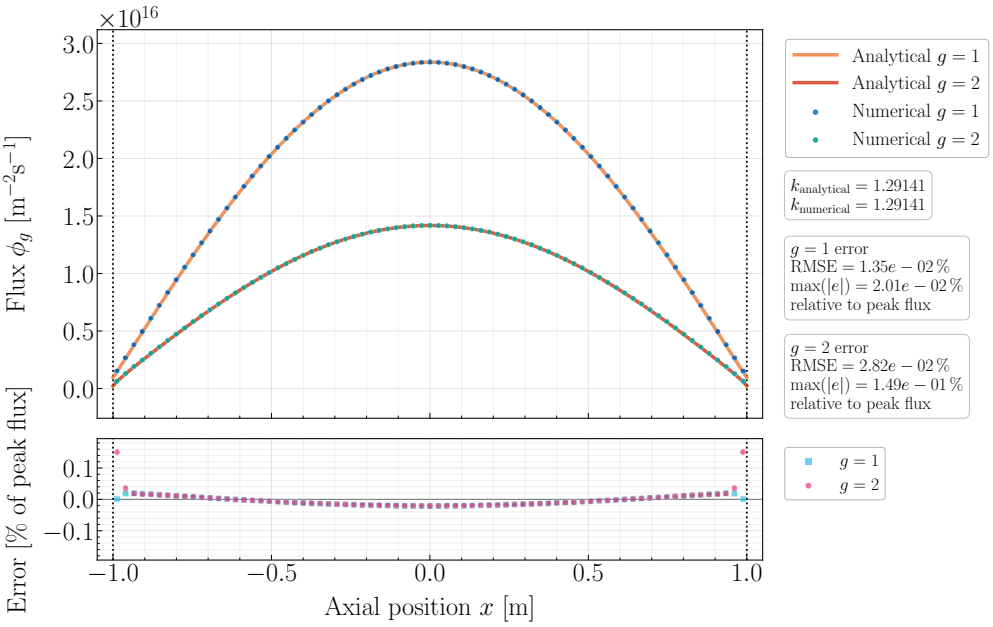

Figure 4.11: Comparison of the numerical and analytical solutions of the one-dimensional neutron balance equation. The presented error is the difference between the cell-averaged analytical value and the numerical cell-centre value, divided by the maximum group scalar flux.

Table 4.4: Input constants used for the two-group diffusion equation validation case.

Quantity	**Value**	**Unit**
Slab length, L	2.0	m
Slab half-width, $a = L/2$	1.0	m
Diffusion coefficient, D_1	1.2×10^{-2}	m
Diffusion coefficient, D_2	3.5×10^{-3}	m
Absorption cross section, $\Sigma_{a,1}$	1.0	m^{-1}
Absorption cross section, $\Sigma_{a,2}$	8.0	m^{-1}
Scattering cross section, $\Sigma_{s0,1\to2}$	4.0	m^{-1}
Scattering cross section, $\Sigma_{s0,2\to1}$	0.0	m^{-1}
Fission cross section, $\Sigma_{f,1}$	2.0×10^{-1}	m^{-1}
Fission cross section, $\Sigma_{f,2}$	5.0	m^{-1}
Average neutrons per fission, ν_1	2.5	–
Average neutrons per fission, ν_2	2.4	–
Nu-fission cross section, $\nu\Sigma_{f,1}$	5.0×10^{-1}	m^{-1}
Nu-fission cross section, $\nu\Sigma_{f,2}$	1.2×10^{1}	m^{-1}
Fission spectrum, χ_1	1.0	–
Fission spectrum, χ_2	0.0	–
Energy released per fission, κ_1	2.0×10^{8}	eV
Energy released per fission, κ_2	2.0×10^{8}	eV
Power per unit area, P_A	1.0×10^{3}	W m^{-2}

5

Coupled Fuel-Assembly Methodology

This chapter describes how the implemented models are combined into a coupled fuel-assembly model capable of evaluating both fuel-assembly operating states and the corresponding heat-transfer limitations. The methodology begins with preparing the necessary input parameters later used by the coupled model. This consists of collecting material data, generating neutronic parameters, and pre-computing effective moderator thermal resistances. The coupled fuel-assembly model is then presented, along with the chosen state variables, the complete system of equations, the computational mesh, the coupling between the different assembly components, and the solution procedure used for the coupled non-linear system. The chapter concludes with a description of how the heat-pipe operating limits are evaluated within the coupled fuel-assembly framework.

5.1 Preparations

Setting up the coupled fuel-assembly model requires several preliminary steps. Fuel-assembly materials are selected and the corresponding temperature-dependent material properties are collected. The high-resolution neutron library is then adapted to the multi-group diffusion equation through a homogenisation process that preserves key system characteristics, such as reaction rates. Finally, the effective thermal resistance of the moderator is pre-computed in order to reduce the computational burden when solving the coupled system of equations.

5.1.1 Material selection

The fuel-assembly materials are selected to match the model implementations and to represent a physically realisable microreactor, inspired by the eVinci microreactor concept. Although the eVinci reactor uses TRISO fuel, UO_2 is chosen because it is simpler to model. UO_2 is the most widely used chemical compound for nuclear fuel. Additionally, its high melting point of 2800 °C, compatibility with zirconium cladding, and good irradiation stability, among other things, make it a suitable candidate [34].

In combination with the fuel, the cladding is then chosen to be zirconium. Its small capture cross section for thermal neutrons is advantageous for neutron trans-

port across the cladding. It is typically preferred to use a zirconium alloy to improve mechanical strength and corrosion resistance, but pure zirconium is used as a simplification in this case [35]. The thermophysical properties used for UO_2 and zirconium correspond to unirradiated material [36, 37].

The heat-pipe materials are chosen to match the eVinci microreactor as closely as possible, based on the publicly available information. Westinghouse reports that the moderating material is graphite and that the heat pipes are manufactured from a FeCrAl alloy, with sodium as the working fluid. The thermophysical data used to model the sodium are given by [20]. The specific chemical composition of FeCrAl by weight was not available for this thesis, but based on the statements made by Westinghouse, it is deemed likely that a Kanthal-like composition is considered [6].

Regarding the graphite moderator, it is typically highly anisotropic, which is difficult to model. Instead, an isotropic variant of graphite (G-348) is selected to serve as a replacement [38, 39]. A summary of the materials used for the fuel assembly in this thesis can be found in Table 5.1.

Table 5.1: Materials used to model the fuel assembly.

Component	**Material**	**Comments**
Fuel	UO_2	100% unirradiated
Fuel-pin cladding	Zirconium	100% unirradiated
Moderator	Graphite	Isotropic graphite variant (G-348)
Heat pipe	FeCrAl alloy	Unirradiated, (Fe 74%, Cr 21%, Al 5%)
Heat-pipe fluid	Sodium	

5.1.2 Neutronic data generation

The neutronic data, including the ENDF/B-VII.1 nuclear library used in this thesis [40], are provided with a significantly higher energy resolution than what can be represented by the 8-group diffusion equation. In addition, the neutron transport mesh used in this work is intentionally coarse, since the objective is to extract the general neutron behaviour, rather than local effects. The high-resolution data therefore need to be adapted to the coarser mesh, energy resolution, and simplified geometry while preserving the general characteristics of the neutron transport in the fuel assembly, such as reaction rates and multiplication factor.

This adaptation is performed through homogenisation using stochastic Monte-Carlo methods. Neutronic Monte-Carlo methods simulate a large number of neutron trajectories while accounting for the coupled effects of geometry, temperature, material composition, and neutron energy [16, Ch. 3.7]. The quantities of interest, such as the multi-group cross-sections, are then generated by weighting the continuous energy nuclear data with the simulated neutron flux spectrum. In this way, representative group constants can be obtained for a simplified geometry while preserving the reaction rates of the original system.

The homogenisation was carried out using the Monte Carlo code *OpenMC* [41]. The energy group boundary selection is based on the CASMO-5 standard 8-group selection for thermal systems, with the upper bounds presented in Table 5.2 [42].

The implementation of the fuel assembly in OpenMC uses periodic boundary conditions in the radial plane of the fuel assembly, and no-reentry conditions on the axial ends. Figure 5.1 illustrates the geometry and material regions, while the material details can be found in the Appendix. A total of 250 batches with 50 000 neutrons per batch were used per simulation. To account for the temperature dependence of the group coefficients, 64 separate OpenMC simulations were performed with different temperature settings. The temperature-dependent group coefficients were then obtained by interpolation between these simulations.

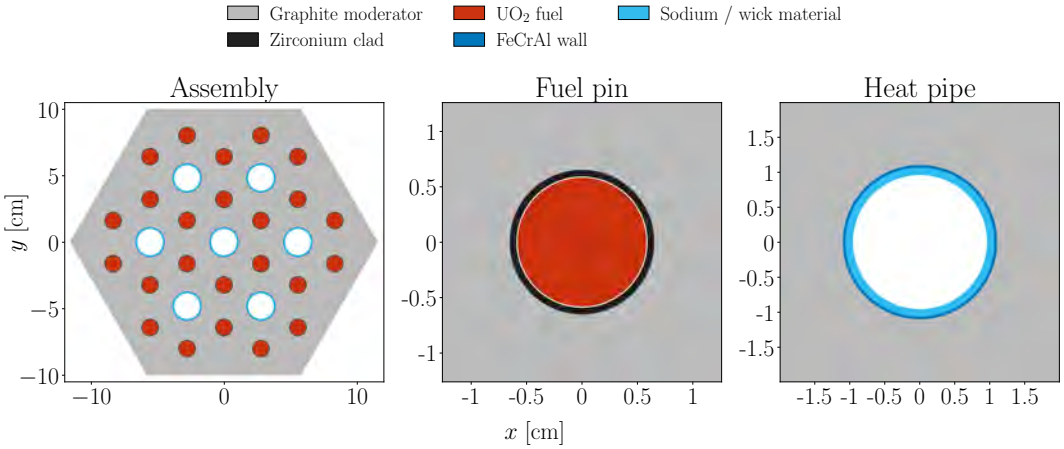

Figure 5.1: Fuel assembly, fuel pin, and heat pipe as they are represented in OpenMC, with colour-coded materials.

Table 5.2: 8-group energy boundaries for thermal systems, as implemented in CASMO-5.

Group	Lower bound [eV]	Upper bound [eV]
1	8.21×10^{5}	2.00×10^{7}
2	5.53×10^{3}	8.21×10^{5}
3	4.00×10^{0}	5.53×10^{3}
4	6.25×10^{-1}	4.00×10^{0}
5	2.80×10^{-1}	6.25×10^{-1}
6	1.40×10^{-1}	2.80×10^{-1}
7	5.80×10^{-2}	1.40×10^{-1}
8	0	5.80×10^{-2}

5.1.3 Moderator effective resistance

Solving the moderator heat-transport equation monolithically with the other governing equations of the fuel assembly would dramatically increase the number of degrees of freedom in the non-linear system of equations. Since the moderator mesh contains approximately 10 000 cells at each axial level, including the whole mesh would result in roughly 1 000 000 additional degrees of freedom. In contrast, the number of degrees of freedom in the coupled fuel-assembly system is on the order of a few thousand. A fully monolithic evaluation would therefore be dominated by the moderator temperature variables, and also lead to a substantial increase in computational effort.

To bypass this, two simplifications are made. First, the moderator heat-transport problem is solved only for a single axial layer, representing radial heat transfer between a fuel pin and a heat pipe. Second, this problem is solved pre-emptively for a range of representative heat-pipe boundary temperatures. The resulting solutions are then used to construct an interpolated effective thermal resistance for radial heat transfer through the moderator. In the coupled fuel-assembly model, this resistance is applied independently at each axial layer to couple the local fuel-pin and heat-pipe temperatures, which is illustrated in the middle section of Figure 5.3.

The effective thermal resistance is evaluated from the solution by computing the mean temperature difference between the fuel-pin boundary temperature, $\bar{T}_{\mathrm{FP}}$, and the heat-pipe boundary temperature, $\bar{T}_{\mathrm{HP}}$, and dividing this difference by the total power generated in the fuel pins, Q_{FP}, according to

$$R_{\mathrm{mod}}(\bar{T}) = \frac{\bar{T}_{\mathrm{FP}} - \bar{T}_{\mathrm{HP}}}{Q_{\mathrm{FP}}} \tag{5.1}$$

where $\bar{T}$ denotes the mean volumetric temperature of the moderator. The temperature dependence arises because the thermal conductivity of graphite varies with temperature.

5.2 Coupled fuel-assembly model

The coupled fuel-assembly model is presented in terms of its governing variables, physical couplings, and numerical solution procedure. The section begins by defining the state variables, the full system of equations, and the fuel-assembly mesh. It then describes how the submodels are coupled through fission heat generation, temperature-dependent neutron data, and the effective thermal resistance between the fuel pins and heat pipes. The final part of the section focuses on the practical solution procedure, with particular emphasis on the construction of the initial guess used to solve the coupled non-linear model.

5.2.1 State variables and model equations

Once the pre-computations have been completed, the geometry specified, and the material and nuclear data processed, the coupled fuel-assembly model is defined by the state variables solved for by the nonlinear solver. The state variables are summarised in Table 5.3. The equations are solved over the full mesh, which is the combination of all the different component meshes, and is presented in Figure 5.2.

Table 5.3: State variables in the coupled fuel-assembly model.

Model part	**State variable**
Neutronics	ϕ_g, k_{eff}
Fuel pins	T
Heat pipe wall-wick region	T
Heat pipe vapour region	T, v

Collecting all the fuel assembly components, the set of equations that governs the state variables and needs to be satisfied simultaneously is as follows:

$$\begin{aligned}
\text{Neutronics:}\quad 0 &= (a^{+}_{g,i} + a^{-}_{g,i})\phi_{g,i} + b_{g,i}\phi_{g,i+1} + c_{g,i}\phi_{g,i-1} + \Sigma_{t,g,i}\phi_{g,i} \qquad (5.2)\\
&\quad - \sum_{g'=1}^{N_G} \Sigma_{s0,g'\to g,i}\phi_{g',i} - \frac{\chi_{g,i}}{k_{\text{eff}}} \sum_{g'=1}^{N_G} \left(\nu\Sigma_f\right)_{g',i}\phi_{g',i}\\
\text{Fuel Pin:}\quad 0 &= \sum_{f\in\mathcal{F}(C)} \frac{S_f k_f}{d_{CF}} \left(T_{F_f} - T_C\right) + q'''V_C \qquad (5.3)\\
\text{Wall-Wick:}\quad 0 &= \sum_{f\in\mathcal{F}(C)} \frac{S_f k_f}{d_{CF}} \left(T_{F_f} - T_C\right) \qquad (5.4)\\
\text{Vapour:}\quad 0 &= \rho(T_i)v_{i+\frac{1}{2}} - \rho(T_{i-1})v_{i-\frac{1}{2}} - \Delta z_i\Gamma_i \qquad (5.5)\\
0 &= \rho(T_i)v^2_{i-\frac{1}{2}} - \rho(T_{i-1})v^2_{i-\frac{3}{2}} + p(T_i) - p(T_{i-1})\\
&\quad + \Delta z_{i-\frac{1}{2}} \frac{f_{D,i-\frac{1}{2}}}{2D_{\text{H}}} \rho(T_{i-1})v_{i-\frac{1}{2}}|v_{i-\frac{1}{2}}| \qquad (5.6)
\end{aligned}$$

5.2.2 Coupling strategy

The state variables of each fuel-assembly subsystem are, in general, dependent on each other, and solving the fuel assembly is therefore a problem of finding the states such that all the governing equations are satisfied simultaneously. The way in which the dependence is addressed is the subject of a coupling strategy. The main couplings are as follows. First, the fuel pins and heat pipes are thermally coupled through the moderator, which is represented by an effective thermal resistance. Second, the neutron flux and the temperature-dependent fission quantities determine the volumetric heat source distribution in the fuel pins. Third, the fuel-pin and heat-pipe temperatures affect the neutron data used in the diffusion calculation, and therefore also the neutron-flux distribution.

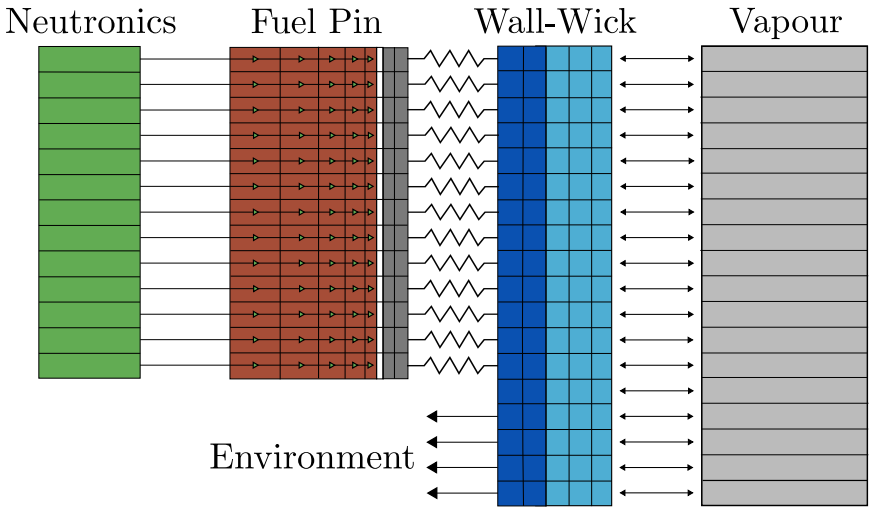

Figure 5.2: Full mesh used to discretise the coupled fuel-assembly model. The two-dimensional fuel-pin and heat-pipe meshes are shown as axial-radial cross-sections, while the neutronics and vapour regions are discretised axially.

Thermal coupling between fuel pins and heat pipes. By modelling the moderator using the aforementioned effective resistances, the heat transfer is greatly simplified. To go from the last cell centre in the fuel pins to the first cell centre in the heat pipes, heat is conducted through the remaining half-cell of the fuel pins, through the moderator effective resistances, and finally through the first half of the first cell in the heat pipes; this process is illustrated in Figure 5.3.

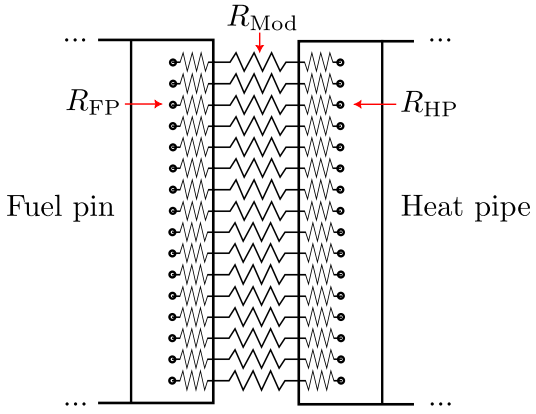

Figure 5.3: Illustration of the thermal resistances during heat transfer between one fuel pin's outer cell centres and a heat pipe's outer cell centres. The outer cell centres are marked with small circles. The moderator is modelled by thermal resistances bridging the fuel pins to the heat pipes.

Assuming perfect contact between the moderator and the fuel pins and the heat pipes, and assuming that there is no axial heat transfer in the moderator, the total resistance in one axial slice is a series connection of the three resistances

$$R_{\text{tot}}(T) = R_{\text{FP}}(T) + R_{\text{mod}}(T) + R_{\text{HP}}(T). \tag{5.7}$$

The fuel-pin and heat-pipe resistances are given by conduction through a cylindrical volume

$$R(T) = \frac{\ln \frac{r_{\text{outer}}}{r_{\text{inner}}}}{2\pi k(T)\Delta z}. \tag{5.8}$$

These assumptions are important limitations of the coupling model. In reality, there is a small gap between the fuel pins and the moderator, which increases the equilibrium temperature of the fuel pins. Furthermore, the assumption of no axial heat transfer is generally not an accurate description, but is applied to simplify the heat transfer mechanism.

Additionally, because the fuel assembly is represented by an effective one-fuel-pin–one-heat-pipe model, the heat removed from the fuel pins must be scaled to preserve the total heat transferred in the representative moderator slice. The moderator slice contains two fuel pins and 7/12 heat pipes. Therefore, if $Q_{i,\text{FP}}$ denotes the heat leaving one fuel pin at axial position i, the corresponding heat transferred to one effective heat pipe at the same axial position is

$$Q_{i,\text{HP}} = \frac{2}{7/12} Q_{i,\text{FP}} = \frac{24}{7} Q_{i,\text{FP}}. \tag{5.9}$$

Fission heat source. The generation of heat in the fuel pins is directly determined by the neutron flux and the fission quantities, since the neutron flux describes the spatial distribution of fission reactions. Using the energy per fission $\kappa(E,T)$ and the macroscopic fission cross-section $\Sigma_f(E,T)$, the volumetric heat density generated from fission can be determined from the neutron flux

$$q'''(\boldsymbol{r}) = \int_0^\infty \kappa(\boldsymbol{r},E,T)\Sigma_f(\boldsymbol{r},E,T)\phi(\boldsymbol{r},E)\,dE. \tag{5.10}$$

In the present case, the one-dimensional discrete equation reads for fuel pin cells on the axial level i

$$q'''_i = \sum_{g=1}^{N_G} \kappa_{g,i}(\bar{T}_{\text{FP,i}}, \bar{T}_{\text{Mod,i}}, \bar{T}_{\text{HP,i}})\Sigma_{f,g,i}(\bar{T}_{\text{FP,i}}, \bar{T}_{\text{Mod,i}}, \bar{T}_{\text{HP,i}})\phi_{g,i}. \tag{5.11}$$

Since the moderator is not solved explicitly in the coupled model, its local average temperature is approximated from the neighbouring fuel-pin and heat-pipe temperatures as

$$\bar{T}_{\text{Mod}} \approx \frac{\bar{T}_{\text{FP}} + \bar{T}_{\text{HP}}}{2} \tag{5.12}$$

Temperature feedback in the diffusion equation. The same temperature approximation is used when evaluating the neutron data in the discrete diffusion equation (2.35). At each axial position i, the diffusion coefficient, total cross-section, scattering matrix, fission spectrum, and fission production cross-section are interpolated using the temperature state

$$\left(\bar{T}_{\text{FP},i}, \bar{T}_{\text{Mod},i}, \bar{T}_{\text{HP},i}\right) \approx \left(\bar{T}_{\text{FP},i}, \frac{\bar{T}_{\text{FP},i} + \bar{T}_{\text{HP},i}}{2}, \bar{T}_{\text{HP},i}\right). \tag{5.13}$$

Thus,

$$D_{g,i}, \quad \Sigma_{t,g,i}, \quad \Sigma_{s0,g'\to g,i}, \quad \chi_{g,i}, \quad \left(\nu\Sigma_f\right)_{g,i} \tag{5.14}$$

are evaluated from the local axial temperature state at position i. The neutron-flux solution is therefore coupled back to the thermal solution through the temperature dependence of the neutron data.

5.2.3 Numerical solution procedure

The residuals are combined and solved monolithically using fsolve from the Python package SciPy [43], which is based on MINPACK's modified Powell hybrid method. Since the numerical solver starts from an initial state and iteratively converges towards a state that satisfies the coupled system of equations, an important step in finding a solution to the fuel-assembly model is setting up an initial guess for the state variables. The initial guess dictates how fast the solver converges, what state it converges to, and whether it converges at all in certain cases.

For simple systems, a rough initial guess is usually sufficient, but when the system becomes more complicated, a more accurate guess can be necessary. The approach used here is therefore to solve the fuel-assembly model through a sequence of increasingly complex fuel-assembly models. Instead of attempting to construct an accurate initial guess for the fully coupled model directly, the solution from a simpler model is used as the initial guess for the next, more complex model. In this way, each solve acts as a continuation step towards the full temperature-dependent and fluid-coupled solution.

The first model in this hierarchy, denoted C, is simple enough for a crude initial guess to be adequate. In this model, the fluid model is omitted and replaced by an isothermal vapour approximation, while the temperature dependence of the thermal conductivities and neutron parameters is ignored. The initial guess for the simple model is as follows: The axial neutron flux is initialised using a cosine distribution with appropriate scaling. The same axial shape is then used to initialise the heat input to the heat-pipe evaporator, again with appropriate scaling. The fuel-pin temperatures are initialised as a uniform distribution.

The solution of model C is then used as the initial guess for a second model named B, in which the heat-pipe fluid effects are included, while the temperature dependencies in the thermal conductivities and neutron parameters are still ignored. Finally, the solution of model B is used as the initial guess for the fully coupled fuel-assembly model. If convergence cannot be obtained at any stage, an additional continuation step is introduced by first solving the corresponding model on a coarser mesh before using that solution to initialise the finer-mesh problem.

Table 5.4: Model hierarchy used in the numerical solution procedure. The models are presented in order of greatest complexity first.

Model	Vapour model	Data treatment
A	1D discretised	Temperature-dependent thermal and neutronic data
B	1D discretised	Fixed thermal and neutronic data
C	Isothermal	Fixed thermal and neutronic data

5.3 Evaluation of heat-pipe operating limits

First, we consider the limits that are not resolved within the numerical model: The boiling and the entrainment limits. These are computed analytically using the respective expressions presented in Section 2.5. The solutions are based on the material properties specified in Section 5.1.1 together with the reactor input parameters.

The capillary and sonic limits are determined numerically through an iterative approach involving repeated evaluations of the fully coupled fuel-assembly model with progressively adjusted fuel pin power levels P_{FP} and condenser-side environmental heat transfer coefficient h_{env}. The parameter adjustment is continued until the criterion of the corresponding limit is fulfilled. The axial heat-transfer limit, Q_{HP}, is then recorded as a function of the operating temperature T_{op}, to construct the characteristic Q–T graph.

More specifically, for the sonic limit each data point is obtained by fixing the condenser-side environmental heat-transfer coefficient and subsequently adjusting the fuel-pin power until the maximum vapour velocity in the interior of the heat pipe reaches a Mach number of unity.

Furthermore, for the capillary limit, each data-point is obtained by first choosing an approximate operating temperature for the heat pipe, and then setting an initial fuel-pin power output. The fuel-pin power is then increased iteratively until the capillary limit is reached. Since the operating temperature of the heat pipe cannot be set as a simulation parameter, the environmental heat-transfer coefficient is instead estimated before each simulation, based on the following approximate relationship.

$$h_{\mathrm{env}} = \frac{Q_{\mathrm{HP}}}{S_{\mathrm{env}}(T_{\mathrm{op}} - T_{\mathrm{env}})} \tag{5.15}$$

6

Results

In this chapter, the main results of the coupled fuel-assembly model are presented. In the first part, the heat-pipe operating limits of a fuel assembly in an eVinci-like reactor are evaluated and combined into a Q–T operating map. The numerically obtained limits are also compared to the analytical models. In the second part, the operating map is used to select two representative reactor states with the purpose of comparing the model behaviour. In this way, different model assumptions are also tested for the predicted heat-pipe temperatures, fuel-pin temperatures, and neutronic spectra.

6.1 Heat-pipe limitations

This section uses the fully coupled fuel-assembly model to construct a Q–T diagram for the heat-pipe limitations. Subsequently, the numerical results are compared to the analytical expressions presented in Section 2.5. The calculations are based on the reactor data listed in Table A.2 in Appendix A. The resulting Q–T diagram is presented in Figure 6.1, which compares the four heat-pipe limitations as a function of the operating temperature in the heat pipe[1].

The results show that no single limitation controls the full temperature range. At the lower end of the temperature range, the sonic limitation is most restrictive. The monotonic increase is expected, since the velocity increases when the density of the saturated vapour decreases in order to maintain the same level of heat transfer.

Following the sonic limitation is the capillary limitation, which occurs in the intermediate temperature range. The capillary limit is not as steep as the sonic limitation and eventually levels off. This behaviour shows that increasing temperatures and imposed heat loads improve vapour transport, but that the resulting pressure losses in the heat pipe remain a finite constraint. The capillary limit is therefore a relevant restriction in the reactor.

The analytical entrainment limit increases monotonically with temperature and remains above the sonic and capillary limits. It therefore appears not to be a dominant restriction on the heat-pipe operation for this particular configuration. In contrast, the boiling limit appears in the higher temperature range and provides an upper

[1]In this thesis, the operating temperature is defined as the average temperature in the heat pipe.

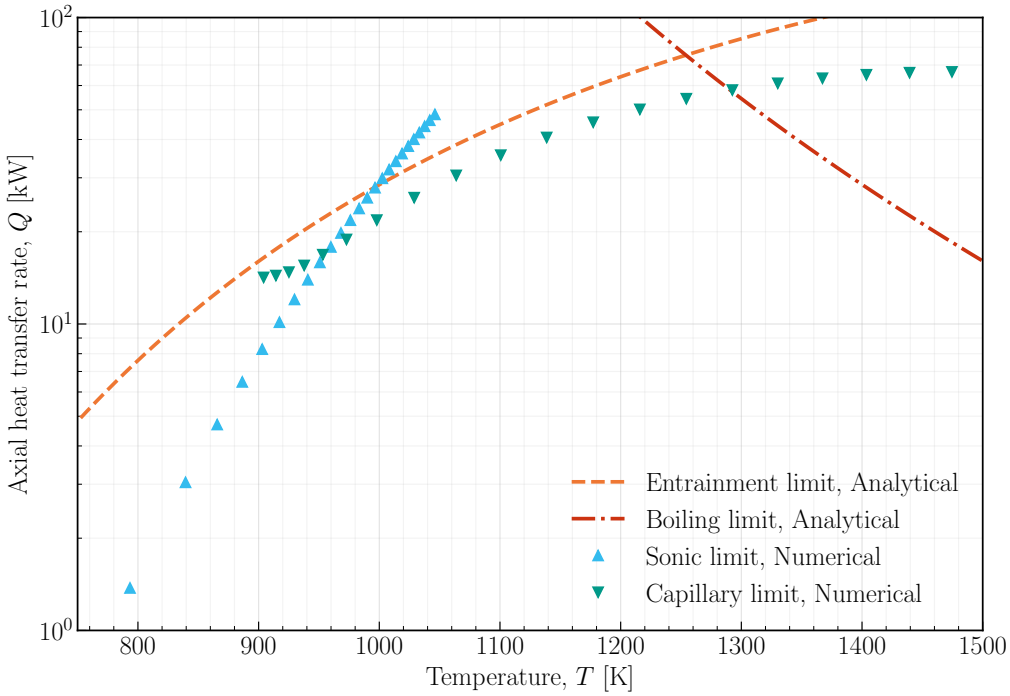

Figure 6.1: The resulting entrainment, boiling, sonic and capillary limits for the fuel assembly inspired by the eVinci concept. The entrainment and boiling limits are evaluated based on analytical expressions. The sonic and capillary limits are evaluated based on the fully coupled fuel assembly model.

bound on the temperature for different heat loads. This limitation is highly sensitive to changes in input parameters and should therefore not be considered reliable.

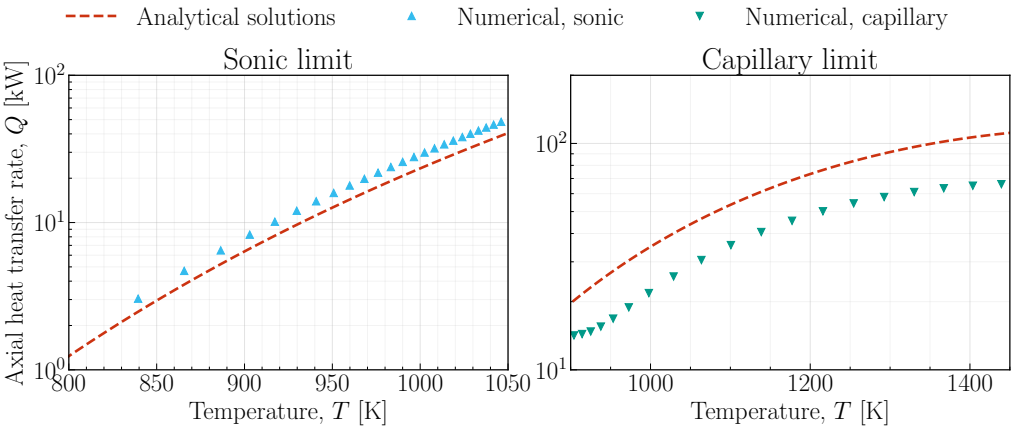

Figure 6.2: Comparison of numerical sonic and capillary limits with corresponding analytical solutions for a representative eVinci reactor fuel assembly. The sonic limit was obtained for 25 heat-transfer coefficients, linearly spaced between 75.0 and 1800.0 $\mathrm{W\,m^{-2}\,K^{-1}}$. The capillary limit was obtained for 20 approximate operating temperatures, linearly spaced between 850 and 1400 K. The two analytical limits, boiling and entrainment, were evaluated over the temperature interval 750–1400 K using the material data presented in Section 5.1.1.

The numerical results for the sonic and capillary limits are compared with the corresponding analytical expressions in Figure 6.2. It can be observed that both of the limits show qualitative agreement between the analytical and numerical results, as indicated by the approximate constant offset in the logarithmic plot. On average, the numerical sonic limit is 24.3% higher than the analytical prediction, whereas the numerical capillary limit is 36.1% lower.

6.2 Comparison of fuel-assembly states in different heat-pipe operating regimes

To connect the heat-pipe limitation analysis to the subsystem-level results of the coupled model, two operating points are selected from the operating map shown in Figure 6.3. The operating map is obtained from the limiting curves presented in Figure 6.1. The first point represents the predicted Q–T state from the fully coupled model given the marketed eVinci-reactor power output of 15 MW(th) [6], corresponding to a heat-pipe power input of approximately 17 kW(th). The second point represents a fuel-assembly state where the heat pipe is operating on the sonic limit predicted earlier.

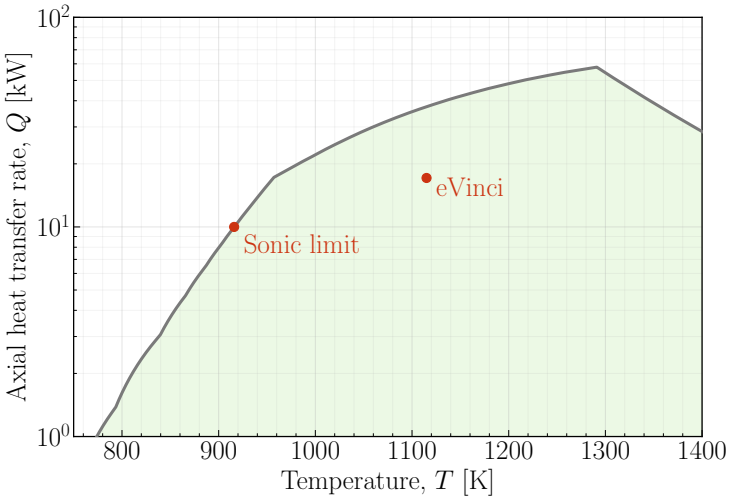

Figure 6.3: Heat-pipe operating region extracted from the limiting curves presented in Figure 6.1. The two markers show the reactor operating conditions for two different simulations. The first simulation mimics the eVinci operating conditions and operates within the allowable operating region, whereas the second simulation lies on the sonic limit.

The remainder of this chapter is dedicated to presenting the detailed results of the fuel assembly in these selected operating states. In addition to examining the predictions of the fully coupled model, two simplifications are introduced and used for comparison. The three models are labelled A, B, and C, in decreasing complexity, as described in Section 5.2.3. For the model predictions at the sonic limit, only Models A and C will be shown, to avoid repeating the findings from the first case. Table 6.1 summarises the data for the two selected operating points.

Table 6.1: Operating points used for the two reactor simulations.

Case	T_{op} [K]	Q_{HP} [kW]	h_{env} [W m^{-2} K^{-1}]	Models
eVinci	958	16.6	692	A, B, C
Sonic limit	1008	9.1	320	A, C

6.2.1 eVinci-like operating conditions

Heat pipe

Figure 6.4 shows a comparison of the axial heat-pipe temperatures for the three models in eVinci-like operating conditions. Models A and B are nearly indistinguishable, showing that the material temperature dependence has little influence on the temperature profile in this heat-pipe operating regime. This is expected, since the temperature variation in the heat pipe is small.

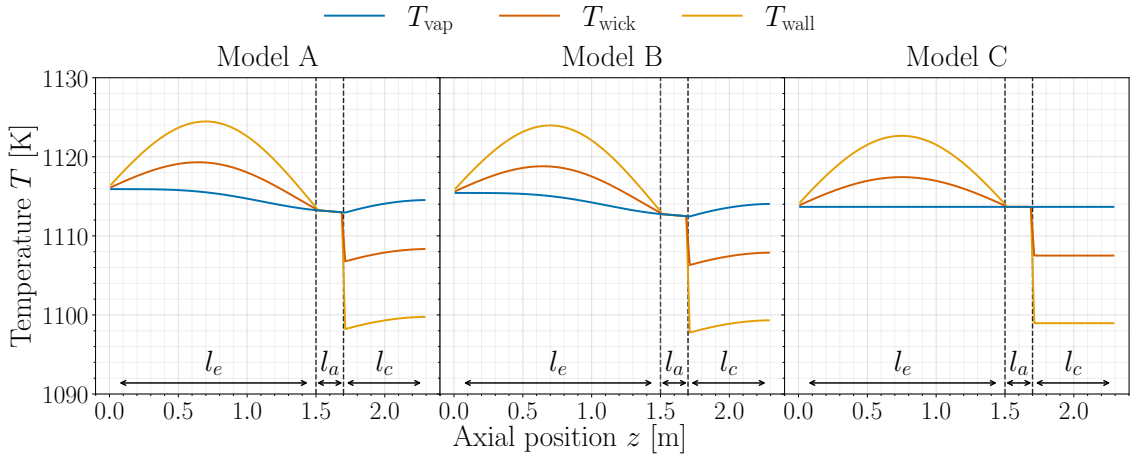

Figure 6.4: Axial temperature profiles in the vapour, wick, and wall for the three different models under normal heat pipe operation.

A slight difference is observed between the models with discretised vapour, Models A and B, and the model with an isothermal vapour approximation, Model C. However, this difference is not important in most cases. Approximating the vapour as isothermal is, therefore, acceptable in this operating regime.

Inspecting the radial temperature variation, the progression is consistent with expectations. The vapour temperature is the lowest temperature radially in the evaporator section, meaning that heat enters the vapour, while the vapour temperature is the highest radial temperature in the condenser section, meaning that heat exits the vapour. This is congruent with the idea of the working fluid evaporating in the evaporator, and the vapour condensing in the condenser. Additionally, the temperatures in the adiabatic section show that the radial sections equilibrate, which is expected, since there is no heat applied to the outer wall of the adiabatic section of the heat pipe. Finally, the sharp transition to the condenser section is due to the piecewise heat flux at the boundary.

Fuel pin

As seen in Figure 6.5, the fuel-pin temperatures for the eVinci-like operating condition show the expected axial shape, with maximum temperatures near the centre of the fuel and lower temperatures toward the ends. This largely reflects the axial neutron-flux distribution.

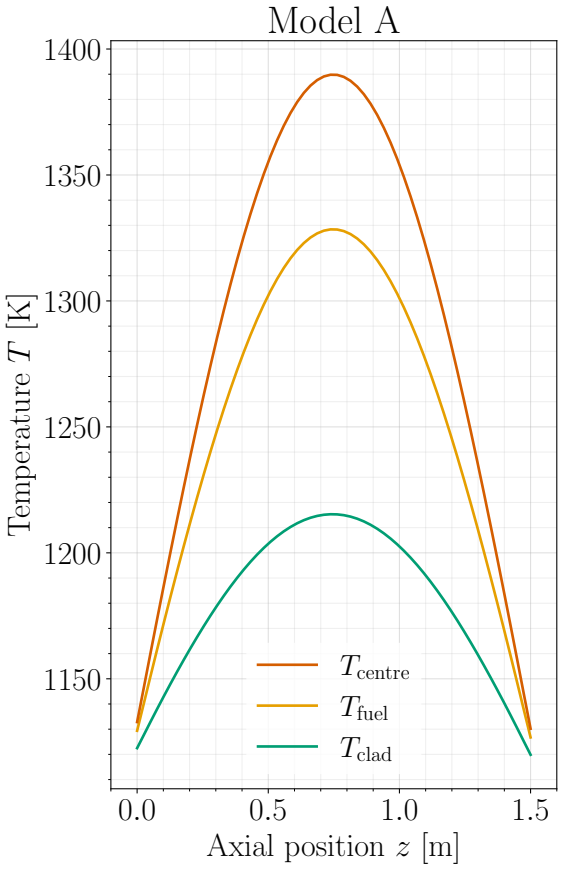

Quantity	Value [K]
System A	
$\bar{T}_{\text{centre}}$	1295.42
$\bar{T}_{\text{fuel}}$	1255.82
$\bar{T}_{\text{clad}}$	1181.62
$\max_z(T_{\text{fuel}} - T_{\text{clad}})$	113.08
$\max_z(T_{\text{centre}} - T_{\text{clad}})$	174.47
System B	
$\bar{T}_{\text{centre}}$	1301.04
$\bar{T}_{\text{fuel}}$	1258.75
$\bar{T}_{\text{clad}}$	1180.83
$\max_z(T_{\text{fuel}} - T_{\text{clad}})$	117.14
$\max_z(T_{\text{centre}} - T_{\text{clad}})$	180.72
System C	
$\bar{T}_{\text{centre}}$	1300.14
$\bar{T}_{\text{fuel}}$	1257.84
$\bar{T}_{\text{clad}}$	1179.92
$\max_z(T_{\text{fuel}} - T_{\text{clad}})$	117.14
$\max_z(T_{\text{centre}} - T_{\text{clad}})$	180.72

Figure 6.5: Axial fuel-pin temperature profiles for Model A using the eVinci-like power output, together with summary temperature quantities for Models A–C. The plotted profiles show the centreline temperature, fuel-average temperature, and cladding temperature along the fuel pin. In the table on the right, the barred temperatures represent the axially averaged temperatures in each corresponding region.

The radial temperature ordering is also physically consistent. The highest temperature is found in the centre, followed by the fuel-average and finally the cladding. This indicates that heat is transported out of the fuel pin. The resulting temperature drop is significantly larger than the temperature drop in the heat pipe, showing that the fuel-pin conduction resistance is an important contribution for the coupled model.

In contrast to the heat pipe, the slight difference is now between the models with and without temperature-dependent material properties. Including temperature dependence reduces the overall temperature level in the fuel pin. In general, however,

there is no significant difference between the model predictions.

Neutronics

The average neutron-flux spectra for the eVinci-like fuel assembly are shown in Figure 6.6. The three models produce almost identical spectral shapes, with the largest fluxes in the low-energy groups and progressively lower fluxes toward the fast-energy range. The stepwise appearance is a consequence of the discrete energy groups. The similarities indicate that the overall neutron-energy distribution is not strongly affected by the model differences. Importantly, the material temperature dependence only weakly changes the spectrum. This is consistent with the relatively weak temperature dependence observed in the homogenised cross-section data.

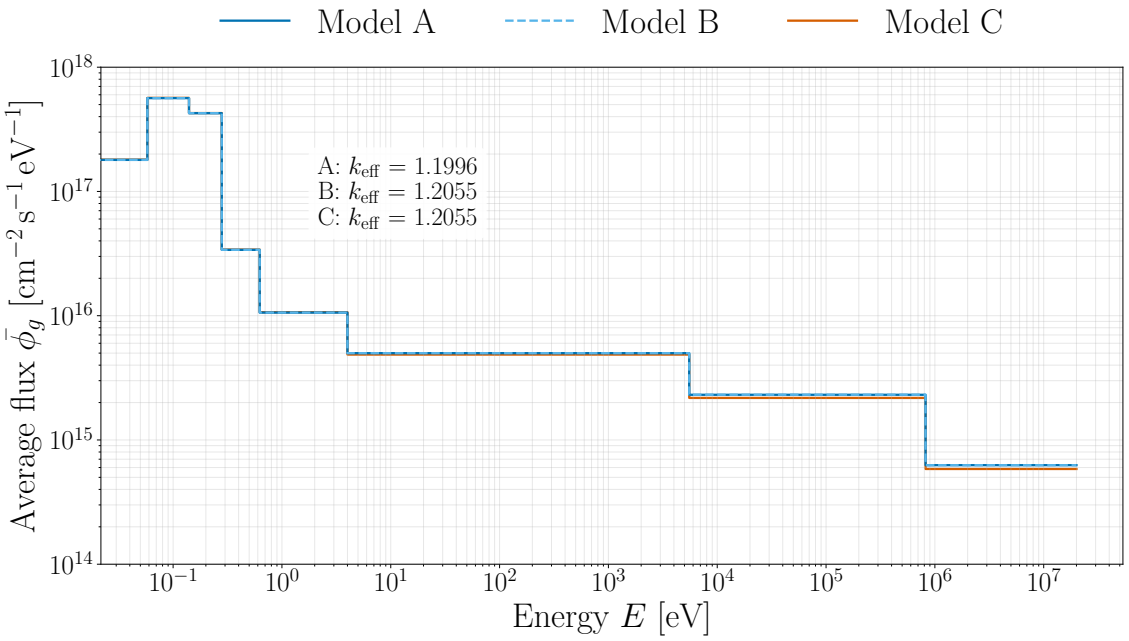

Figure 6.6: Average scalar neutron flux as a function of neutron energy for Models A–C in the eVinci-like fuel assembly. The flux is shown using the eight-group energy discretisation, which gives the spectra their step-like appearance. The three systems produce nearly identical energy distributions, with only small differences in magnitude and in the corresponding eigenvalues k_{eff}.

The effective multiplication factors are also close, although Model A gives a slightly lower value than Models B and C. Together with the previous result, this further indicates that the material temperature dependence only has a slight effect on the neutronic solution, most likely through the homogenised cross sections.

6.2.2 Sonic-limit operating conditions

In the normal reactor state simulation, the aim of presenting the results from Model B was mainly to separate the effect of temperature-dependent material and neutronic data from the effect of the vapour-model approximation. However, it did not show

substantially different behaviour from Models A and C. The thermal profiles of Model B were close to those of Model A, while the neutron flux spectrum was close to that of Model C. This subsection therefore focuses on the direct comparison between Model A and Model C, with the purpose of examining the effect of the isothermal-vapour approximation when the heat pipe operates close to the sonic limit.

Heat pipe

The resulting axial heat-pipe temperatures for the sonic limit operating state are shown in Figure 6.7. In contrast to the normal state simulation, the difference between Models A and C is now substantial. The isothermal-vapour approximation in Model C produces a temperature profile that remains relatively similar to the eVinci-like operating state, with a maximum heat-pipe wall temperature difference of approximately 24 K. Model A, however, predicts a much larger axial temperature variation, with a total wall temperature difference of approximately 155 K. The temperature decreases through the evaporator and adiabatic sections, and continues to decrease into the condenser before recovering sharply further downstream. This behaviour is not captured by the isothermal-vapour approximation, showing that the simplified vapour treatment becomes inadequate near the sonic limit.

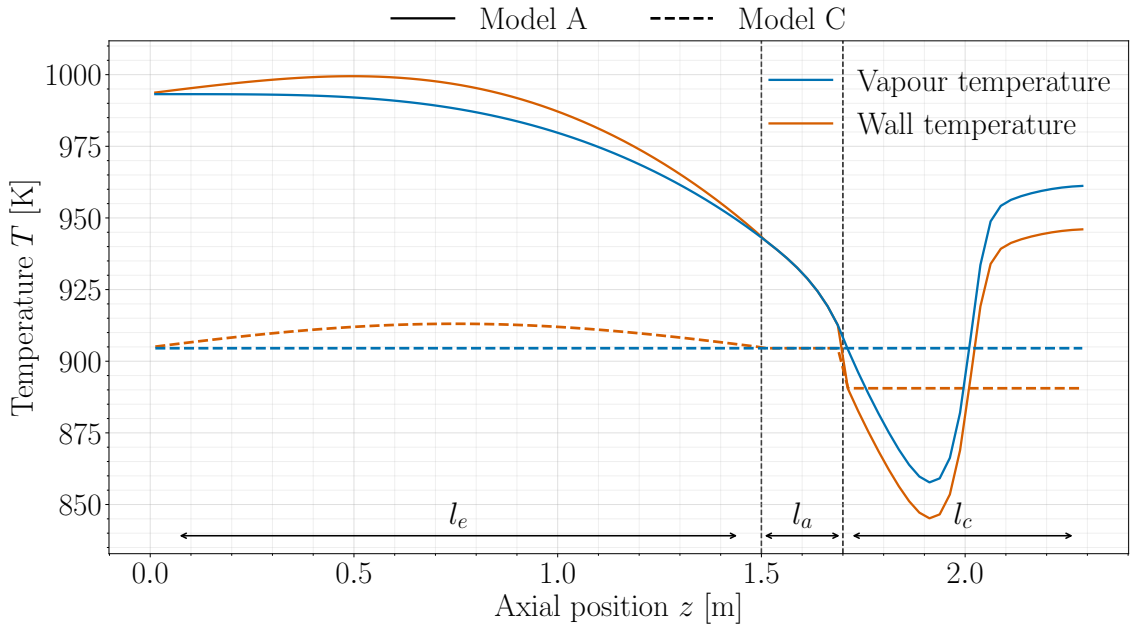

Figure 6.7: The heat-pipe operating states for Models A and C in the simulation at the sonic limit. The solid lines represent the fully coupled model, or Model A, while the dashed graphs represent the isothermal-vapour model, Model C.

Fuel pin

The axial fuel-pin temperature profiles for Models A and C are shown in Figure 6.8. In both models, the temperature increases toward the centre of the fuel pin, as

expected from the axial power distribution. However, Model A predicts significantly higher temperatures than Model C because the full vapour model gives a higher and more strongly varying heat-pipe temperature field. The profile in Model A is also more asymmetric, with the maximum shifted toward the evaporator side of the fuel pin. This differs from the previous simulation presented, where the fuel-pin temperatures were much less sensitive to the vapour-model approximation.

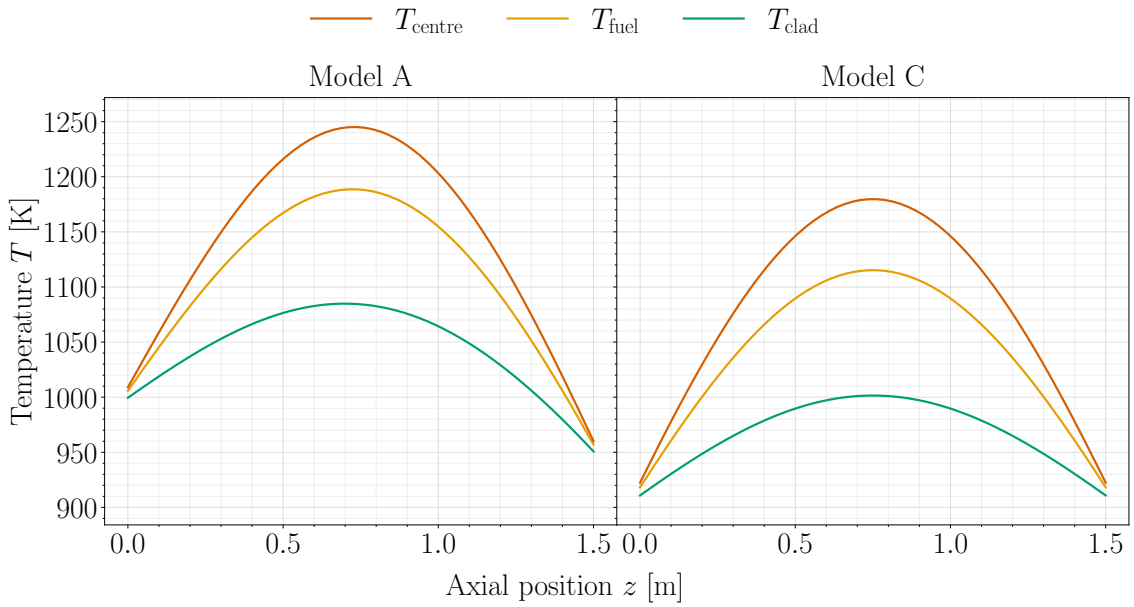

Figure 6.8: The fuel pin operating state for the simulation at the sonic limit for Models A and C.

Neutronics

The neutron-flux spectra for the sonic-limit simulation are shown in Figure 6.9. As in the normal state simulation, the two models produce similar spectral shapes, despite the much larger difference in the thermal state. This indicates that the energy distribution of the neutron flux is relatively insensitive to the vapour-model approximation. The effect on the multiplication factor is also limited, with a difference between the models of $\Delta k_{\text{eff},2} = -490\,\text{pcm}$, compared to $\Delta k_{\text{eff},2} = -590\,\text{pcm}$ in the normal state simulation.

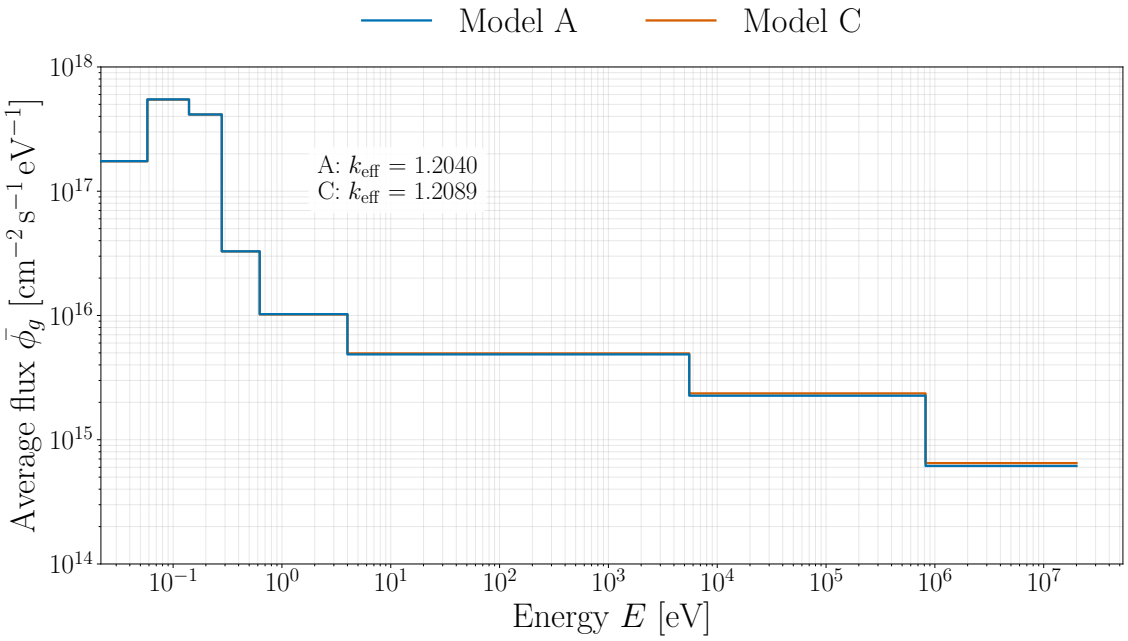

Figure 6.9: The average scalar neutron flux as a function of energy in the sonic limit simulation. The two curves resemble step functions because the neutron conservation equation is treated with a multi-group formalism.

7

Conclusion & Outlook

The aim of this thesis was to develop a reduced coupled model capable of simulating the main interactions in a representative fuel assembly of a heat-pipe-cooled microreactor. The final model couples the neutron-flux distribution, the fuel-pin and heat-pipe temperature distributions, and the vapour flow in the heat-pipe vapour channel. Although the model contains several geometrical and physical simplifications, it is able to describe the main feedbacks between heat generation, heat transfer, and heat-pipe operation.

The model was used to evaluate relevant heat-pipe operating limits. The resulting operating map shows that the limiting mechanism depends on the heat-pipe operating temperature in a mostly expected way. At lower temperatures, the sonic limit is the most restrictive, while the capillary limit becomes relevant at intermediate temperatures. The boiling limit is the limiting factor at higher temperatures, while the entrainment limit does not seem to have an impact on the operating region for this particular fuel-assembly configuration. Although the rough estimate of the boiling limitation is not especially reliable, the limitation is typically not a problem for liquid-metal heat pipes [4].

Furthermore, a comparison of the numerically obtained limits from the fully coupled model with simplified analytical limits shows qualitative agreement, but a quantitative discrepancy by an approximately constant factor. This can in part be explained by the differences in the physical mechanism considered and the discrepancy between the vapour-model predictions and the experimental results. But the accuracy of the numerically obtained limits is not fully known and comparisons with experimental data or high-fidelity models are thus desired.

The first research question concerned the operating conditions and heat-pipe limitations predicted for a representative fuel assembly of an eVinci-like microreactor. The results suggest that the operating conditions for the eVinci-like microreactor occur inside the predicted heat-pipe operating region. Importantly, however, the stability of the operating point has not been assessed. Assuming that the heat-pipe limitations are approximately accurate, a next step could therefore be to investigate the effect of perturbations at the eVinci operating point.

The second research question concerned how the predicted reactor state changes when different levels of model complexity are introduced. Under steady-state operating conditions far from any heat-pipe operating limit, the comparisons show only

small differences between the investigated models. In this regime, the simpler models reproduce the main fuel-pin and neutronic quantities reasonably well, provided that temperature-dependent material and neutronic parameters are evaluated at a representative temperature.

However, the isothermal vapour approximation becomes less reliable near the sonic limit. There, the vapour pressure drop becomes large enough that the associated saturation temperature varies greatly along the axis. The isothermal-vapour model inherently does not take this into account, which results in a different fuel-pin temperature distribution. The axially discretised vapour model is therefore mainly relevant when vapour pressure and saturation-temperature variations become significant, such as near the sonic limit.

Future work could extend the reduced coupled model by introducing a two-dimensional vapour-flow description and a two-dimensional neutronic model over a homogenised fuel assembly. A two-dimensional vapour model would make it possible to resolve the radial velocity profile in the heat-pipe vapour channel, instead of treating the vapour flow as cross-sectionally averaged. This could improve the accuracy of the predicted sonic limit and make the comparisons to experimental results more explicit. A two-dimensional homogenised neutronic model would retain more of the geometrical effects of the fuel-pin, moderator, and heat-pipe arrangement. This could allow spatial variations in the neutron flux to couple more directly to the temperature field, and thereby improve the description of temperature-dependent neutronic feedback.

Additionally, further work could include modelling the entire reactor, as opposed to a single representative fuel assembly. This would be useful because heat transfer across the boundaries of the fuel assemblies would likely imply a higher temperature in the centre of the reactor and a lower temperature further away. This would mean that there would not be a single operating point, but an operating region (within the operating region bounded by the limitations).

Bibliography

[1] M. N. Ivanovskii, V. P. Sorokin, and I. V. Yagodkin. *The Physical Principles of Heat Pipes*. Oxford University Press, New York, 1982.

[2] G. Hu. Development of heat pipe modeling capabilities in a fully-implicit solution framework. In C. Liu, editor, *Proceedings of the 23rd Pacific Basin Nuclear Conference, Volume 1*, pages 845–860, Singapore, 2023. Springer Nature Singapore.

[3] B. H. Yan, C. Wang, and L. G. Li. The technology of micro heat pipe cooled reactor: A review. *Annals of Nuclear Energy*, 135:106948, 2020.

[4] A. Faghri. *Heat Pipe Science and Technology*. Taylor & Francis, 1995.

[5] M. A. Gibson, D. I. Poston, P. McClure, T. Godfroy, J. Sanzi, and M. H. Briggs. The kilopower reactor using stirling technology (KRUSTY) nuclear ground test results and lessons learned. In *2018 International Energy Conversion Engineering Conference*, 2018.

[6] M. M. Swartz, W. A. Byers, J. Lojek, and R. Blunt. Westinghouse eVinci™ heat pipe micro reactor technology development. In *Proceedings of the 28th International Conference on Nuclear Engineering*, volume 1, page V001T04A018, 2021.

[7] Antares Nuclear, Inc. Antares Achieves Criticality of Mark-0 Reactor, June 2026. Accessed: 2026-06-29.

[8] U.S. Department of Energy, Office of Nuclear Energy. NUCLEAR 101: How does a nuclear reactor work? `https://www.energy.gov/ne/articles/nuclear-101-how-does-nuclear-reactor-work`, May 2025. Published May 19, 2025.

[9] International Atomic Energy Agency (IAEA). Industrial applications and nuclear cogeneration. `https://www.iaea.org/topics/non-electric-applications/industrial-applications-and-nuclear-cogeneration`. Non-electric applications.

[10] J. Liou. What are small modular reactors (SMRs)? `https://www.iaea.org/newscenter/news/what-are-small-modular-reactors-smrs`, September 2023. Published Sep. 13, 2023.

[11] D. I. Poston, R. J. Kapernick, and R. M. Guffee. Design and analysis of the SAFE-400 space fission reactor. In *AIP Conference Proceedings*, volume 608, pages 578–588, 2002.

[12] Logan Harbour et al. 4.0 MOOSE: Enabling massively parallel multiphysics simulation. *SoftwareX*, 31:102264, 2025.

[13] Joshua E. Hansel, Ray A. Berry, David Andrs, Matthias S. Kunick, and Richard C. Martineau. Sockeye: A one-dimensional, two-phase, compressible flow heat pipe application. *Nuclear Technology*, 207(7):1096–1117, 2021.

[14] Yaqi Wang et al. Griffin: A moose-based reactor physics application for multiphysics simulation of advanced nuclear reactors. *Annals of Nuclear Energy*, 211:110917, 2025.

[15] Christopher Matthews, Vincent Laboure, Mark DeHart, Joshua Hansel, David Andrs, Yaqi Wang, Javier Ortensi, and Richard C. Martineau. Coupled multiphysics simulations of heat pipe microreactors using direwolf. *Nuclear Technology*, 207(7):1142–1162, 2021.

[16] C. Demazière. *Modelling of Nuclear Reactor Multi-physics: From Local Balance Equations to Macroscopic Models in Neutronics and Thermal-Hydraulics*. Academic Press/Elsevier, 2020.

[17] J. R. Lamarsh. *Introduction to Nuclear Reactor Theory*. Addison-Wesley Publishing Company, 1966.

[18] F. P. Incropera, D. P. DeWitt, T. L. Bergman, and A. S. Lavine. *Fundamentals of Heat and Mass Transfer*. John Wiley & Sons, 6 edition, 2007.

[19] F. Moukalled, L. Mangani, and M. Darwish. *The Finite Volume Method in Computational Fluid Dynamics: An Advanced Introduction with OpenFOAM and Matlab*. Springer, 2015.

[20] J. K. Fink and L. Leibowitz. Thermodynamic and transport properties of sodium liquid and vapor. Technical report, Argonne National Laboratory, IL, United States, January 1995.

[21] E. J. Hinch. Fluid dynamics ii, 2020. Available at: `https://www.damtp.cam.ac.uk/user/hinch/teaching/FluidsIInotes.pdf`.

[22] G. Bar-Meir. *Basics of Fluid Mechanics*. University Press of Florida, 2009.

[23] G. W. Howell and T. M. Weathers. Aerospace fluid component designers' handbook. volume i, revision d. Technical Report AFRPL-TDR-64-25, TRW Systems Group, Redondo Beach, CA, 1970. Vol. I-D, Defense Technical Information Center, AD0874542.

[24] H. Jouhara, D. Reay, R. McGlen, P. Kew, and J. McDonough. *Heat Pipes: Theory, Design and Applications*. Elsevier, 7 edition, 2024.

[25] R. Bertossi, C. Romestant, V. Ayel, and Y. Bertin. Theoretical study and review on the operational limitations due to vapour flow in heat pipes. *Frontiers in Heat Pipes*, 3:023001, 2012.

[26] T. Cotter. Theory of heat pipes. Technical Report LA-3246-MS, Los Alamos National Laboratory, 1965.

[27] B. S. Garbow, K. E. Hillstrom, and J. J. Moré. Documentation for MINPACK subroutine HYBRD. Technical report, Argonne National Laboratory, March 1980. Accessed: May 2026.

[28] K. Madsen, H. B. Nielsen, and O. Tingleff. Methods for non-linear least squares problems. Technical report, Informatics and Mathematical Modelling, Technical University of Denmark, April 2004.

[29] C. Mueller and P. Tsvetkov. A review of heat-pipe modeling and simulation approaches in nuclear systems design and analysis. *Annals of Nuclear Energy*, 160:108393, 2021.

[30] Nils T. Basse. Turbulence intensity and the friction factor for smooth- and rough-wall pipe flow. *Fluids*, 2(2):30, 2017.

[31] Y. Cao and A. Faghri. Transient two-dimensional compressible analysis for high-temperature heat pipes with pulsed heat input. *Numerical Heat Transfer, Part A: Applications*, 18(4):483–502, 1991.

[32] Christophe Geuzaine and Jean-François Remacle. Gmsh: A three-dimensional finite element mesh generator with built-in pre- and post-processing facilities. *International Journal for Numerical Methods in Engineering*, 79(11):1309–1331, 2009.

[33] C. Demazière. Physics of steady-state neutron transport. Course material for TRA410 Nuclear Reactor Technology – Past, Present and Future, 2024.

[34] M. T. Simnad. Nuclear reactor materials and fuels. In R. A. Meyers, editor, *Encyclopedia of Physical Science and Technology*, pages 775–815. Academic Press, New York, 3 edition, 2003.

[35] D. Mayweg, J. Eriksson, M. Sattari, H.-O. Andrén, and M. Thuvander. Corrosion of zirconium fuel cladding inside a boiling water reactor: A post-irradiation study by atom probe tomography. *Acta Materialia*, 292:121020, 2025.

[36] A. Bouloré, C. Struzik, V. Bouineau, F. Gaudier, G. Damblin, and S. Bernaud. Modelling of UO_2 thermal conductivity: Improvement of the irradiation defects contribution and uncertainty quantification. *Nuclear Engineering and Design*, 407:112304, 2023.

[37] J. K. Fink and L. Leibowitz. Thermal conductivity of zirconium. *Journal of Nuclear Materials*, 226(1):44–50, 1995.

[38] B. Marsden, A. Jones, G. Hall, M. Treifi, and P. Mummery. Graphite as a core material for Generation IV nuclear reactors. In P. Yvon, editor, *Structural Materials for Generation IV Nuclear Reactors*, pages 495–532. Woodhead Publishing, 2016.

[39] D. McEligot, W. D. Swank, D. L. Cottle, and F. I. Valentin. Thermal properties of G-348 graphite. Technical report, Idaho National Laboratory, Idaho Falls, ID, United States, 2016.

[40] M. B. Chadwick et al. ENDF/B-VII.1 nuclear data for science and technology: Cross sections, covariances, fission product yields and decay data. *Nuclear Data Sheets*, 112(12):2887–2996, 2011.

[41] P. K. Romano, N. E. Horelik, B. R. Herman, A. G. Nelson, B. Forget, and K. Smith. OpenMC: A state-of-the-art monte carlo code for research and development. *Annals of Nuclear Energy*, 82:90–97, 2015.

[42] Serpent Wiki. CASMO 8-group structure. `https://serpent.vtt.fi/mediawiki/index.php/CASMO_8-group_structure`. Accessed: May 22, 2026.

[43] Pauli Virtanen et al. SciPy 1.0: Fundamental algorithms for scientific computing in python. *Nature Methods*, 17:261–272, 2020.

A

Fuel assembly data

Table A.1: Spatial mesh sizing used for the full fuel-assembly model.

Subsystem	**Parameter**	**Symbol**	**Value**
Mesh sizing			
	Heat pipe wall–wick radial cells	$N_{r,\mathrm{HP,ww}}$	15
	Heat pipe wall–wick axial cells	$N_{z,\mathrm{HP,ww}}$	60
	Heat pipe vapour axial cells	$N_{z,\mathrm{vap}}$	60
	Fuel pin radial cells	$N_{r,\mathrm{FP}}$	15
	Fuel pin axial cells	$N_{z,\mathrm{FP}}$	46
	Neutronic axial cells	$N_{z,\mathrm{n}}$	46

Table A.2: Input parameters used for the full fuel-assembly model.

Subsystem	Parameter	Symbol	Value
Heat pipe			
	Vapour radius	r_{vap}	$9.54 \times 10^{-3}\,\mathrm{m}$
	Wick thickness	δ_{wick}	$3.89 \times 10^{-4}\,\mathrm{m}$
	Gap thickness	δ_{gap}	$6.81 \times 10^{-4}\,\mathrm{m}$
	Wall thickness	δ_{wall}	$3.89 \times 10^{-4}\,\mathrm{m}$
	Evaporator length	L_{evap}	$1.50\,\mathrm{m}$
	Adiabatic length	L_{ad}	$0.20\,\mathrm{m}$
	Condenser length	L_{cond}	$0.60\,\mathrm{m}$
	Condenser temperature	T_{cond}	$300\,\mathrm{K}$
	Vapour heat-transfer coefficient	h_{vap}	$1.0 \times 10^{6}\,\mathrm{W\,m^{-2}\,K^{-1}}$
	Effective pore radius	r_{pore}	$2.0 \times 10^{-5}\,\mathrm{m}$
	Wick porosity	φ	0.70
	Sodium density	$\rho_{\mathrm{Na}}(T)$	Given by [20]
	FeCrAl density	ρ_{FeCrAl}	$7.16\,\mathrm{g\,cm^{-3}}$
Fuel pin			
	Fuel radius	r_{fuel}	$6.50 \times 10^{-3}\,\mathrm{m}$
	Gap thickness	δ_{gap}	$1.0 \times 10^{-4}\,\mathrm{m}$
	Cladding thickness	δ_{clad}	$6.0 \times 10^{-4}\,\mathrm{m}$
	Fuel-pin length	L_{FP}	$1.50\,\mathrm{m}$
	Enrichment	–	$19.75\,\%$
	UO_2 density	$\rho_{\mathrm{UO_2}}$	$10.6\,\mathrm{g\,cm^{-3}}$
	Zirconium density	ρ_{Zr}	$6.6\,\mathrm{g\,cm^{-3}}$
Reactor			
	Core diameter	D_{core}	$2.80\,\mathrm{m}$
	Flake diameter	D_{flake}	$0.20\,\mathrm{m}$
	Pin-cell pitch	–	$3.20 \times 10^{-2}\,\mathrm{m}$
	Number of heat pipes	N_{HP}	876
	Number of fuel pins	N_{FP}	2970
	Graphite density	ρ_{graphite}	$1.85\,\mathrm{g\,cm^{-3}}$

B

Files and Inputs

The core components of the software are contained in the directories listed below, all of which should be located within the same root directory. Additional information about the code can be found in the corresponding `ReadMe.md` file in each folder. The source code is available upon request by contacting either of the authors.

- `nuclear_data/` – Directory containing the nuclear data used by the neutronics calculations. In particular, the `endfb71/endfb-vii.1-hdf5/` subdirectory contains the HDF5-formatted ENDF/B-VII.1 data, including neutron, photon, and windowed multipole data.
- `coupled_systems/` – Contains implementations of the coupled systems used to combine the individual physics models.
- `data/` – Contains input data and preprocessed data used by the model.
- `models/` – Contains the main model implementations. This directory is divided into subdirectories for the different components of the coupled model:
  - `fuel_assembly/` – Homogenisation of the neutron coefficients in the fuel assembly utilising OpenMC.
  - `fuel_pin/` – Fuel-pin heat-transfer model components.
  - `heatpipe/` – Heat-pipe and vapour-flow model components.
  - `moderator/` – Moderator model components.
  - `neutronics/` – Neutronics model components.
- `scripts/` – Contains scripts and notebooks used to generate results, figures, and supporting calculations. The scripts are grouped by application:
  - `fuelpin/` – Scripts related to the fuel-pin model.
  - `heatpipe/` – Scripts related to the heat-pipe model.
  - `heatpipe_limits/` – Scripts for evaluating heat-pipe operating limits.
  - `iso_reactor/` – Scripts related to the isothermal-reactor approximation.
  - `moderator/` – Scripts related to the moderator model.
  - `neutronics/` – Scripts related to the neutronics model.

  - `reactors/` – Scripts for coupled reactor simulations.
  - `theory_illustrations/` – Scripts used to generate theoretical illustrations.
  - `vapour_reactor/` – Scripts related to vapour-flow reactor simulations.
- `tests/` – Contains test cases for selected model components:
  - `heat_discretised_model/` – Tests for the discretised heat-transfer model.
  - `vapour_discretised_model/` – Tests for the discretised vapour-flow model.
- `utils/` – Contains utility functions used across the code base, such as solver code, material data, interpolator code, etc.

C

Benchmark of Vapour Model

C.1 Estimate of the maximum vapour Mach number

An independent estimate of the maximum vapour Mach number was computed from the experimental heat input, vapour-core geometry, and measured vapour-temperature profiles. The estimate is based on the assumption that the largest vapour velocity occurs near the end of the evaporator section. At this location, the vapour mass flow rate is approximated by assuming that the applied heat input has been converted into latent heat of evaporation, such that

$$\dot{m}_v(T) \approx \frac{Q_{\text{in}}}{h_{fg}(T)}, \tag{C.1}$$

where Q_{in} is the applied heat load and $h_{fg}(T)$ is the temperature-dependent latent heat of vaporisation. The vapour velocity is then estimated from the one-dimensional mass-flow relation

$$u_v(T) \approx \frac{\dot{m}_v(T)}{\rho_v(T) A_v} = \frac{Q}{h_{fg}(T)\rho_v(T)A_v}, \tag{C.2}$$

where $\rho_v(T)$ is the vapour density and

$$A_v = \pi r_v^2 \tag{C.3}$$

is the vapour-core cross-sectional area.

The local speed of sound in the vapour was estimated as

$$c_s(T) = \sqrt{\frac{\gamma p_v(T)}{\rho_v(T)}}, \tag{C.4}$$

where $p_v(T)$ is the saturation pressure and γ is the ratio of specific heats. In the calculations, $\gamma = 5/3$ was used. The corresponding temperature-dependent Mach-number estimate is therefore

$$M(T) = \frac{u_v(T)}{c_s(T)} = \frac{Q}{h_{fg}(T)\rho_v(T)A_v}\sqrt{\frac{\rho_v(T)}{\gamma p_v(T)}}. \tag{C.5}$$

For each experiment, this expression was evaluated at the measured vapour temperatures. The maximum estimated Mach number for a given experiment was then defined as

$$M_{\max}^{(i)} = \max_j M\left(T_j^{(i)}\right), \tag{C.6}$$

where $T_j^{(i)}$ denotes the measured vapour temperature at axial measurement point j in experiment i. Finally, the largest estimated Mach number over all experiments was computed as

$$M_{\max} = \max_i M_{\max}^{(i)}. \tag{C.7}$$

This estimate should be interpreted as an approximate upper-bound estimate based on the experimental temperature data and the assumption that the peak mass flow rate occurs near the end of the evaporator. It neglects detailed axial variations in mass flow rate, pressure losses, and any velocity-profile effects within the vapour core.

C.2 Comparison model

The derivation of the comparison model is similar to the main model, the only difference being the saturation closure. Instead of using empirical correlations, the ideal gas law and the Clausius–Clapeyron relation are used

$$p = \rho R T \tag{C.8}$$

$$\frac{dP}{dT} = \frac{P h_{fg}}{T^2 R}, \tag{C.9}$$

where R is the specific gas constant. Using Equation (C.9), we can write

$$\frac{dp}{dz} = \frac{p h_{fg}}{T^2 R}\frac{dT}{dz}. \tag{C.10}$$

The pressure can now be substituted using Equation (C.8)

$$\frac{dp}{dz} = \frac{\rho(T) h_{fg}}{T}\frac{dT}{dz}. \tag{C.11}$$

We want to find an expression for the density $\rho(T)$. Approximating h_{fg} as a constant and integrating Equation (C.9) between T and T_c, we get

$$P = P_c \exp\left[\frac{h_{fg}}{R}\left(\frac{1}{T_c} - \frac{1}{T}\right)\right], \tag{C.12}$$

where P_c is the characteristic pressure at the characteristic temperature T_c and P is the pressure at T. Substituting for P using Equation (C.8), we get

$$\rho(T) = \frac{P_c}{RT} \exp\left[\frac{h_{fg}}{R}\left(\frac{1}{T_c} - \frac{1}{T}\right)\right]. \tag{C.13}$$

The values for P_c, T_c, h_{fg}, and μ can be found in Table C.1.

Case	P_c [Pa]	T_c [K]	h_{fg} [J kg^{-1}]	μ [Pa s]
1	2476	856	4.182×10^6	1.80×10^{-5}
2	1300	818	4.182×10^6	1.80×10^{-5}
3	2476	856	4.182×10^6	1.80×10^{-5}
4	2476	856	4.182×10^6	1.80×10^{-5}

Table C.1: Additional parameters for Model 2. The parameters in cases 1 and 2 are based on G. Hu [2]. Cases 3 and 4 use the same parameters as case 2.

DEPARTMENT OF PHYSICS
CHALMERS UNIVERSITY OF TECHNOLOGY
Gothenburg, Sweden
www.chalmers.se

CHALMERS
UNIVERSITY OF TECHNOLOGY